UNIVERSITY OF CALIFORNIA SAN DIEGO

Revealing Composition-Performance Relationships In Halide Perovskite Solar Cells By Correlative Microscopy

A dissertation submitted in partial satisfaction of the
requirements for the degree of Doctor of Philosophy

in

Nanoengineering

by

Yanqi Luo

Committee in charge:

Professor David P. Fenning, Chair
Professor Shadi A. Dayeh
Professor Darren J. Lipomi
Professor Ying Shirley. Meng
Professor Oleg Shpyrko

2020

The Dissertation of Yanqi Luo is approved, and it is acceptable in quality and form for publication on microfilm and electronically:

Chair

University of California San Diego

2020

TABLE OF CONTENTS

LIST OF FIGURES

LIST OF TABLES

ACKNOWLEDGEMENTS

First of all, I would like to thank my advisor, Professor David Fenning, for granting me this great opportunity for my PhD journey, his unwavering support, his patient and continual audience, and his immense knowledge. David is a great mentor and is always open to new ideas. His guidance and vision helped me all the time in my research and made this dissertation possible. Besides my advisor, I would like to thank the rest of my thesis committee: Prof. Shadi Dayeh, Prof. Darren Lipomi, Prof. Ying Shirley Meng, and Prof. Oleg Shpyrko, for their insightful comments that helped strengthen my thesis.

Secondly, I would like show my special appreciation to all of my colleagues in the Solar Energy Innovation Laboratory (SOLEIL), especially Rishi Kumar, Taewoo Kim, Deniz Cakan, and Moses Kodur. With their help, my graduate life at UCSD became much more enjoyable. Doing scientific work without collaboration and interaction with others is impossible, so I feel fortunate to have been part of such a great team. A special thanks to Juan Pablo Correa-Baena, Thomas M. Brenner, Michael Stuckelberger, Parisa Khoram, and Lioz Etgar. I would also like to thank Barry Lai for supporting my work at 2ID-D .

Finally, I would like to thank my parents and dear friends for their constant support, and Ruo Xuan, for her understanding through this challenging and difficult time during my PhD. Special thanks to Wisely Yang for help proofread this thesis.

Chapter 1, in part, is a reprint of the material “The Relationship between Chemical Flexibility and Nanoscale Charge Collection in Hybrid Halide Perovskites” as it appears in Advanced Functional Materials, Yanqi Luo, Sigalit Aharon, Michael Stuckelberger, Ernesto Magaña, Barry Lai, Mariana I. Bertoni, Lioz Etgar, and David P. Fenning, 2018, 28 (18), 1706995. The dissertation author was the primary investigator and author of this material.

Chapter 2, in part, is a reprint of the material ”X-Ray Microscopy of Halide Perovskites: Techniques, Applications, and Prospects” as it appears in Advanced Energy Materials, Moses Kodur, Rishi E. Kumar, Yanqi Luo, Deniz N. Cakan, Xueying Li, Michael Stuckelberger, and David P. Fenning, 2020, 1903170, and an ongoing work of the material ”Quantitative

Specifications to Avoid Degradation during E-beam and Induced Current Microscopy of Halide Perovskite Devices" for submission with authors of Yanqi Luo, Pritesh Parikh, Thomas M. Brenner, Juan-Pablo Correa-Baena, Tonio Buonassisi, Ying Shirley Meng, and David P. Fenning. The dissertation author contributed to the XRF, XBIC and EBIC portion of this material.

Chapter 3, in full, is a reprint of the material "Spatially Heterogeneous Chlorine Incorporation in Organic-Inorganic Perovskite Solar Cells" as it appears in Chemistry of Materials, Yanqi Luo, Shany Gamliel, Sally Nijem, Sigalit Aharon, Martin Holt, Benjamin Stripe, Volker Rose, Mariana I. Bertoni, Lioz Etgar, and David P. Fenning, 2016, 28, 6536-6543, and a reprint of the material "The Relationship between Chemical Flexibility and Nanoscale Charge Collection in Hybrid Halide Perovskites" as it appears in Advanced Functional Materials, Yanqi Luo, Sigalit Aharon, Michael Stuckelberger, Ernesto Magaña, Barry Lai, Mariana I. Bertoni, Lioz Etgar, and David P. Fenning, 2018, 28 (18), 1706995. The dissertation author was the primary investigator and author of this material.

Chapter 4, in full, is a reprint of the material "Direct Observation of Halide Migration and its Effect on the Photoluminescence of Methylammonium Lead Bromide Perovskite Single Crystals" as it appears in Advanced Materials, Yanqi Luo, Parisa Khoram, Sarah Brittman, Zhuoying Zhu, Barry Lai, Shyue Ping Ong, Erik C. Garnett, and David P. Fenning, 2017, 1703451, 1-7. The dissertation author was one of the primary investigators and author of this material.

Chapter 5, in full, is currently being prepared for submission for publication of the material "Microscopic degradation mechanism in MA-free perovskite solar cells under various stressors intrinsic to operation", Nengxu Li, Yanqi Luo, Zehua Chen, Xiuxiu Niu, Xiao Zhang, Jiuzhou Lu, Rishi Kumar, Junke Jiang, Huifen Liu, Xiao Guo, Barry Lai, Geert Brocks, Qi Chen, Shuxia Tao, David P. Fenning, Huanping Zhou. The dissertation author was one of the primary investigators and author of this material.

Chapter 6, in full, is a reprint of the material "Homogenized halides and alkali cation segregation in alloyed organic-inorganic perovskites", Juan-Pablo Correa-Baena1, Yanqi Luo,

Thomas M. Brenner, Jordan Snaider, Shijing Sun, Xueying Li, Mallory A. Jensen, Noor Titan Putri Hartono, Lea Nienhaus, Sarah Wieghold, Jeremy R. Poindexter, Shen Wang, Ying Shirley Meng, Ti Wang, Barry Lai, Martin V. Holt, Zhonghou Cai, Moungi G. Bawendi, Libai Huang, Tonio Buonassisi, David P. Fenning. The dissertation author was one of the primary investigators and author of this material.

VITA

2009-2013 B. S. in Chemistry, California Polytechnic State University San Luis Obispo

2013-2014 M. S in Polymer Science, California Polytechnic State University San Luis Obispo

2014-2015 R&D Chemist, Nusil Technology, LLC

2015-2020 Ph. D. in NanoEngineering, University of California San Diego

PUBLICATIONS

Y. Luo, P. Parikh, T. M. Brenner, J.-P. Correa-Baena, T. Buonassisi, Y. S. Meng, D. P. Fenning, "Quantitative Specifications to Avoid Degradation during E-beam and Induced Current Microscopy of Halide Perovskite Devices," *in preparation*

M. Kodur, R. E. Kumar, **Y. Luo** D. N. Cakan, X. Li, D. P. Fenning, "X-ray Microscopy of Halide Perovskites: Techniques, Applications, and Prospects," *Advanced Energy Materials*, 1903170, 1, 2020

R. Wang, J. Xue, K-Li. Wang, Z-K. Wang, **Y. Luo**, D. P. Fenning, G. Xu, S. Nuryyeva, T. Huang, Y. Zhao, J. L. Yang, J. Zhu, M. Wang, S. Tan, I. Yavuz, K. N. Houk, Y. Yang, "Constructive Molecular Configurations for Surface-Defect Passivation of Perovskite Photovoltaics," *Science*, 366 (6472), 1509, 2019

X. Li, **Y. Luo**, M. Holt, Z. Cai, D. P. Fenning, "Residual Nanoscale Strain in Cesium Lead Bromide Perovskite Reduces Stability and Shifts Local Luminescence," *Chemistry of Materials*, 31 (8), 2778, 2019

J.-P. Correa-Baena†, **Y. Luo**†, T. M. Brenner, J. Snaider, S. Sun, X. Li, M. A. Jensen, N. Titan, P. Hartono, L. Nienhaus, S. Wieghold, J. R. Poindexter, S. Wang, Y. S. Meng, T. Wang, B. Lai, M. V Holt, Z. Cai, M. G. Bawendi, L. Huang, T. Buonassisi, D. P. Fenning, "Homogenized Halides and Alkali Cation Segregation in Alloyed Organic-Inorganic Perovskites," *Science*, 363 (6427), 627, 2019 (†- co-first author)

Y. Luo, S. Aharon, M. Stuckelberger, E. Magaña, B. Lai, M. I. Bertoni, L. Etgar, D. P. Fenning, "The Relationship between Chemical Flexibility and Nanoscale Charge Collection in Hybrid Halide Perovskites," *Advanced Functional Materials,*, 28 (18), 1706995, 2018

G. W. P. Adhyaksa, S. Brittman, A. Haralds, A. Lof, X. Li, J. D. Keelor, **Y. Luo**, T. Duevski, R. M. A. Heeren, S. R. Ellis, D. P. Fenning, E. C. Garnett, "Understanding Detrimental and Beneficial Grain Boundary Effects in Halide Perovskites," *Advanced Materials*, 30 (52), 1804792, 2018

T. Kim, A. Kargar, **Y. Luo**, R. Mohammed, E. Martinez-Loran, A. Ganapathi, P. Shah, D. P. Fenning,"Enhancing C2–C3 Production from CO_2 on Copper Electrocatalysts via a Potential-Dependent Mesostructure," *ACS Applied Energy Materials*, 1 (5), 1965, 2018

J. Wang, A. S. Jeevarathinam, A. Jhunjhunwala, H. Ren, J. Lemaster, **Y. Luo**, D. P. Fenning, E. E. Fullerton, J. V Jokerst, "A Wearable Colorimetric Dosimeter to Monitor Sunlight Exposure," *Advanced Materials Technologies*, 3 (6), 1800037, 2018

Y. Luo, P. Khoram, S. Brittman, Z. Zhu, B. Lai, S. P. Ong, E. C. Garnett, D. P. Fenning,"Direct Observation of Halide Migration and Its Effect on the Photoluminescence of Methylammonium Lead Bromide Perovskite Single Crystals," *Advanced Materials*, 29 (43), 1703451, 2017

Y. Luo, S. Gamliel, S. Nijem, S. Aharon, M. Holt, B. Stripe, V. Rose, M. I. Bertoni, L. Etgar, D. P. Fenning,"Spatially Heterogeneous Chlorine Incorporation in Organic-Inorganic Perovskite Solar Cells" *Chemistry of Materials*, 28 (18), 6536, 2016

ABSTRACT OF THE DISSERTATION

Revealing Composition-Performance Relationships In Halide Perovskite Solar Cells By Correlative Microscopy

by

Yanqi Luo

Doctor of Philosophy in Nanoengineering

University of California San Diego, 2020

Professor David P. Fenning, Chair

In recent years, hybrid halide perovskite solar cells have attracted much attention due to their excellent optoelectronic performance. Leveraging the structural flexibility of perovskites, composition engineering appears to be an effective approach to improve material and device stability but can also raise durability challenges such as phase separation. In this presentation, I will share insights into the composition-performance relationships in these emerging materials resulting from correlative X-ray, electron, and optical microscopy investigations. Encompassing a wide range of perovskite chemistries, this work reveals the challenges and benefits of increasing compositional complexity and elucidates the roles of substituents and additives in these complex

material systems. By identifying potential pitfalls in tuning the materials chemistry of halide perovskites, we provide a path forward for further improving their optoelectronic performance and making them commercially viable.

Chapter 1

A Brief Introduction to Halide Perovskites and Their Applications in Photovoltaics

One of the biggest challenges we face in the 21^{st} century is reducing our dependence on non-renewable fossil fuels. Providing a path forward to a cleaner and greener tomorrow, solar energy is abundant and accessible. Our overarching goal in solar energy research is to capture this resource efficiently, produce solar electricity cost-effectively, and to build durable systems to power our society.

Solar cells, also known as photovoltaic (PV) devices, capture and convert solar energy directly to electricity using semiconducting materials. Owing to significant research over the past 60 years, today's silicon (Si) solar cells are commercially viable at a large scale. UC San Diego recently expanded its microgrid to a 2.4 megawatt solar network because the university identified this upgrade as a strong return on investment. In fact, California has a solar initiative program (CSI) as an incentive for people to install solar panels on their houses. In 2018, California took a giant step further and became the first state to mandate new homes have solar panels installed.

One drawback of Si-based PVs, however, is that their fabrication requires multiple costly and energy-intensive high-temperature steps, including crystal growth above 1400 °C. In stark contrast, an emerging class of solar cells, called perovskite solar cells (PSCs), is processed in the range of 100-150 °C,[1, 2] which translates to more than a 90% reduction in production energy requirements and a reduced energy- and carbon- payback time. These hybrid halide perovskites

show great potential in PV applications not only due to a 50% reduction in manufacturing costs relative to Si-based PVs, but also due to their excellent optoelectronic properties. The exceptional minority carrier diffusion lengths in these materials[3, 4] lead to nearly 100% internal quantum efficiency[5], which results in high charge carrier collection efficiency and external luminescence efficiency in PV devices.[2, 6]

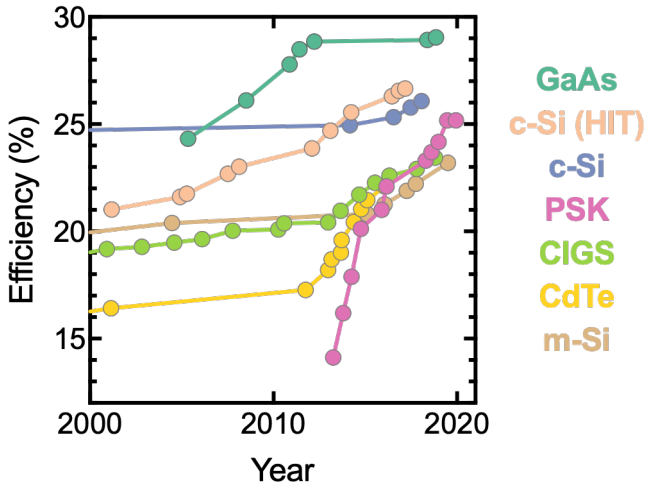

Figure 1.1. Improvement of photovoltaic devices using different types of light absorbing materials in the past decades.[7] The selective light absorbing materials are gallium arsenide (GaAs) thin film crystal, monocrystalline Si with heterojunction thin instrinsic layer (c-Si HIT), monocrystalline Si (c-Si), halide perovskites (PSK), copper indium gallium selenide (CIGS), multicrystalline Si (m-Si), and cadmium telluride (CdTe).

These extraordinary material properties have enabled perovskite solar absorbers to achieve large improvements in device performance in the past decade. State-of-the-art perovskite solar cells have outperformed all other polycrystalline photovoltaic absorbers, including multicrystalline Si as shown in Figure 1.1. After the demonstration of a device with 3.8% power conversion efficiency (PCE) by Miyasaka *et al*, a breakthrough in perovskite photovoltaics occurred in 2012 when the first all-solid-state hybrid perovskite devices were shown by Kim *et al*,[8] improving the chemical stability of the perovskite absorber and enabling device performance to exceed 9%. With intense investigation of perovskite material properties globally from a vast number of research groups, including bandgap engineering and stability optimization

by tuning chemical composition,[9, 10, 11, 12] the record PCE of halide perovskite solar cells reached 25.2% in 2019. Surpassing 25% PCE by leveraging the chemical flexibility of the perovskite structure as well as interface engineering in devices[6], hybrid perovskite solar cells became the most efficient polycrystalline solar absorbers to date. Their efficiency exceeds those of other emerging solar absorbers including copper indium gallium selenide (CIGS) and cadmium telluride (CdTe).

To fully exploit the hybrid perovskites for commercially viable optoelectronic applications, robust functional thin films must be reproduced consistently. The electronic and chemical instability of halide perovskites due to anomalous electronic hysteresis,[13, 14] rapid decomposition under exposure to ultraviolet (UV) or visible light[15], and moisture[16] presents a critical challenge to the reliability of halide perovskites in optoelectronic applications.[17, 18, 19] The chemical flexibility of the perovskite holds promise for addressing these issues through formulating complex compositions. An interesting and counter-intuitive trend is observed in perovskite literature, in which improved efficiency and stability has been strongly correlated with increased chemical complexity within the methylammonium (MA) containing perovskites. However, complex chemical composition often leads to other potential challenges, such as difficult homogenized mixing and proneness to phase segregation. The complex material system of a high-performing perovskite absorber is a metaphorical black box, in which the fundamental roles of each elements and the underlying mechanism of elemental enhancement are poorly understood or altogether unexplored. Herein, this thesis is centered around investigating the composition-performance relationship and revealing the role of individual elements via correlative microscopic techniques.

1.1 Chemical Flexibility of ABX_3 Hybrid Perovskites: A large design space to tune functional properties

Hybrid perovskites are a broad family of inorganic-organic compounds that expand the material design space in the familiar ABX_3 perovskite crystal structure,[20] which includes the widely-studied inorganic oxide perovskites ABO_3.[21, 22] The primitive crystal structure of the most studied hybrid lead halide perovskite today, methylammonium lead iodide $CH_3NH_3PbI_3$, is shown in Figure 1.2a, where A-site cation, B-site cation and X-site anion, are $CH_3NH_3^-(MA^-)$, Pb^{2+}, and I^-, respectively. Here we discuss the evolution in chemical composition of hybrid perovskite optoelectronic materials from $CH_3NH_3PbI_3$, trending away from single cation (A-site) and halide (X-site) chemistry to triple/quadruple cations and mixed halide composition to enhance device performance and long term operational and environmental stability.[12, 23, 11, 24, 25]

Hybrid perovskite materials combine functional advantages of both inorganic and organic semiconducting materials. The introduction of an organic cation on the A-site to create the hybrid organic-inorganic material may contribute to unusual defect-tolerance[26] but rather depends on charge-carrier separation at the conduction and valence band edges as in inorganic materials. The inorganic framework of PbI_6 octahedra is formed due to strong lead-halide ionic interaction; and the electronic structure of perovskite is mainly constituted via this interaction, where the valance band is composed of Pb (*6s* orbital) and I (*5p* orbital) anti-bonding states, while the conduction band is attributed mainly to anti-bonding states of Pb (*6p* orbital) and I (*5p* orbital) interaction.[27, 28] Optoelectronic investigations have focused on semiconducting lead halide perovskites, though extensive previous work in metallic stannous halide perovskites highlighted their exceptional electronic properties.[29, 30] Recently, lead-tin alloys have also been pursed to reduce the bandgap toward optimal terrestrial values.[31, 32] This thesis focus here on the lead halide perovskites, given the explosive growth in recent work on their optoelectronic functionality.

Goldschmidt's tolerance factor (t) has been demonstrated to be a valuable approach

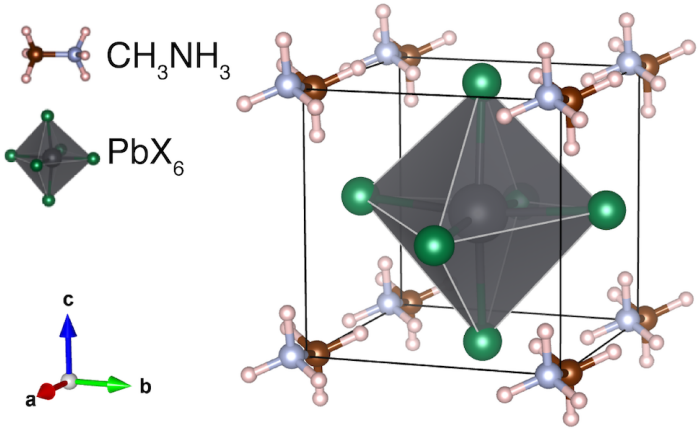

Figure 1.2. A cubic unit cell of a hybrid methylammonium lead halide perovskite, with general ABX_3 chemical formula.

for evaluating the formability of existing and as-yet-undemonstrated perovskite compositions. In 1926, Goldschmidt developed the tolerance factor to estimate whether a specific elemental composition can exist within the perovskite structure on the basis of elemental ionic radii and crystal geometry.[33] As the hybrid perovskite material systems attracts increased attention, it encourages scholars to investigate undiscovered perovskite materials that may have potential to be excellent electronic, magnetic, or optical materials. Recently, Kieslich *et al.* calculated the ionic tolerance factor for over 2300 amine-metal-ion permutations, indicating roughly 742 compositions would adopt the perovskite structure.[34, 35] Within these compositions, one seventh are known to be suitable for electronic applications.[34] The octahedral factor, derived from the radius ratio rules of Pauling,[36] provides an additional easily-calculated and necessary criterion for the formability of halide perovskites.[37] In addition to the crystal geometry and ionic radii considerations, oxidation state of A-site cation is recently being incorporated in an improved tolerance factor (τ) calculation to help predict perovskite stability.[38] The improved tolerance factor established by Bartel *et al.*, appears to correlate linearly with decomposition enthalpies ΔH_d calculated by density functional theory,[38] which has great potential to provide critical insight into the phase stability of predicted perovskite phases and help identify promising candidates for experimental demonstration and testing.

Tolerance factor calculations provide a framework to understand the current landscape of hybrid perovskite compositions, and they illustrate the chemical flexibility of perovskites. Figure1.3a displays a color map of tolerance factor for Pb^{2+} B-site cation perovskites using a non-modified Goldschmidt equation, covering wide range of A-site cations from K^{+} to formamidinium (FA) ion and X-site anions from fluoride to iodide. The Shannon's ionic radii are used in the tolerance factor calculation.[39] The calculated tolerance factor span 0.75 to 1.05, where the tolerance factor of photoactive black phase hybrid perovskite is commonly found within the range of 0.83 to 1.06(*e.g.* the orange and yellow color regions in Figure 1.3a).[12] The values of the tolerance factor indicate the structural formability of the hybrid perovskite is dominated by the size of large A-site occupants in lead perovskites, in which the photoactive phase is unlikely to form using A-site cation with ionic radius smaller than Rb^{+} cations. Similar trend is predicted using the improved tolerance factor τ, but with a narrower formability window ($\tau < 4.18$ shown in Figure 1.3b), where black phase perovskite is limited to cation with size bigger than Cs^{+} ion. The prediction from τ agrees well with the most of experimental findings.[40, 41] The formability of photoactive perovskites strongly depends upon the A-site ionic radii as illustrated in the tolerance factor estimation. However, the optical properties of the 3-dimensional (3D) hybrid lead perovskite do not show a strong dependence on different A-site ion composition[42] but can be fine tuned by X-site halide mixing.[9] The functionality of X- and A- site ions will be discussed in further detail in Chapter 1.2 and 1.3, respectively.

1.2 Tunable optoelectronic property in mixed halide compositions

Substitution of different halide anions within the 3D perovskite structure, enables us to tune the perovskite materials' optoelectronic properties significantly resulting in variation of absorption coefficient of thin films.[15] Changes to the lead halide bonding,[43] which

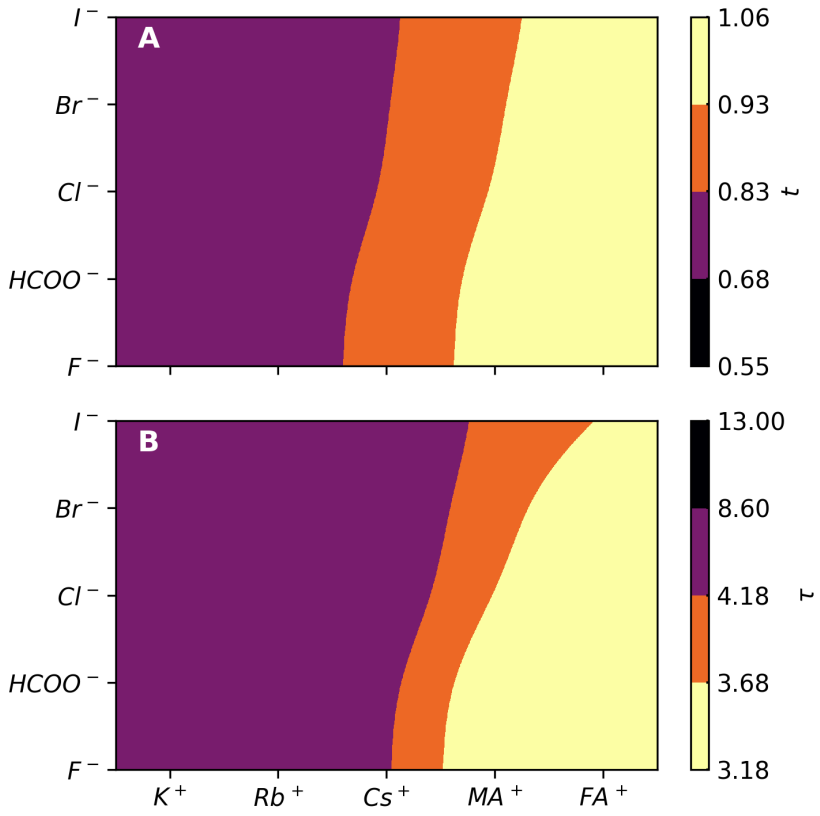

Figure 1.3. (A) Non-modified Goldschmidt's tolerance factor (t) and (B) improved tolerance factor (τ)[38] for a range of hybrid perovskites using Shannon's ionic radii,[39] including A-site cations from K+ to formamidinium (FA^+) and X-site anion from F^- to I^-.The purple regions in both (A) and (B) are the windows that photoactive lead perovskites are unlikely to form, while the formable regions are indicated in orange and yellow color.

contributes the valence and conduction band density of states, lead to sensitive changes in the functional capability of the perovskite.[44, 45] The absorption wavelengths, of different halide film compositions upon substituting I^- with Br^-, can be fine-tuned in the range of 800 nm to 520 nm by having the appropriate Br to I ratio.[15] The absorption spectra clearly indicate the optoelectronic tunability that emerges from the structural flexibility of hybrid perovskites. In the early stage of the hybrid perovskite development, different halide compositions, ranging from single halide (Cl, Br, and I) to mixed halide Br/I,[15, 46, 47] were explored extensively while fixing the A-site cation for pursuing the better fine-tuned optoelectronic properties. Impressively,

the structural flexibility extends to post-fabrication chemical modifications, including gas-solid heterogeneous reactions. For example, Solis-lbarra *et al.* found that $MAPbI_3$ perovskite films can undergo halide conversion/exchange after exposure to Br_2 or Cl_2.[48] This observation indicates the structural flexibility of $MAPbI_3$ thin films but also suggests the instability of the material itself.[49, 50] Incorporation of a small but increasing Br fraction relative to I promotes better environmental stability for MA based perovskite devices.[51] The PCE of mixed halide $MAPbI_{3-x}Br_x$ devices, where x = 0.20 and 0.29, display almost no PCE decrease after storing for 20 days at 35% humidity, while the PCE of the triiodide system drops from 11.2% to 2.5%.[9]

However, this mixed halide composition appears to have poor photostability upon laser/light illumination resulting in a shift in the photoluminescence (PL) peak from 635 nm to 730 nm[15]. Shift in PL peak position suggests the occurrence of photoinduced phase segregation, resulting in I- and Br- rich phases formation. This observation can be attributed to the metastable nature of the mixed halide systems which leads to gradual deterioration by thermal or optical energy inputs,[52, 53] or the instability from the mobile halide ions.[54] To improve the long-term photo- and environmental stability in mixed Br/I phases, mixed A-site cations were introduced to the mixed halide hybrid perovskite which is discussed in the following chapter.

1.3 A-site compositional engineering improves performance and stability

Although A-site cation does not impact the electronic structure of the materials directly, it serves an important component in determining the formability, dimensionality, and stability of perovskites.[55, 20] Expanding beyond the 3D perovskite structure through the incorporation of larger A-site cations can vastly broaden the structural and functional design space of hybrid perovskites,[20] though the highest performing hybrid perovskite solar cells to date are the 3D perovskites. The dimensionality of the perovskites can be tuned from 2D[56, 57] to Ruddlesden-Popper quasi-2D [58, 59] to fully 3D perovskite structures by incorporating larger organic

A-site molecules such as 2-phenylethylammonium (PEA) or n-butylammonium (n-BA).[60, 61] In the 3D perovskite framework, the commonly used A-site cations (methylammonium or formamidinium) reside in the cages formed by the corner sharing PbX_6 layer networks. In contrast, the 2D structure can be regarded as n number of octahedral perovskite layers sandwiched top and bottom by two layers of larger A-site organic cations. These large organic molecules, also known as organic spacers, prevent the continuous growth of perovskite 3D lattices resulting in a quasi-2D layered structure with a mixture of organic spacers and perovskite domains.

The addition of the longer-chained hydrophobic cations has been shown to offer greater environmental stability to the hybrid perovskite.[62] State-of-the-art low-dimensional Ruddlesden -Popper quasi-2D perovskite solar cells, with composition of $PEA_2MA_{n-1}Pb_nI_{3n+1}$ ($n = 5$), exhibit decent performance with 18.04% PCE along with 8-month long term stability.[63] Additionally, the large organic cation salt can be added directly to 3D perovskite solution, in which the final perovskite films have formation of 2D perovskite platelets interspersed between 3D perovskite grains, providing potential benefits of improving crystallinity of 3D perovskites, passivating grain boundary passivation, and enhancing environmental stability.[64] Recently, 2D perovskite can also be deposited as the interlayer, between 3D perovskite absorber and charge-transport layer, for lowering defect densities and improved carrier lifetime.[65, 66]

Furthermore, A-site engineering for 3D perovskites involves mixing small organic A-site cations(MA^+,FA^+) in tandem with incorporating inorganic A-site cations have shown great promises in achieving highest performance PV applications with decent stability to date. The poor intrinsic stability of hybrid perovskite appears to originate from the weak stability of MA as it gradually decomposes to HI and CH_3NH_2, leaving inactive PbI_2 behind.[67] Remarkable advances have been achieved by precise compositional engineering though substituting unstable MA^+ with relatively stable FA^+ . First, the addition of $MAPbBr_3$ to $FAPbI_3$ in small quantities has been demonstrated to produce better film coverage and stabilization of $FAPbI_3$ (nominally, outside the perovskite formability window, Figure1.3) achieving a PCE of 17.9% by Jeon *et al.* with $(FAPbI_3)_{0.85}(MAPbBr_3)_{0.15}$[68] and 22.1% by Yang *et al.* using an optimized

$(FAPb_3)_{0.95}(MAPbBr_3)_{0.05}$ with additional iodide ions in organic cation precursor solutions.[69]. For inorganic cation incorporation, selection of inorganic monovalant ions is limited according to prediction from tolerance factor (shown in Figure1.3), and Cs^+ appears to be the only one being able to be incorporate into perovskite structure. Choi *et al.* demonstrated Cs incorporation in $MAPbI_3$, creating mixed Cs/MA lead iodide perovskites, resulting in stable perovskite films reaching to 7.68 % PCE.[70] The Cs/FA lead iodide compositional space was explored by Lee *et al.*, who found that substituting a small amount of Cs helps to not only stabilize the photoactive black phase of $FAPbI_3$ but also improve the PCE from 16.3% to 17.1 %.[71] The presence of Cs and its effect on $FAPbI_3$ phase stabilization can be understood on the basis of entropic stabilization and the Goldschmidt tolerance factor.[72, 73] The mixed Cs/FA cation chemistry exhibits significantly improved environmental stability with respect to $FAPbI_3$, maintaining 70 % of the initial device performance after 220 hours of continuous light exposure while the pure FA cation lead iodide perovskites do not operate after 70 hours in the same testing conditions.[71] In the mixed Br/I space, 25% Cs concentration in $Cs_{0.25}FA_{0.75}Pb(Br_{0.20}I_{0.80})_3$ composition space suppresses photoinduced halide segregation and yields 17.4 % PCE.[74] Similar compositional space with $Cs_{0.17}FA_{0.83}Pb(Br_{0.17}I_{0.83})_3$ has shown to withstand damp heat and thermal cycling with careful encapsulation.[75]

These promising mixed inorganic-organic A-site investigations motivated novel hybrid perovskite chemistries combining triple A-site cations (Cs^+, MA^+ and FA^+) and mixed halides. Saliba *et al.* achieved 21.2% efficiency that was maintained over 250 hours under constant illumination at room temperature in a nitrogen atmosphere.[11] Later, Christians *et al.* demonstrated more than 1000 hour operational stability using CsFAMA triple cations in mixed halides composition.[76] Expanding the design space further, Saliba *et al.* incorporated a fourth A-site cation in small quantities, Rb^+, in quadruple cation (Rb^+, Cs^+, MA^+ and FA^+) mixed A-site Br/I halide perovskites, yielding chemistry of $Rb_{0.05}(Cs_{0.05}(MA_{0.17}FA_{0.83})_{0.95})_{0.95}Pb(I_{0.83}Br_{0.17})_3$, to achieve yet higher photovoltaic performance of 21.6%, improved reproducibility, and further improved stability.[12]

With rapid advances in the chemical complexity of hybrid perovskite materials, how the mixing of organic and inorganic rubidium/cesium cations on the A-site and the mixing of halides on the X-site impact charge collection at the nanoscale remained open questions. In this thesis, I narrow our focus to the relationship between nanoscale chemistry and charge-collection properties of 3D hybrid perovskites with mixed organic-inorganic A-site and mixed halide devices, as they have exhibited the highest performance in optoelectronic applications to date.

1.4 Thesis overview

The goal of this research is to reveal the composition-performance relationship of and further elucidate the role of each element in complex halide perovskite absorbers. To accomplish this objective, the development of *operando* synchrotron-based microscopic techniques is pursued, providing an optimal window to avoid degradation during characterization and enabling collection of both chemical and electronic information. Along with establishing quantitative methods for analyzing the compositional data, synchrotron-based microscopic investigations of chemical determinants of local performance using a wide range of perovskite composition chemistries are conducted in various device architectures.

In Chapter 2, I detail the characterization method for performing synchrotron based X-ray as well as electron-beam (E-beam) based microscopy, along with the data analysis approaches to extract the collected elemental and electronic information. This chapter also highlights useful characterization guidance and provides the optimal windows to avoid degradation during E-beam and X-ray beam characterizations.

With the optimal characterization window established, in Chapter 3, I perform the first microscopic assessment on composition-performance relation in mixed halide perovskites, by means of X-ray fluorescence (XRF) and X-ray beam induced current (XBIC) microscopy. The XRF/XBIC result reveals the potential challenge of the spatial heterogeneous halide distribution in the widely used mixed halide composition. The elemental information from XRF combined

with the electronic information from XBIC highlights the importance of local chemical stoichiometry on local charge collection. The resulting halide segregation is potentially due to the ionic size difference of halides or the highly mobile nature of the halide ions shown in Chapter 4.

To avoid the halide segregation observed in Chapter 3 and 4, high performing A-site modulated perovskite devices using single halide chemistry are prepared and investigated in Chapter 5. Although the halide segregation problem is avoided, this composition is limited by A-site stability upon accelerated testing under heat and light.

Lastly, one of the most promising perovskite compositions is explored in Chapter 6, composed of mixed halides and A-site (with alkaline ions). In this relative complex composition, adding alkaline ions help homogenize halide distribution, which leads to enhancement in both performance and stability observed in the perovskite community.

Chapter 7 summarizes the results and conclusions, along with the future outlook in engineering stable and high performance halide perovskites solar cells from my perspective.

1.5 Acknowledgement

Chapter 1, in part, is a reprint of the material "The Relationship between Chemical Flexibility and Nanoscale Charge Collection in Hybrid Halide Perovskites" as it appears in Advanced Functional Materials, Yanqi Luo, Sigalit Aharon, Michael Stuckelberger, Ernesto Magaña, Barry Lai, Mariana I. Bertoni, Lioz Etgar, and David P. Fenning, 2018, 28 (18), 1706995. The dissertation author was the primary investigator and author of this material.

Chapter 2

Methods and X-ray/Electron-beam Microscopy Development

Perovskite absorbers exhibit significant compositional and structural heteroeneities on a variety of length scales,[77] which can lead to either performance enhancement [78] or device instability.[40] Thus, micro- and nanoscale characterization is necessary to provide deeper insights on the origins of heterogeneity and reveal the degradation mechanisms in halide perovskites. Techniques utilizing focused electron beam (E-beam) and X-ray beam offer unique advantages toward understanding the nanoscale variations for both chemical and optoelectronic properties. E-beam and X-ray microscopy has readily developed and shown great success in characterizing semiconducting materials such as silicon, which can be exploited on hybrid halide perovskite characterization as well.

In this chapter, I will first introduce synchrotron based X-ray fluorescence (XRF) microscopy and the associated data analysis procedure for obtaining quantitative compositional information from samples. Next, I will discuss the physical mechanism, benefits, and operational limits of the *operando* X-ray beam induced current (XBIC) technique for collecting electronic information on perovskites. Lastly, since working with hybrid halide perovskites comes with additional difficulties due to their radiation sensitive nature,[79] a quantitative specification during E-beam measurement is provided with insights on underlying perovskite degradation mechnisms during E-beam perovskite interactions.

2.1 Mapping Elemental Distribution via Synchrotron-based X-ray Fluorescence (n-XRF)

Micro- or nano- probe X-ray fluorescence (XRF) microscopy has large contribution in identifying the impact of trace amount metal impurities related failure modes in semiconducting devices.[80, 81, 82, 83] In single- and multi- crystalline silicon, transition metal impurities can dissolve or precipitate to form metal silicides, which can result in active carrier recombination centers and lead to shorten carrier diffusion length and reduce carrier collection.[84] McHugo *et al.* first utilized synchrotron based μ-XRF at Advanced Light source at Lawrence Berkeley National Laboratory to report the present of nanometer-scale metal precipitates (Fe, Cr, Ni, Cu, and Au) in multicrystalline silicon (mc-Si) solar cells.[85, 86] Buonassisi *et al.* and Istratov *et al.* later found that performance of mc-Si cells were limited not only by the total metal concentration but also the distribution of metal clusters within grains or grain boundaries.[87, 88] These microscopic learning have revealed the chemical and electronic nature of the nanoscale impurities or variation in composition, which are essential to evaluate the composition-performance relation. Leveraging on the readily developed XRF microscopy, elemental distribution in halide perovskites and its impacts on local electronic performance can be unlocked.

X-ray fluorescence (XRF) microscopy provides mapping of elemental composition, achieving better than part per million sensitivity and sub-30 nm resolution.[90] The basic requirement of X-ray microscopy is a bright X-ray source, most commonly found at a synchrotron facility, that allows the beam to be focused into small spot size using X-ray optics. The most common nano-focusing approach is to use a Fresnel Zone Plate shown in Figure 2.1.[90, 91, 92] Rastering the sample or the X-ray optic using precision nano-positioning stages enables high-spatial resolution scanning X-ray interrogation of materials. Then, the detection of XRF signal relies on the emission of elemental characteristic X-ray photon by relaxation of an outer-shell electron to the core-hole generated upon X-ray absorption. The basic physical mechanism of XRF is illustrated in Figure 2.1. The process begins first with the creation of a core-hole (*e.g.* in

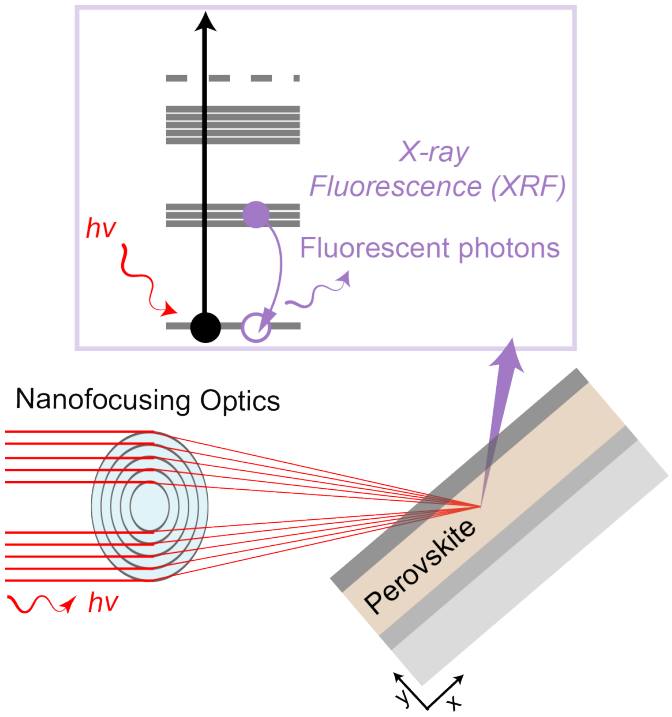

Figure 2.1. X-ray fluorescence operates by a mechanism where an X-ray photon of high enough energy removes a core-shell electron, and the core-hole is filled by relaxation of one of an outer shell electron with energy conserved by fluorescent photon emission.Reproduce from [89]

the K, L, or M shell) by absorption of an incident X-ray photon of energy greater than the binding energy of an electron in that shell. Outer-shell electron relaxation can occur by multiple pathways including Auger electron emission or the emission of various characteristic fluorescent X-rays shown in Figure 2.2. The energy of the fluorescent X-ray photon is dictated by conservation of energy between the electronic transition's initial state and its final state. Dipole selection rules determine which transitions are quantum mechanically allowable, and each is characteristic of the absorbing atomic species. Typically conducted in a 2D mapping mode, the collected XRF signal is a 2D projection of the three-dimensional distribution of XRF emission integrated from the surface into the bulk of the sample.

Synchrotron XRF enables rapid, sensitive, and spatially-resolved mapping of composition in samples of various geometries and architectures. Though XRF provides information seemingly analogous to that of energy dispersive X-ray spectroscopy (EDX), a widely available electron

microscopy-based technique for compositional analysis, XRF offers several distinct advantages over EDX. Deceleration of electrons within a sample during EDX measurements generates white Bremsstrahlung background radiation, limiting sensitivity to 0.1% [93] - a limitation not present in XRF, which uses photons as an excitation source, and accordingly has about 1000x the sensitivity of EDX. This boost in sensitivity not only reduces measurement time and energy dose imparted to a sample, but actually allows lower-energy emission weaker L- or M-lines that would typically be masked by EDX background to be used for analysis. EDX measurements also often require incident electrons to have an energy 3-5 times higher than the binding energy of core-level electrons to have acceptable characteristic fluorescence photon signal, [94] which can be particularly damaging to beam-sensitive perovskite materials. XRF is a dose-efficient photon-in, photon-out technique in which little excess energy for the incident X-ray beam is required above the absorption edge of interest. Spatial resolution in SEM-EDX is typically limited to 0.5-1 μm by broadening from the electron interaction volume, though this limit is lifted in TEM-EDX by the thin sample thickness (¡100 nm). XRF resolution can reach 10-30 nm at state-of-the-art facilities, primarily determined by the spot size of X-ray nanoprobes. Critically, the long penetration depth of X-ray beams allows us to measure buried layers in a multilayer device such as a solar cell (Figure 2.1), enabling compositional mapping at high resolutions in extended samples. Overall, the dose efficiency and information depth of XRF unlock compositional characterization in beam-sensitive materials like lead halide perovskites.

2.1.1 Performing XRF Measurement on Halide Perovskite

Consideration in choosing the appropriate incident X-ray beam energy and awareness of potential overlapping emission peaks is crucial. This is particularly essential in the mixed halide and mixed A-site absorbers as mentioned in Chapter 1.2 and 1.3. Figure 2.2 displays an exemplary XRF spectrum of a $Cs_{0.1}FA_{0.9}PbI_3$ perovskite solar cell in the common double-heterostructure architecture, in which the perovskite layer is sandwiched between electron transport layer (ETL, SnO_x) and hole transport layer (HTL, Spiro-OMeTAD). After the carrier

selective contacts, the holes and electrons are extracted using Au and indium tin oxide current collector (ITO), respectively. This yields a common layered stack of perovskite device of ITO/SnOx/perovskite/Spiro-OMeTAD/Au. Here, the 7 keV X-ray beam impinges upon the back side of the sample, penetrating through the thin Au back-contact and Spiro-OMeTAD overlaying layers, the absorber, tin oxide, and into the substrate. Due to long penetration length of X-rays and bright synchrotron radiation, all elements from the individual layers in the stack are detectable, with the exception of low-Z elements (less than Na and including H, C and O) due to their low fluorescence yield.[95] The emitted X-ray photons are named in a hierarchical scheme where the first letter (K, L, M) defines the core-hole level. A Greek letter and number specify the original orbital of the electron that relaxes, with transitions labeled α, β, and γ, in order of increasing transition energy with finer orbital angular momentum differences denoted using subscripts 1,2, etc.[96] As illustrated in Figure 2.2 a, relaxations within a single atom to fill a core-hole can be complex because more than one electron is available to fill the core-hole and emit the fluorescence X-ray photons. Fuggle *et al.* summarized the electron binding and X-ray emission energies in metals as a function of atomic number (Z),[97] which is included in the booklet "X-Ray Data Booklet"[98] serving as a valuable resource for quick reference and providing guidance in selecting the incident beam energy.

As is evident from the overlapping peaks in Figure 2.2 b, careful data analysis is required to extract quantitative elemental concentrations from raw XRF signal in halide perovskites, particularly in strongly overlapping regions, such as the energy range of 3-5 keV where emission lines from I_L, In_L, and Sn_L overlap.[98] It is crucial to select the most favorable L-lines for data quantification and apply rigorous spectral fitting routines that deconvolute overlapping emissions and background from the spectra.[99] The fitted elemental concentrations can be quantified using NIST-traceable XRF standards with 5-10% uncertainty in elemental concentration. To obtain the most accurate quantification, XRF standards are measured as soon after sample XRF data collection as possible in the sample-detector position/geometry. An optimistic lower bound error is 10% after all accounting for the propagated errors during data quantification.[100] This

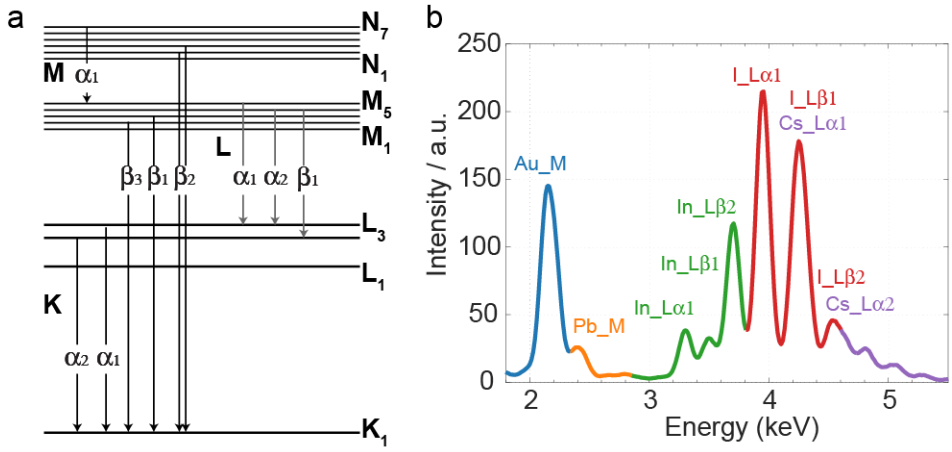

Figure 2.2. Elemental characteristic X-ray photons and their associated energy level.[89] (a) X-ray fluorescence operates by a mechanism where a high intensity X-ray beam removes a core-shell electron and the core-hole is filled by relaxation of one of an outer shell electron. (b) A representative XRF spectrum taken on a layered stack perovskite solar cells with device architecture of ITO/SnOx/perovskite/Spiro-OMeTAD/Au. The elemental specific fluorescence photons emitted are detected and produce an XRF spectrum of elements along the beam path.

quantification uncertainty strongly depends on the concentration of the element of interest and the layer architecture of sample or cell stack. Attenuation of both incident and outgoing X-ray photons within the sample should be accounted for systematically.[101, 102] The elemental quantification of perovskites is further challenging because many emission lines are far in energy from typical NIST standards (primarily for 3*d* transition metals), requiring calibration of yields and branching ratios. An approach to simplify the quantification process is to use a well-characterized perovskite sample – ideally a single-crystal perovskite with known composition and comparable thickness to the perovskite sample of interest – as a standard, allowing direct conversion of XRF counts into estimated elemental composition.[40, 100]

2.1.2 XRF Data Analysis and Interpretation

Since it is often a challenging to fabricate and handle single-crystal with comparable thickness to its sub-micron layer thickness in device, XRF data analysis to account for signal attenuation in highly absorbing Pb-containing perovskite films is crucial to avoid misinterpretation

of the XRF results. According to Beer Lambert's law, the attenuation of light intensity within a medium at a fixed X-ray photon energy is expressed:

$$I = I_o exp(\frac{-t}{\lambda_i cos\alpha}) \tag{2.1}$$

where I_o is the incident intensity of light, λ_i is the attenuation length of incident X-rays, t is the depth and α is the incident angle with respect to the sample normal. Then, the intensity of fluorescent X-rays emitted at the given depth that reaches the detector is:

$$Q(\frac{\Omega}{4\pi})I_o exp(\frac{-t}{\lambda_i cos\alpha}) \tag{2.2}$$

where Q is the fluorescence yield describing the emission probability of the fluorescent photons and Ω is the solid angle defined by the detector collimator. Since fluorescence radiation is emitted uniformly in every direction, the term $\Omega/4\pi$ is used to account for the fraction of fluorescent signal that makes it to the detector.[103] Considering the outgoing fluorescent signal is attenuated by the absorber along the beam path, with a factor of $exp(\frac{-t}{\lambda_y cos\beta})$,[104] the intensity of the XRF signal is given by the following equation:

$$I_y(t) = \int_0^{t_{film}} I_o Q \frac{\Omega}{4\pi} exp(\frac{-t}{\lambda_i cos\alpha}) exp(\frac{-t}{\lambda_y cos\beta}) dt \tag{2.3}$$

where λ_y is attenuation length of element-specific fluorescent photons and β is the detector angle with respect to sample normal.

Using the relationship established in Eq 2.3, the total XRF signal attenuation due to self-absorption can be estimated. In this analysis, we assume the incident intensity of X-ray beam, sample-detector geometry and fluorescence yield remain unchanged, and that the element-specific attenuation factor α_y is expected to be proportional to overall attenuation of fluorescent photons that are collected at the detector as shown in Eq 2.4. Then, the attenuation corrected

elemental signal equals to $I_{measured}/a_y$, where $I_{measured}$ is the raw XRF intensity.

$$\alpha_y(t) \propto \int_0^{t_{film}} exp(\frac{-t}{\lambda_i cos\alpha}) exp(\frac{-t}{\lambda_y cos\beta}) dt \tag{2.4}$$

Figure 2.3 illustrates the estimated attenuation factor α_y at various film thicknesses using X-ray beam at 13.6 keV with α and β equal to 15° and 75°, respectively. At 13.6 keV, the X-ray beam allows the emission and detection of Br_{K_α}, Pb_{L_α}, and I_{L_α}, which are the three major elements detectable by XRF in perovskite absorber. The attenuation factor of Br_{K_α} ($E_{Br_{K_\alpha}}$ = 11.92 keV) and Pb_{L_α} ($E_{Pb_{L_\alpha}}$ = 10.45 keV) appear to be very similar in the given thickness window. In contrast, signal I_{L_α} is being attenuated more and requires a larger correction factor using $1/\alpha_y$. Note that the attenuation length of element-specific X-ray photons is estimated based on the X-ray interaction with perovskite absorber, $FAPbI_{2.25}Br_{0.75}$.[105]

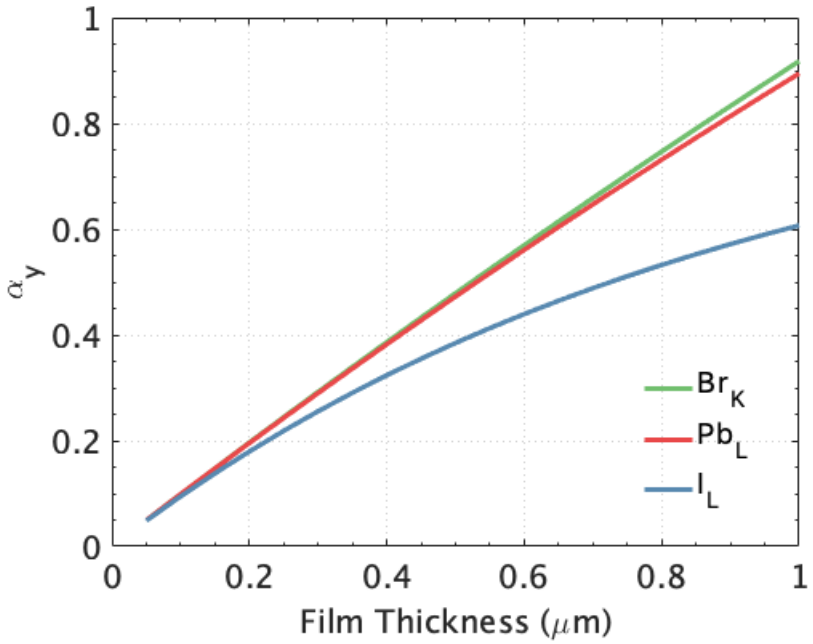

Figure 2.3. Estimating attenuation factor for $FAPbI_{2.25}Br_{0.75}$ absorber using 13.6 keV X-ray beam. The estimation is calculated using relation in Eq 2.4 with sample-beam geometry of α and β of is 15 and 75°, respectively.

Due to the significant self-absorption of iodine signal shown in Figure 2.3, it's important

to implement this correction on perovskite films to avoid misinterpretation of the chemical environment of iodine, between PbI_2 precursor and $APbI_3$ perovskite composition as the difference of Pb:I ratio is within the magnitude of self-absorption. Thus, removing the impact of self absorption on the collected signal is one of the essential steps while quantifying the XRF data.

2.2 Probing Local Electronic Performance using X-ray Beam Induced Current (XBIC)

In addition to obtain composition information (*e.g.,* Chapter 2.1), the same X-ray micro- and nanoprobes can characterize local electronic properties of semiconducting devices such as solar cells.[106, 88, 107] The collected signal of X-ray beam induced current (XBIC) involves not only the process of generating electron-hole pairs but also the collection of the excited carriers. As shown schematically in Figure 2.4, the highly energetic electrons excited by X-ray absorption can decay by a cascade of secondary interactions, ultimately resulting in the generation of a large number of band-edge charge carriers for each absorbed X-ray photon in an internal carrier amplification process.[108] During XBIC measurement, these excited carriers drift/diffuse, are separated via junctions and are ultimately collected at device contacts. The current is amplified externally to produce an XBIC signal.

Compared with other beam induced current techniques such as electron-beam induced current (EBIC), XBIC offers unique capabilities and advantages due to the particular X-ray-matter interaction. One obvious advantage of utilizing XBIC is the long penetration length of hard X-ray photon. This allows a large fraction of incident X-rays to interact with the buried layer of interested in a layered stack device. Along with smaller interaction volume by X-ray with respect to electron-beam,[89] *operando* beam induced current studies are achievable using X-ray nanoprobe. For example, XBIC is often exploited in conjunction with compositional (XRF)[109] or structural (X-ray diffraction, XRD) information.[110], providing further insights on the root cause of detrimental/enhanced electronic performance.

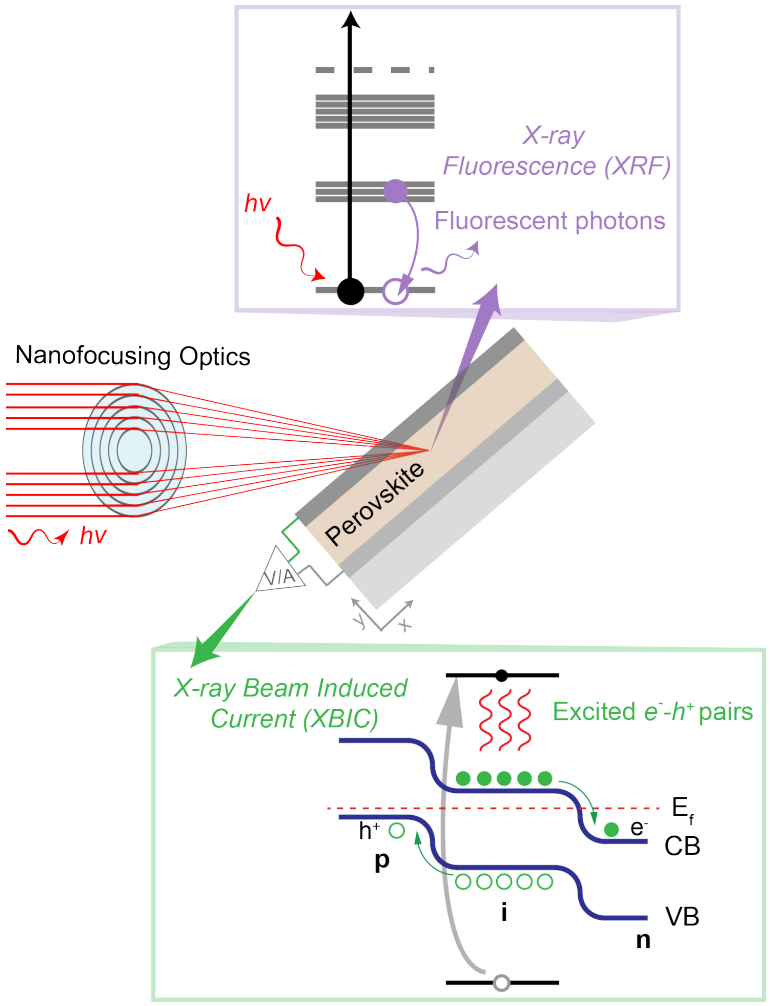

Figure 2.4. X-ray micro- nanoprobes can extract composition and electronic information simultaneously. X-ray beam induced current (XBIC) measures current collection of the band-edge electron-hole carriers resulted from the cascading secondary interaction following the primary core hole generation. Reproduce from [89].

2.2.1 Performing XBIC Measurement on Perovskite

Unlike n-XRF measurement, electronic performance characterization on the nanoscale is often challenging on hybrid halide perovskites, as shown in Figure 2.5. The characterization windows for n-XRF was first compiled by Stuckelberger *et al.*, in which there were no changes in X-ray elemental mapping after five repeat scans under high X-ray flux density in $MAPbI_3$ absorbers.[111] Although the composition extracted from XRF has proven to be stable under

the high flux X-ray beam, atomic-scale defects are generated under X-ray irradiation. This leads to the exponential decay of the XBIC signal, which is similar to that observed in EBIC measurement as reported by Klein-kedem.[79] As a matter of best practice, care should be taken when characterizing beam sensitive perovskites in order to avoid the operation regime that the detected signal starts to vary significantly as a function of incident beam dose.

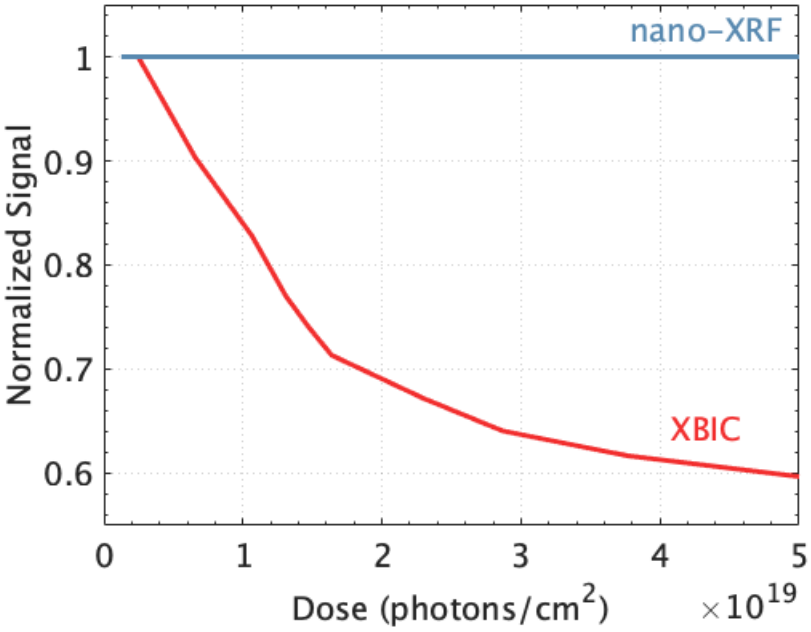

Figure 2.5. Signal decay as a function of dose for nanoprobe XRF and XBIC. The X-ray microscopy measurements were conducted using a 30×30 nm^2 focused beam with photon flux of 10^6 photon s^{-1} at 26-IDC nanoprobe beamline in Advanced Photon Source (APS). The characteristic decay of the XBIC signal was tracked using a $MAPbI_3$ perovskite absorber with a device architecture of FTO/meso-TiO_2/perovskite/Spiro-OMeTAD/Au.[111] The nano-XRF study was performed on hole transport layer (HTL) free $MAPbI_{3-x}Br_x$ device.[101] Reproduce from [89].

As rapid degradation of XBIC signal is seen during measurement, a two-step strategy is adapted to achieve successful n-XRF/XBIC measurement. We first perform an "electronic" measurement map, followed by an "elemental" map. For the electronic map, we combine high-throughput fly-scanning mapping that reduces scanning time to a typical 20-50 ms per point dwell time [112] and insert beam attenuation filters to reduce X-ray dose. This strategy

takes advantage of the $\sim 10^3$ multiplication factor of band edge electrons generated per single hard X-ray photon and the relative ease of low-noise amplification of pA current measurements. To filter the electronic noise further, lock-in amplifier to collect modulated XBIC signal.[113] However, the significant reduction in dose reduces our XRF elemental sensitivity. As necessary to improve our XRF signal-to-noise to strengthen any correlation between the nanoscale chemistry and the charge collection, following XBIC electronic measurement, we re-map the same area for X-ray fluorescence at full flux and typically with a larger per point dwell time ($\sim$ 150-250 ms) to achieve a high signal-to-noise ratio of the elemental distributions. These largely generalizable characterization strategies have enabled us to investigate the relationship between nanoscale chemistry and charge collection in the hybrid perovskites in the later chapters.

2.2.2 XBIC Data Analysis

To enable cross sample comparison, XBIC signal is often corrected to the extent possible for variations in X-ray absorption and subsequent carrier generation due to absorber thickness and morphology variation of the overlaying layers. Given long penetration length of X-ray ($>$ 2 μm, at 7 keV), which is far beyond the nominal perovskite thickness ($\sim$ 500-600 nm), local thickness variation can vary XBIC signal considerably since thicker absorber is likely to absorb more X-ray, leading larger amount of charge-carrier generation, than thinner sample. X-ray absorption as a function of thickness can be estimated according to Beer Lambert's law (*i.e.,* Eq 2.1). Since the active absorber is buried layer, the amount of incident X-ray photons reaches the absorber can be attenuated by the overlaying layer Au and Spiro-OMeTAD. Thus, to calculate the effective X-ray absorption, the signal attenuation at the overlaying layers should be considered. Assuming the incident flux is mostly absorbed by Au than Spiro-OMeTAD before it reaches perovskite, we can establish the relation based on Eq 2.1 to account for morphological variation in the overlaying Au layer as shown in Eq 2.5,

$$I_{absorbed}(t_{PSK}) = \int_0^{t_{PSK}} I_o exp(\frac{-t_{Au}}{\lambda_{Au}}) exp(\frac{-t_{PSK}}{\lambda_{PSK}}) dt_{PSK} \tag{2.5}$$

in which t and λ is the thickness and X-ray attenuation length, respectively. Leveraging on the accessibility of compositional information during *operando* XRF/XBIC measurement, thickness profiles, in the plan of measurement, of both Au and perovskite layers can be approximated. The detected elemental concentration in XRF maps are used to scale thickness approximation linearly, with the average of elemental counts in XRF matched to the nominal thickness of each layer using the expression below:

$$t_{PSK}(i,j) = \frac{I_{Pb}(i,j) + I_I(i,j)}{(\sum_{i=1}^{n}\sum_{j=1}^{m} I_{Pb}(i,j) + I_I(i,j))/nm} \cdot t_{nominal} \tag{2.6}$$

where i and j indicate the x- and y- coordinates of a 2D map, I_{Pb} and I_I are the corrected Pb and I XRF signals due to self-absorption using Eq 2.4, and $t_{nominal}$ is the nominal film thickness. The thickness profile of Au is obtained using a similar approach with the XRF signal of Au. With this normalization, we are able compare the performance of different perovskite devices and elucidate the impact of experimental variables/parameters on electronic properties.[114] To help better demonstrate this approach, an interactive Jupyter Notebook is provided on "Github".

2.3 Probing Carrier Collection using Electron-beam Induced Current (EBIC)

Similar as X-ray microscopy, electron-beam (E-beam) is known to be a strong probe to degrade perovskites rapidly. The formation of intermediate or degraded phases was evidenced in transmission electron microscopy (TEM) by the appearance of forbidden reflections in methylammonium lead iodide ($CH_3NH_3PbI_3$) after 1 min of continuous e-beam irradiation at 200 kV and 2 e/(Å^{2}s).[115] Methylammonium lead bromide ($CH_3NH_3PbBr_3$) has similarly been reported to lose crystallinity under an accumulated dose of 10 to 20 e/(Å^{2}s) at an e-beam voltage of 300 kV during high-resolution TEM (HRTEM) measurements.[116] Given the signal-starved nature of scattering experiments, structural characterization of perovskite materials using e-beam microscopies has often meant pushing the limit of detector capabilities and/or carefully tuning

beam conditions.

The electron-beam analogs of XBIC, electron-beam induce current (EBIC), can identify heterogeneous recombination activity and charge carrier collection due to composition variations, structural defects, or impurities.[117, 118, 119, 107] It can also provide valuable insights into understanding device operating mechanisms by identifying the location of charge-separating junctions in cross-section and enabling quantitative measurement of carrier diffusion lengths to those junctions.[120] Cross-sectional EBIC performed by Edri *et al.* confirmed the p-i-n operating mechanism in $MAPbI_{3-x}Cl_x$ perovskites,[121] whereas $MAPbBr_3$ cells were identified to operate as p-n junction type cells by Kedem *et al.* [122, 123] Plan-view EBIC can help demystify the role of chemical composition or structure defects on carrier generation and collection. For example, recently Rb-rich aggregates were found to be photoinactive and weakly recombination-active by plan-view EBIC in Rb-containing quaternary A-site perovskites.[40] Besides investigation of carrier collection heterogeneities, plan view EBIC can also be used to extract carrier diffusion length for both holes and electrons by capturing the carrier diffusion profile onto selective contacts, as recently quantified for mixed halide perovskites.[124]

Despite these pioneering studies, compared to traditional semiconducting materials,[117, 119, 125, 126] perovskite solar cells have seen relatively little application to date of EBIC, or correlative microscopy studies on devices incorporating e-beam characterization with other *ex-situ* characterization on the same areas because of the unique challenges presented by this class of materials, namely poor beam stability and related dose- and rate-dependent activation and decay effects. In this following chapter, we identify an experimental window where little e-beam induced degradation is seen in perovskite solar cells, as evidenced by the relative stability of the time-dependent EBIC current, which is sensitive to electronic defect concentration. We identify the accelerating voltage as the dominant parameter in determining the rate of damage to PSCs using EBIC measurements in plan view.

2.3.1 Determining Range of Accelerated Beam Voltage for Conducting Plan-view EBIC

For this investigation, a 16.8% triple-cation perovskite solar cell with nominal chemistry of $Cs_{0.05}(FA_{0.87}MA_{0.13})_{0.95}Pb(I_{0.83}Br_{0.17})_3$ (CsFAMA) in the common device architecture FTO/TiO_2/Perovskite/Spiro-OMeTAD/Au was selected due to its spatially-uniform initial EBIC signal across the device. Cell performance for the CsFAMA device is shown in Figure 2.6. Its spatially-uniform electronic response is in good agreement with recent results that indicate alkali-ion addition on the A-site homogenizes the absorber chemistry and carrier dynamics relative to alkali-free compositions.[40] Thus, the triple-cation absorber was used here to isolate the effect of beam conditions.

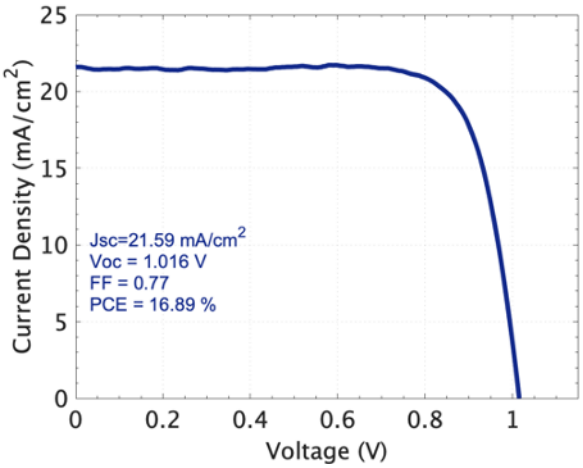

Figure 2.6. J-V curve of the triple-cation device used in the initial EBIC study.

The configuration for plan-view EBIC is shown in Figure 2.7 A, where the beam interacts with the absorber by penetrating through the backside Au contact and the hole transport layer (HTL, Spiro-OMeTAD). As shown in the schematic, when the device is contacted externally, excited carriers can be collected as electron beam induced current. We connect the device in short-circuit conditions to a pre-amplifier (Femto DLPCA-200) whose output is synchronized with the microscope scan generator using a Mighty EBIC 2.0 controller (Ephemeron Labs).

Monte Carlo electron trajectory simulations using CASINO [127, 128, 129] were used

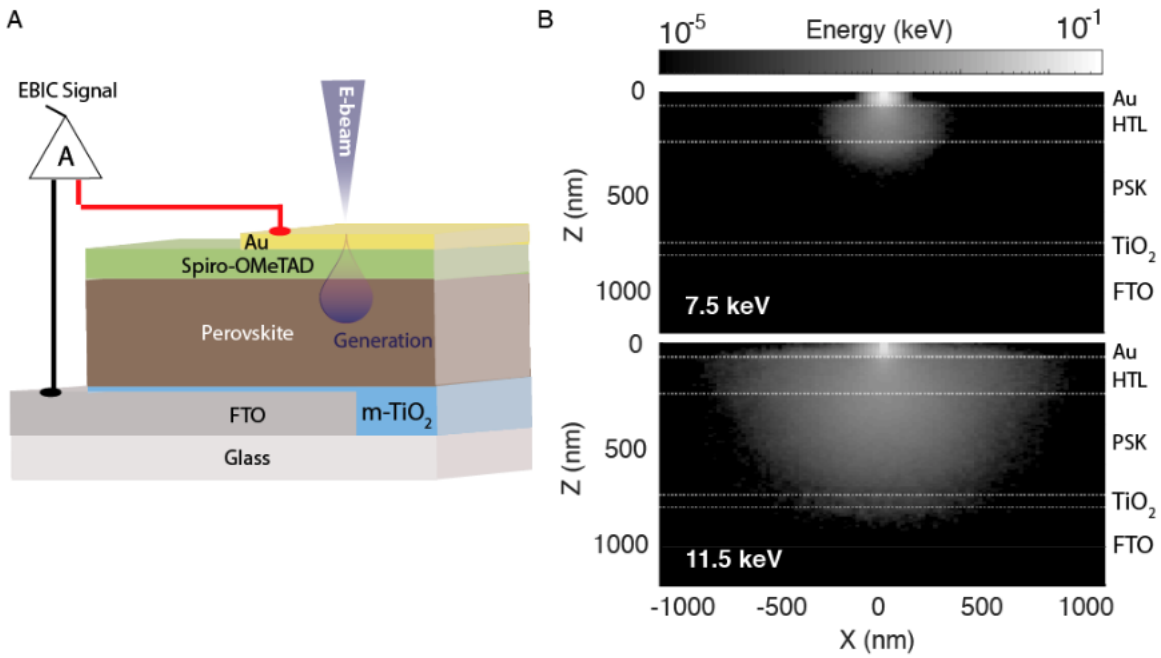

Figure 2.7. EBIC measurement configuration and simulation of energy deposited in perovskites. (A) Experimental setup of plan-view EBIC measurement. A beam voltage is chosen such that the e-beam penetrates sufficiently through the backside Au contact and excites carriers within the perovskite bulk. The charge carriers are collected via the selective contact layers, and this EBIC current amplified externally for detection. (B) Simulation of energy deposited in the device layers per incident electron at a beam voltage of 7.5 kV (top) and 11.5 kV (bottom).

to identify the range of acceleration voltages for which the electron beam probe reaches the perovskite beneath the overlying layers in the solar cell. A cross-section SEM image of the cell used is shown in Figure 2.8, from which layer thicknesses were extracted to construct an accurate device model for CASINO simulation. CASINO estimates the scattering, trajectory, and differential energy loss of electrons interacting with a given material from the probabilities of particular electron-matter interactions.[127] From the simulations, an operating window from 7.5 to 11.5 kV was established. The projected interaction volumes at 7.5 and 11.5 kV are shown in Figure 2.7 B, in which whiter pixels have higher energy deposited. The penetration depth is shallow at 7.5 keV, and the interaction volume just passes the HTL/perovskite interface. Conversely, a large interaction volume appears at 11.5 kV, extending just into the FTO. Thus, by examining accelerating voltages from 7.5-11.5 kV we can probe through the perovskite thickness.

Selecting beam currents near the lower limit of widely-accessible SEMs, an experimental matrix of beam voltages (7.5 to 11.5 kV with 1 kV increment) and beam currents (nominal currents: 6.3, 13, 25, 50 pA was identified for systematic investigation. A dwell time per point of 26.5 μs was used throughout.

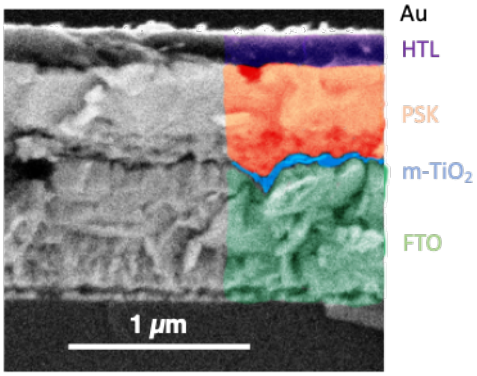

Figure 2.8. Cross-section secondary electron image of the CsFAMA device used in the EBIC study. Device architecture is FTO/meso-TiO_2/Perovskite (PSK)/Spiro-OMeTAD (HTL)/Au. The layer thickness estimated from the SEM is 70, 180, 500, 60, and 680 nm for Au, HTL, PSK, meso-TiO_2 and FTO respectively.

2.3.2 Three Operating Regimes: Activation, Quasi-Steady, Decay

At the lowest e-beam powers, we find a beam induced current activation similar to two previous reports.[79, 124] In Figure 2.9 A, three EBIC maps selected from a set of repetitive scans of the same area carried out at 7.5 kV and 6.3 pA are shown (Scans 1, 35, and 65). Under these conditions, the perovskite device starts with relatively low area-averaged EBIC current of 0.33 $\pm$ 0.06 nA. Over successive scanning, the map brightens, until after 35 scans, the highest EBIC signal is observed with an average of 0.48 $\pm$ 0.06 nA. The EBIC signal then gradually decays upon further scanning, as seen in the 65^{th} scan. Similar optoelectronic activation is observed in the visible light-perovskite interaction as well, such as PL enhancement after light soaking.[130, 131] The presence of activation response suggests either (1) the stabilization or filling of traps by photogenerated carriers or the incident electrons from the beam,[79, 132] (2) a consequence of lead halide formation and surface passivation after e-beam interaction,[133, 134]

and/or (3) the result of thermal annealing of the absorber by the beam.

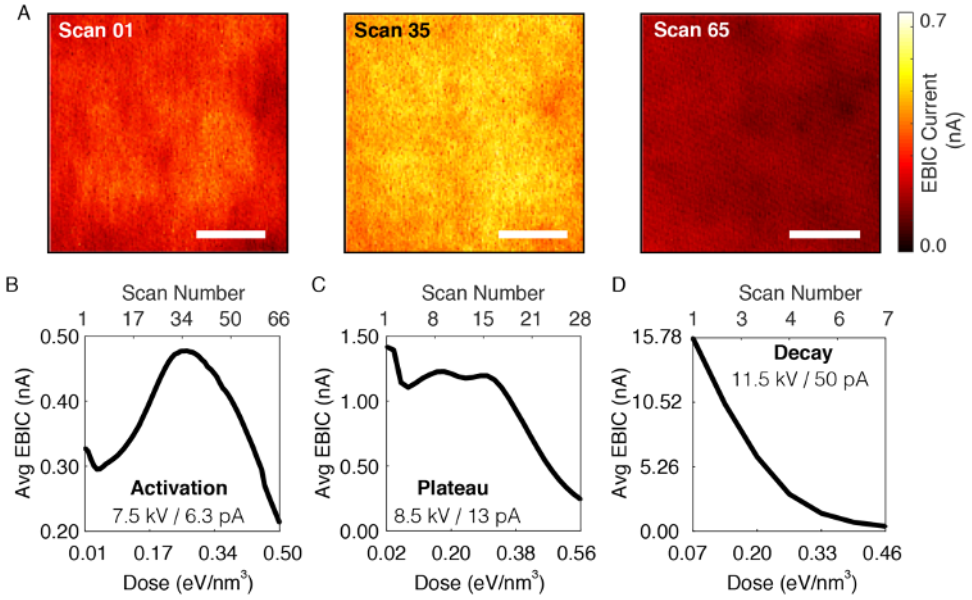

Figure 2.9. Type of EBIC responses at different beam power. (A) Selected scans from a time series of plan view EBIC maps showing the activation response of the CsFAMA-1s-Au device under 7.5 kV / 6.3 pA. Scale bar 10 μm. (B-D) Three characteristic EBIC profile showing activation, quasi-steady, and decay responses, obtained by plotting the average EBIC signal collected from the EBIC maps as a function of accumulated energy dose in the perovskite.

Under higher beam powers, we observe two distinct EBIC responses: at intermediate power we find a "quasi-steady" response before decay finally sets in, and finally at "high" power a direct decay of permanent degradation. The quasi-steady response is defined semi-quantitatively when the rate of change of EBIC signal as a function of dose has multiple inflection points shown in Figure 2.10, suggesting multiple reacting mechanism occurring simultaneously. Examples of the three EBIC responses observed are shown in Figure 2.9 B-D, where the average EBIC from successive maps is shown as a function of Scan Number (top axis) and energy dose absorbed in the perovskite normalized by the beam interaction volume in the perovskite layer (eV/nm^3) as calculated by CASINO simulation (bottom axis). This dose represents the volumetric energy density deposited in the perovskite and is used to examine dose effects as an intensive quantity. In Figure 2.9 B, the activation response from the same area shown in Figure 2.9 A is displayed, where the maximum EBIC current is collected during the 35^{th} scan, equivalent to an absorbed

dose of 0.27 eV/nm^3. When the beam power is slightly higher, 8.5 kV / 13 pA, a quasi-steady response is observed where the EBIC current remains almost unchanged from Scan 8 to 15 as seen in Figure Figure 2.9 C (a dose range of 0.16 to 0.30 eV/nm^3). On the other hand, the highest beam power (11.5 kV / 50 pA) tested results in almost 30% reduction of EBIC signal after the 3rd scan (Figure 2.9 D).

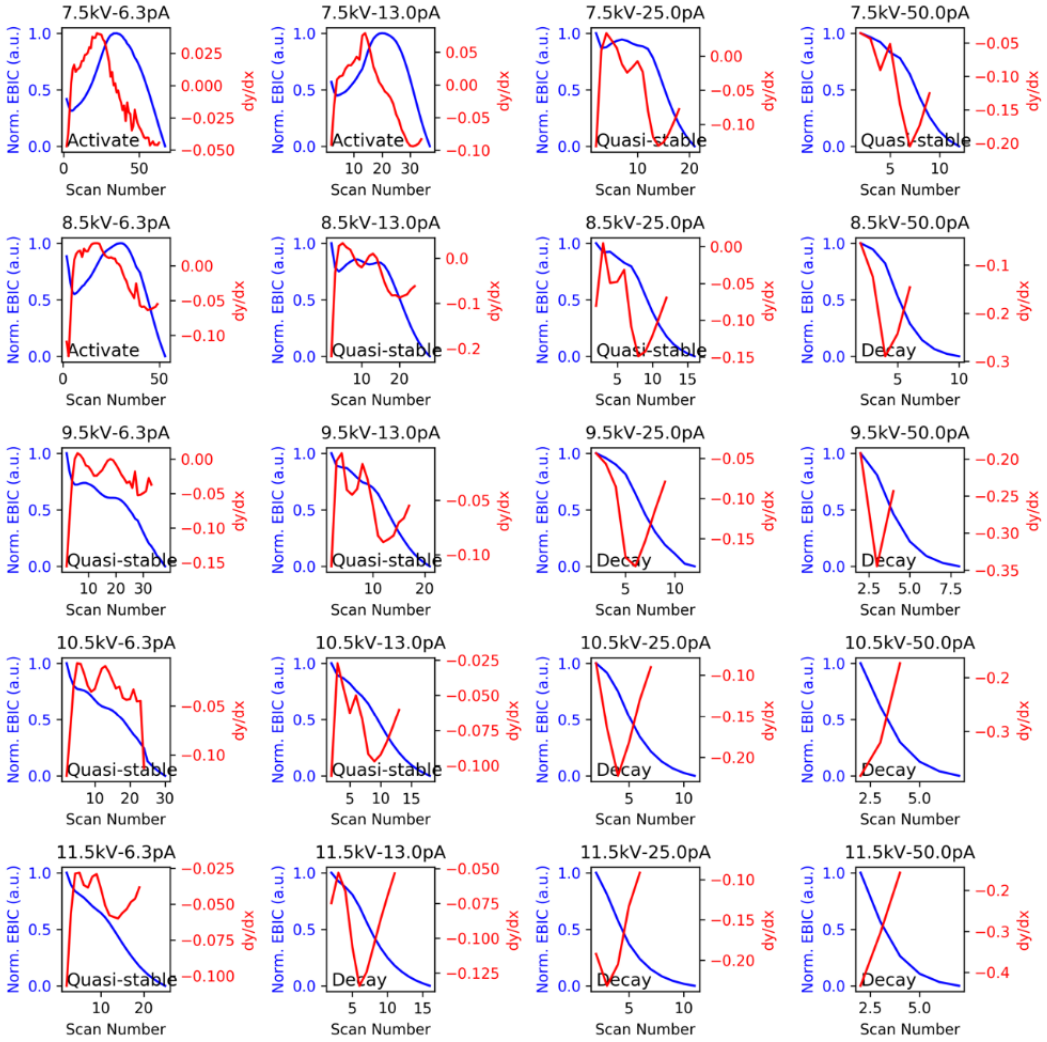

Figure 2.10. The EBIC response across the 20 different conditions of acceleration and voltages in this study.

The type of EBIC response observed does not appear to be strongly influenced by total accumulated energy dose (as shown in Figure 2.9), but it is strongly related to the power absorbed in the perovskite. A categorization of the characteristic type of EBIC response as a function of

beam current and beam voltage is provided in Figure 2.8, with contours indicating calculated lines of constant power absorbed in the perovskite in units of nW per point per scan. The categorization is extracted from the EBIC response at every beam condition, which is shown in Figure 2.10. Given that current varies by a factor of 5 but voltage by less than a factor of 2 across this parameter space, the characteristic EBIC response is evidently more sensitive to the e-beam voltage than the incident beam current. However, the type of EBIC response most closely follows the contours of power absorbed in the perovskite.

An activation response is seen when the power absorbed in the perovskite per point is less than 4 nW, decay EBIC profiles are mainly observed at beam energy above 20 nW, and quasi-steady responses can be found from 6-20 nW. Notably, activation and decay responses in literature reports of cross-section EBIC [79, 121] (as shown in Figure 2.12) also appear to follow these bounds – activation is seen when ¡6 nW is absorbed in the perovskite per point and decay is seen when ¿40 nW is absorbed per point. This correspondence when accounting for the power absorbed in the perovskite between cross-section experiments, where the perovskite is directly exposed to the beam, and the plan-view experiments here with overlying HTL and Au layers, suggest that the type of EBIC response is mainly a result of the beam-perovskite interaction.

2.3.3 Operating Regimes for Other Perovskite Devices

Leveraging on these learning, we perform similar study on perovskites with different absorber chemistry and architecture. Three other samples are explored with perovskite chemistry, methods of fabrication, device architecture and performance listed in Table 2.1. One-step (*1s*) and two-step (*2s*) are the two different deposition method utlized for sample preparation. Samples are denoted using the A-site composition followed by the deposition method and metal backcontact, in which CsFAMA-1s-Au was device used for collecting data present in Figure 2.9 and 2.11.

As perovskite composition can impact the absorber stability significantly, we extend the lower beam voltage limit to the extend possible to prevent rapid degradation of unstable perovskite even at 7.5 kV. While lowering the beam voltage for plan-view EBIC, it is crucial

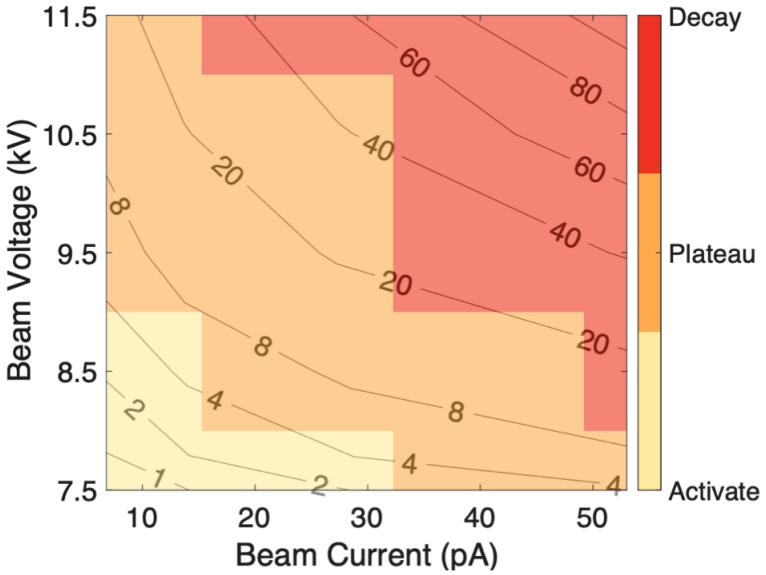

Figure 2.11. Categorical heat map of EBIC responses for beam current and voltage combinations: yellow red for "activation", orange for "quasi-steady", and red for "decay." The contour lines are lines of constant absorbed power in the perovskite in nW per point.

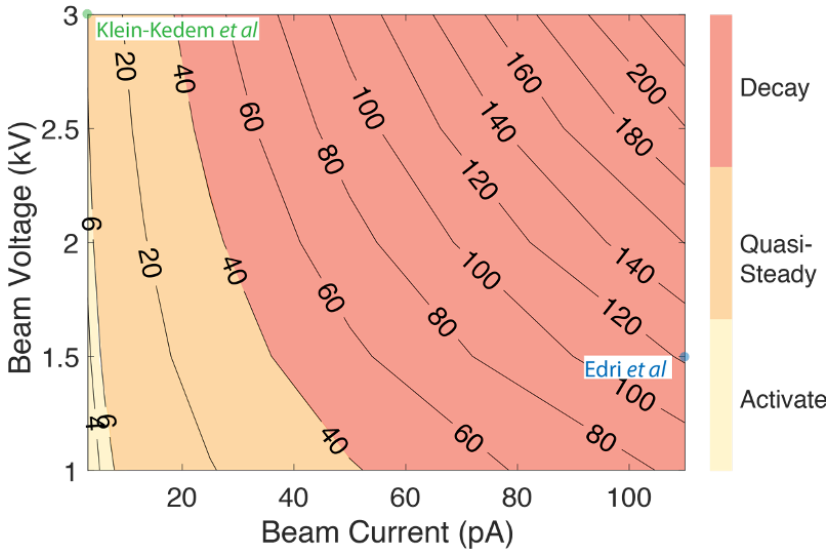

Figure 2.12. Absorbed power in the perovskite per point in cross-section EBIC. Contour lines are in nW from CASINO calculations. Also shown are the bounds for the activation, quasi-steady, and decay regimes seen in the plan-view experiments in this study. The experimental beam conditions used by Edri *et al.*[121] (1.5 kV/110 pA) and Klein-Kedem *et al.*[79] (3 kV/3 pA) are indicated and correspond to 6.7 and 120 nW/pt absorbed in the perovskite, respectively. Edri *et al*[121] saw rapid EBIC decay, while Klein-Kedem *et al.*[79] observed EBIC activation, in agreement with the bounds established in Figure 2.11.

Table 2.1. Sample information for EBIC measurement

Sample Name	FAMA-2s-Au	FAMA-2s-Ag	CsFAMA-2s-Au	CsFAMA-1s-Au
Deposition Method	2s	2s	2s	1s
Absorber Chemistry	$(FAPbI_3)_{0.9}$ $(MAPbBr_3)_{0.1}$	$(FAPbI_3)_{0.92}$ $(MAPbBr_3)_{0.08}$	$Cs_{0.05}(FAPbI_3)_{0.9}$ $(MAPbBr_3)_{0.1}$	$Cs_{0.05}(FAPbI_3)_{0.83}$ $(MAPbBr_3)_{0.17}$
Architecture	ITO/SnO_2/ PSK/Spiro/Au	ITO/SnO_2/ PSK/Spiro/Ag	ITO/SnO_2/ PSK/Spiro/Au	FTO/m-TiO_2/ PSK/Spiro/Au
PCE (%)	17.95	20.7	19.11	16.89

to consider the beam voltage effects on penetration depth as shown in Figure 2.7. With typical layer thickness of Au and HTL, the minimum beam voltage is simulated to be 6.5 kV to allow incident E-beam to penetrate through the overlaying layers fully shown in Figure 2.13. The EBIC responses for these samples are provided in Figure 2.14. As compared with device fabricated using *1s*, samples prepared using *2s* seem to be more sensitive to E-beam with decay regime shift towards lower beam power region. This beam sensitivity behavior also narrows the window for quasi-steady response (*i.e.* all *2s* samples). Even though the exact EBIC responses are slightly different between each other, the major trend still holds, in which high beam voltage and current combination degrades sample rapidly and lower beam power induces less damage on EBIC signal. Based on Figure 2.14, 6.5 kV / 6.3 pA can be used as the starting beam voltage and current combination for characterizing perovskites with typical 70 nm Au and 180 nm HTL layers.

2.3.4 Discussion and Conclusion

The variation of EBIC responses between samples with slight differences in composition illustrates the composition-dependent stability in halide perovskites. The shift of EBIC responses provides insights on the material stability upon interacting with high input energy from the e-beam. When comparing composition only, samples with the highest Br concentrations (CsFAMA-1s-Au) appear to be most stable devices under the e-beam among all the compositions. A similar

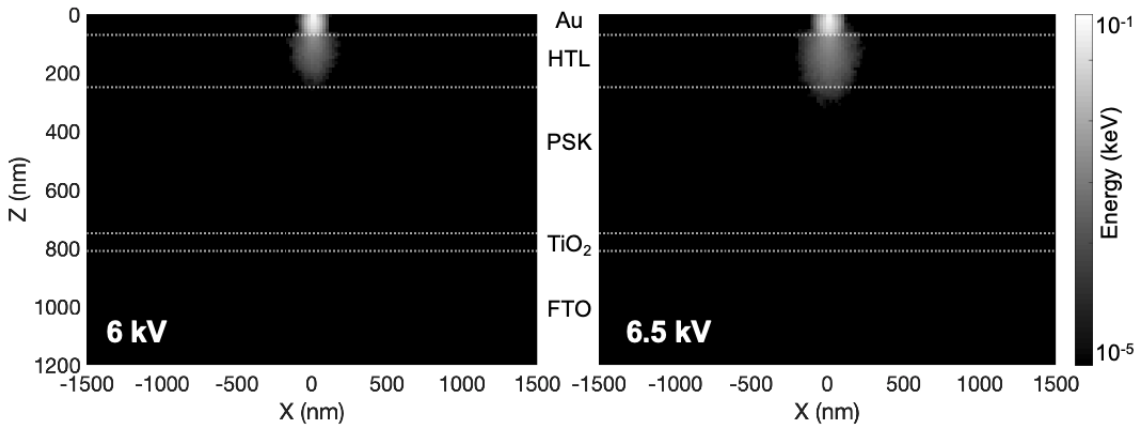

Figure 2.13. CASINO simulation of energy deposited in the device layers per incident electron at beam voltage of 6 kV (left) and 6.5 kV (right).

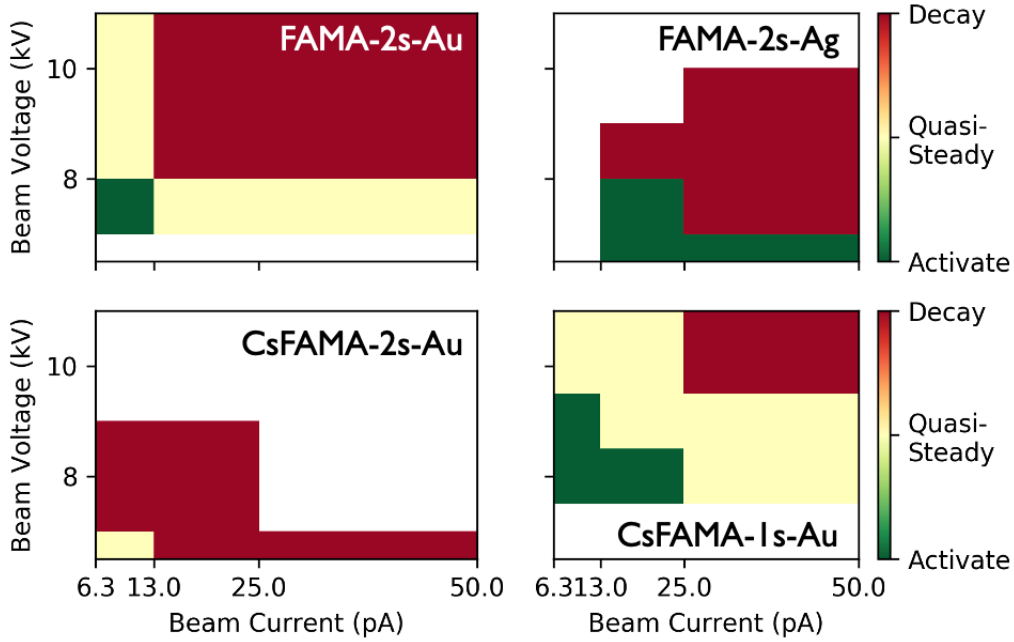

Figure 2.14. Categorical heat map of EBIC responses for samples with different composition.

trend is observed for samples that have the same deposition method (*i.e.* FAMA-2s-Au and FAMA-2s-Ag). These observations align with literature findings, in which devices that have over 1000 h stability under continuous illumination are composed of at least 0.33 mole of Br substituent in the mixed A-site and halide systems.[76, 135, 136] In addition to the Br concentration, the incorporation of Cs for stability enhancement should not be neglected as it strongly suppressed the photo-induced phase segregation in the mixed halide Br/I perovskite

absorber.[137, 74]

The EBIC data provide evidence that at least two distinct dose-dependent processes occur in the perovskite device during e-beam interaction. These processes are highly sensitive to the beam power reaching the perovskite, causing qualitative changes to the dose response, including the dominance of degradation processes at high power. The sensitivity to beam power may indicate that the rate of these processes depends on (1) the energy of the electrons incident on the perovskite layer, such as knock-on effects in the inelastic scattering process, and/or that it depends on (2) the power density, such as in local heating (which has previously been discussed).[79] The quasi-steady response appears to be the superposition (or at least interaction) of multiple photophysical processes occurring simultaneously. It perhaps indicates the competition between degradation and carrier induced brightening, or a self-repairing mechanism involving lattice expansion or lattice re-ordering.[131] While moving towards less stable compositions, the narrowing window of quasi-steady response suggests degradation dominates over other photophysical processes, as shown in Figure 2.14. As a result, the quasi-steady response will not be present if the halide perovskite is rapidly degraded under e-beam. For stable perovskites, on the other hand, the quasi-steady window provides an extended range of experimental conditions where EBIC or other electron microscopy can be conducted successfully without immediate degradation.

Some care must be taken in transferring the success of these operating beam current and voltage conditions to other microscopes and samples. In particular, the necessary voltages for the interaction volume to reach the absorber will be architecture-dependent. Determination of device layer thickness to support evaluation of the experimentally-desirable accelerating voltage using CASINO is encouraged prior to executing EBIC. I provide a user executable package for processing CASINO output files to help transfer this result to different perovskite solar cell architectures.[138] It is important to note that because the perovskite is more sensitive to electron acceleration voltage, it may be favorable to increase beam current to achieve sufficient EBIC signal-to-noise if necessary. With typical layer thickness of Au (70 nm) and HTL (180 nm),

we recommend starting plan-view EBIC measurement at 6.5 kV/ 6.3 pA to avoid rapid beam damage on the samples.

The activation, decay, and newly-observed quasi-steady responses indicate that multiple defect mechanisms are at play, demanding further investigation into the underlying defect chemistry. Having clearly-defined experimental conditions for successful E-beam characterization should facilitate correlative microscopy such as sub-band optical spectroscopy to pursue deeper understanding of the defects involved. EBIC can be part of a suite of tools for understanding the interplay of device-limiting defects in halide perovskites.

Plan-view EBIC can be seen as a promising – and even reliable – perovskite characterization approach to probe nanoscale current collection in operational perovskite devices, identifying defects and assessing device quality. Potential applications include exploring the underlying role of composition variations and passivants such as in quasi-2D perovskites [139, 66] or additives such as thiocyanate,[140] and to provide feedback for perovskite manufacturing scaling efforts, as is common in traditional semiconductor technology. Using the conclusions provided here, SEM-based characterization can be carried out with confidence of inducing little to no electronic degradation.

2.4 Chapter Conclusion

This chapter summarizes the rapid and efficient synchrotron based n-XRF technique for acquiring spatially resolved elemental distribution in nanoscale resolution. Implementing self absorption correction of the element-specific XRF signal is crucial during halide perovskite characterization. Unlike n-XRF elemental signal, electronic signal of XBIC and EBIC decays significantly under intense radiation. With the quantitative specification of probe voltage and current, electronic measurements (*i.e.* XBIC and EBIC) are performed with care to avoid sample degradation.

2.5 Acknowledgement

Chapter 2, in part, is a reprint of the material ”X-Ray Microscopy of Halide Perovskites: Techniques, Applications, and Prospects” as it appears in Advanced Energy Materials, Moses Kodur, Rishi E. Kumar, Yanqi Luo, Deniz N. Cakan, Xueying Li, Michael Stuckelberger, and David P. Fenning, 2020, 1903170, and an ongoing work of the material ”Quantitative Specifications to Avoid Degradation during E-beam and Induced Current Microscopy of Halide Perovskite Devices” for submission with authors of Yanqi Luo, Pritesh Parikh, Thomas M. Brenner, Juan-Pablo Correa-Baena, Tonio Buonassisi, Ying Shirley Meng, and David P. Fenning. The dissertation author contributed to the XRF, XBIC and EBIC portion of this material.

Chapter 3

Mixed Halide Perovskites: the Challenges and Difficulties

As introduced in Chapter 1.1, chemical flexibility of perovskite structure benefits the optical absorption and stability tunability in hybrid halide perovskite materials. The chemical complexity of absorber increases as the result of tuning A-, B-, and X- site compositions. Elements used during the tuning process can result in unforeseen beneficial or detrimental impacts. The main objective of this thesis work is to reveal and elucidate the roles of these tuning elements and their impact on local electronic performance. Synchrotron based X-ray microscopic techniques are chosen to perform rapid multi-modal microscopy within the dose limit before perovskite absorber degraded. Chapter 2 lays the ground work for conducting the measurement and analyzing the collected data. In this chapter, the halide stoichiometry and performance relation is revealed in the mixed halide perovskites. Upon adding Cl and Br into I-rich perovskites, Cl and Br are found to be heterogeneous distributed spatially in the films. Cl-rich aggregates do not appear to affect the local carrier collection but Br-rich clusters are efficient current collectors.

3.1 Spatially Heterogeneous Chlorine Distribution and the Electronic Impacts in Mixed Halide Perovskites

Spatial heterogeneities in the chemical makeup of thin film photovoltaic devices are pivotal in determining device efficiency. The presence of chlorine is positively identified, by means of n-XRF, in $CH_3NH_3PbI_3$ films synthesized with Cl-containing precursors and as an impurity in some films synthesized with nominally Cl-free precursors. The impurity may be introduced from precursors or as contaminants during film synthesis. The films formed from Cl-containing precursors contain roughly an order of magnitude higher amount of chlorine, with Cl:I values greater than 0.02 found whether Cl is present in either the organic or the inorganic precursor for both one- and two-step fabrication processes. A spatial variation in the Cl incorporation is observed within single particles and as well as between particles within a given film, and the standard deviation of the Cl:I ratio across the films is up to 30% of the aver-age value. Understanding and controlling the heterogeneous distribution of chlorine in hybrid perovskite layers may offer a path to improve their photovoltaic performance.

3.1.1 Introduction

Reports have shown that using chloride containing salts or precursors (methylammonium chloride, MACl, and/or $PbCl_2$) can assist perovskite crystal growth using one-step method, in which organic and inorganic halide salts are mixed in solution prior to deposition. This can be attributed to the small size chloride ions or the formation of $PbCl_2$ nanocrystals, which can act as a nucleation center [17, 141]. Additionally, the presence of MACl can also enhance the adsorption of lead iodide perovskite absorber on the TiO_2 substrate and produce large oriented crystallite domains by allowing slow crystal growth.[141, 142]

In perovskite solar cell synthesis, during the final annealing step the majority of the chlorine sublimes, resulting in a low degree of chlorine incorporation.[143] A number of reports with varying film preparations have failed to identify Cl incorporation with X-ray photoelectron

spectroscopy (XPS) or energy dispersive X-ray spectroscopy (EDS),[144, 145, 146] although bulk incorporation of chlorine as $CH_3NH_3PbI_{3-x}Cl_x$ with x<0.4 has been shown by bench-top X-ray fluorescence, synchrotron-based X-ray absorption spectroscopy and photothermal induced resonance (PTIR).[143, 147, 148, 149] X-ray absorption near-edge spectroscopy indicates that remnant Cl cannot be fully explained by the chemical state of Cl found in MACl and $PbCl_2$ precursors.[148] More typically, chlorine incorporation has been measured to be between 0.030<x<0.41 by XPS or EDS.[150]

Minor element incorporation in semiconductor absorbers typically leads to detrimental introduction of trap states in the bandgap,[151, 152] although at times it can be beneficial. For example, Na incorporation has been shown to provide beneficial passivation of grain boundaries in CIGS solar cells [153] and H is used to passivate structural defects in silicon solar cells.[154] Photoluminescence and EDS measurements have tentatively correlated chlorine with improved electronic performance, though its distribution in the film remains poorly quantified.[155]

In this study, we use synchrotron-based n-XRF microscopy to measure the na-noscale in-plane spatial distribution of chlorine in perovskite solar cells. By mapping the elemental distribution in nominally methylammonium lead iodide films with 100 nm spatial resolution, we find that chlorine is incorporated heterogeneously across the film, varying between individual particles. We quantify the variation in local incorporation of chlorine amongst different fabrication methods and find that it is largely independent of whether the Cl containing precursor is the organic or the inorganic component. All perovskite film stacks studied here are fabricated by standard conditions except no hole-transport layer is present.[156] Such a structure has been shown to produce a range of 10.8 to 12.8% efficiency [157, 158, 159] and allows a stronger XRF response to be measured through a largely-transparent Au back contact without the intervening hole-transport layer. The XRF nanoprobe provides insight into not only the local chemical stoichiometry of organometal halide but also the chemical distribution within this thin film system. The nanoprobe fluorescence data reveal a mi-croscopically heterogeneous distribution of chlorine and its manipulation by perovskite precursor chemistry, opening new directions toward

understanding how the distribution can be harnessed to optimize and stabilize hybrid perov-skite solar cells.

3.1.2 Materials and Methods

A series of solar cell thin film stacks was fabricated utilizing three different deposition methods: one-step (*1s*),[160] two-step (*2s*),[161] and spray deposition[162] with various ratios of methylammonium halide and inorganic precursors to produce perovskite absorbers on a mesoporous and a dense layer of TiO_2 substrate for both *1s* and *2s* method, and planar TiO_2 for spray deposition method (detailed compositions in Table 3.1). In the *1s* method, perovskite solution (40 wt% in DMF) was deposited onto the mesoporous TiO_2 by spin-coating at 2000 rpm, followed by an anneal at 90°C for 30 min. For the *2s* deposition method, PbI_2 was first spin-coated on mesoporous TiO_2 at 2000 rpm for 25 sec, allowed to stabilize for 3 min, then annealed at 70°C for 30 min. Second, this layer is dipped into methylammonium halide solution for 20s and then annealed at 90°C for 30 min to form the active perovskite absorber layer. These spin velocity, annealing temperature and time, dipping time, and precursor concentration parameters have been established as optimal for the hole transport layer-free solar cell architecture used here.[161] Spray deposition used the same perovskite solution concentration as the *1s* method but used DMF as the solvent. The solution was sprayed using a Paasche H-SET airbrush onto a planar TiO_2 substrate held at 80°C. The deposited layer was then annealed at 80°C for 40 min. The 40 nm Au back contact layer was evaporated over the perovskite layer under 5×10^{-6} torr.

Table 3.1 details the samples that were investigated, the ratios of their precursor chemistry, and their average chlorine incorporation as measured by n-XRF. The samples are grouped into two different categories, those with Cl-containing precursors and those with nominally Cl-free precursors.

Table 3.1. Effect of Precursor and Deposition Method on Cl Incorporation of Perovskite Samples

	Precursors
Precursors with Cl	PbI_2 + MACl:MAI (2:1,*2s*)
	PbI_2 + MACl:MAI (1:1,*1s*)
	$PbCl_2$ + MAI (*1s*)
Precursors without Cl	PbI_2 + MAI (*Spray*)
	PbI_2 + MAI (*1s*)

3.1.3 Chlorine Incorporation is Tuned by Chlorine Content of Precursors

Using the synchrotron based n-XRF, we are confident to identify the incorporation of Cl in the final perovskite films after annealing. A typical single-point XRF spectra is shown in Figure 3.1a indicating the detection of Pb, I and Cl in a PbI_2 + MACl:MAI film. Au from the semitransparent back contact, Ti from the underlying mesoporous TiO_2 and blocking layer, and Sn from the F:SnO_2 substrate are also detected. Figure 3.1b magnifies the shaded area indicated in Figure 3.1a. It compares the PbI_2 + MACl:MAI samples, made with Cl-containing precursors, to another sample made with Cl-free precursors and positively identifies the presence of chlorine in the sample made with Cl-containing precursors, indicated by the $Cl_{K\alpha}$ emission at 2.62 keV. While readily identifiable, the signal response of $Cl_{K\alpha}$ indicates only trace amounts of chlorine remain in the system.

Using chlorine-containing organic or inorganic precursors results in a significant chlorine incorporation into the hybrid perovskite films. Trace chlorine impurities are detected in some samples produced with nominally Cl-free precursors. Five different organic and inorganic precursor combinations and deposition methods listed in Table 3.1 are analyzed using n-XRF and shown in Figure 3.2. The XRF maps in Figure 3.2 are organized in descending order of average Cl:I mass ratio measured in the samples. The first three samples, containing the higher average Cl:I ratios, are the cells fabricated using either the Cl-containing organic halide MACl (row 1 and row 2) or the Cl-containing precursor $PbCl_2$ (row 3). Row 1 shows the XRF data for the

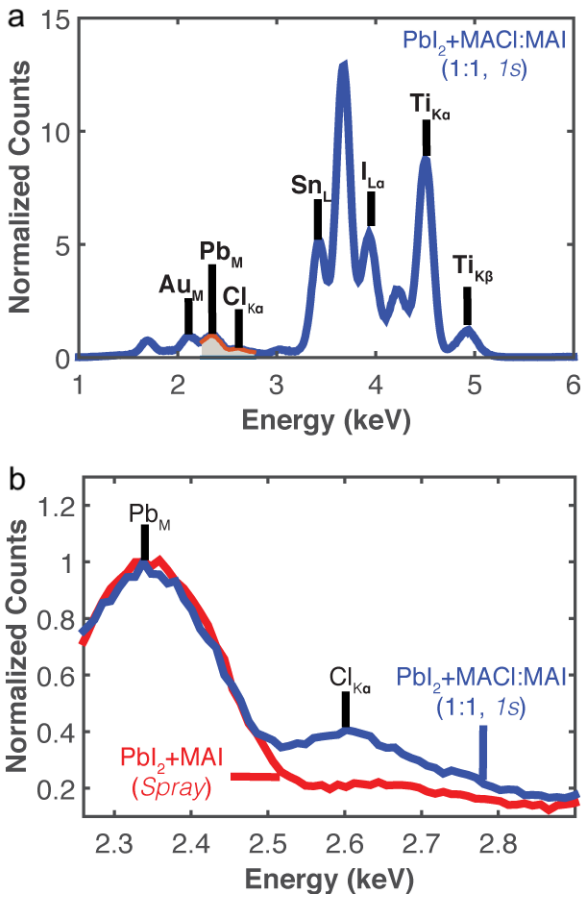

Figure 3.1. Identifying Cl incorporation in perovskite. (a) A typical single-point X-ray fluorescence spectrum revealing that, in addition to detecting all major elements in the film stack, Cl is positively identified (b) The normalized fluorescence spectrum in the 2260-2900 eV range (shaded area of (a)) containing the $Cl_{K\alpha}$ emission.

Cl-containing film synthesized by the two-step method with 2:1 MACl:MAI. Row 2 shows the data for a one-step film with 1:1 MACl:MAI. The two bottom rows show the nominally Cl-free samples synthesized with PbI_2 and MAI with different depositing methods *spray* (row 4) and *1s* (row 5). For a given sample, the Pb and I maps (Figure 3.2a and b, e and f, i and j, m and n, q and r) show similar spatial elemental distribution.

The Cl elemental distribution depends strongly on the film precursors. A normalized Cl XRF map and the quantitative Cl:I ratio are shown for each sample to support detailed comparisons between samples. All halide maps are scaled to their individual maximum for

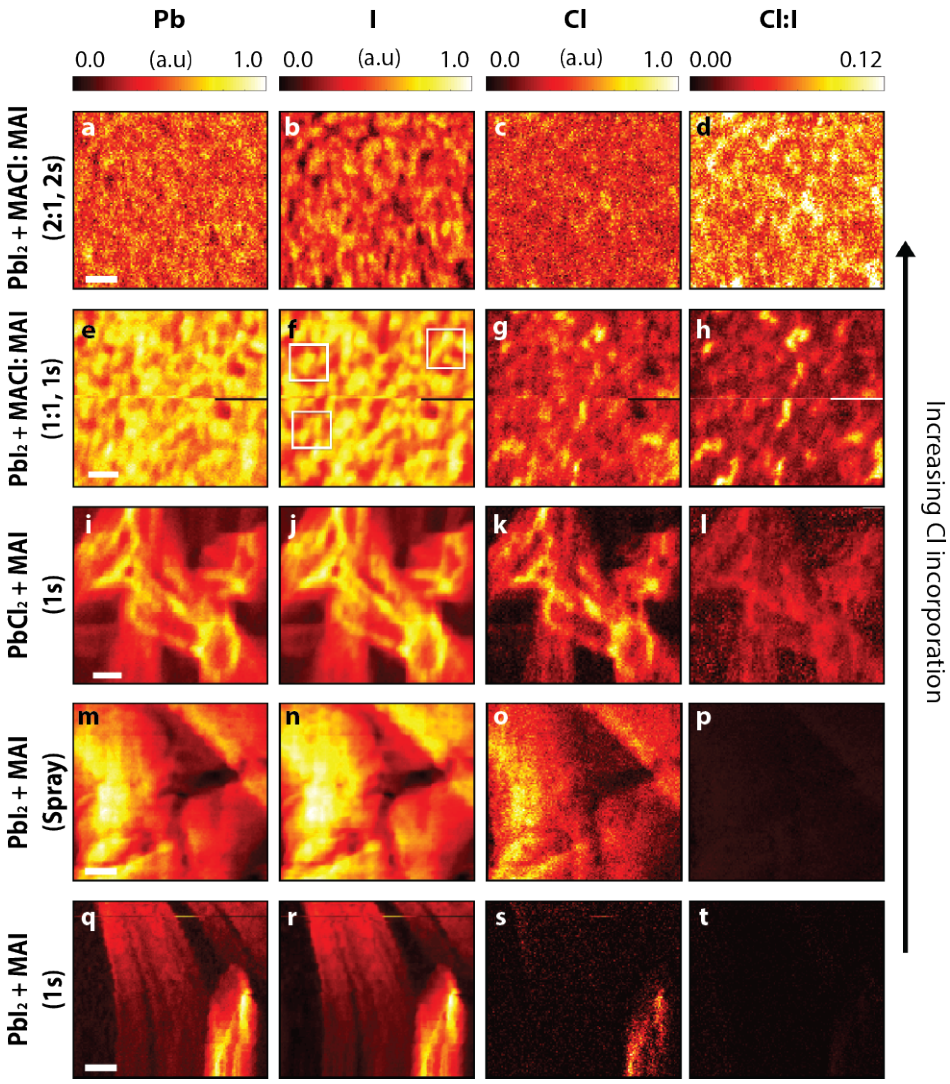

Figure 3.2. Lead, iodine, and chlorine and Cl:I mass ratio X-ray fluorescence maps (1 μm scale bars). Maps are corrected to account for incident beam and outgoing fluorescence attenuation through the multiple layers. XRF images are arranged in descending order of average Cl:I ratio response. The quantitative Cl:I mass ratio, defined at each point as the measured chlorine loading in μg/cm^2 over the iodine loading in μg/cm^2. Cl:I ratio maps are scaled identically from 0.00 to 0.12 for all samples.

comparison of the relative distributions across samples in Figure 3.2. The Cl spatial distribution has a similar pattern as lead and iodine in the Cl-containing precursor samples, but close comparison reveals the Cl distribution is distinct. The Cl:I ratio maps are all scaled identically from 0 to 0.12 Cl:I. The ratio maps not only provide a local chemical halide composition ratio

but show local variations in chlorine incorporation relative to iodine. The inhomogeneity of halide chemistry is clear in the ratio maps.

The Cl content of the resulting film can be directly manipulated by the amount of Cl-containing precursor used in synthesis. When chlorine is intentionally present in the precursors (Figure 3.2 rows 1-3), the sample's Cl XRF image is bright across the film, indicating local Cl content is high (Figure 3.2 c, g and k). The PbI_2 + MACl:MAI (2:1, *2s*) sample has the highest Cl-content in the precursors and subsequently the highest Cl:I ratio and the largest amount of chlorine rich areas (Figure 3.2 row 1). The Cl:I ratio map for the PbI_2 + MACl:MAI (1:1, *1s*) reveals slightly higher local Cl:I ratios than the $PbCl_2$+MAI and a greater variance as evidenced by larger contrast in the ratio map. Cl is incorporated whether it is present in the organic or the inorganic precursor.

The n-XRF data suggest that the degree of chlorine incorporation is dominated by the chlorine content of the precursors and that it is largely independent of whether chlorine-containing precursor is organic or inorganic component. While there may be some process dependence, for example the Cl:I ratio in the *2s* sample (Figure 3.2c) is slightly narrower in distribution than the *1s* preparations (Figure 3.2g and k), the Cl:I ratio maps offer a clear indication that Cl is generally incorporated in these films in a highly heterogeneous distribution.

3.1.4 Chlorine Heterogeneity within Single Particles

The measured variation in Cl:I ration within single particles can be as large as the variation across the film in FIgure 3.2. Figure 3.3 details three particles randomly selected and highlighted in Figure 3.2f. For each particle an approximate particle boundary is determined from the I XRF map and indicated across the I, Cl, and Cl:I XRF maps. In the Cl maps of Figure 3.3b, e and h, the inhomogeneous distribution of chlorine is revealed by readily visible chlorine-poor and -rich areas. The median halide ratio of the three regions are similar at 0.025, 0.024 and 0.030 respectively, but the Cl:I ratio within each particle varies by a factor of 4-6 and the corresponding Cl:I histogram on the right hand side of the figure indicates the overall distribution of the halide stoichiometry within the selected region. In particular, it is interesting to note that Cl rich regions are adjacent to the crystal region where Cl:I ratio is low.

The in-plane distribution indicates that Cl-rich areas appear adjacent to the boundary of some particles, perhaps indicating spatial segregation (Figure 3.2 i-l, Figure 3.3). The heterogeneous Cl incorporation observed here may lead to electrostatic effects at grain boundaries, such as: (1) wider bandgap $MAPbCl_3$ blocking layers that prevent minority carriers from reaching recombination sites at the grain boundary or perhaps (2) enhancing performance by acting as current-collecting channels as is the case of trace Cl in CdTe solar cells.[163] The nanoscale variations in Cl content that are directly observed here correspond to recent observation of local, nanoscale variations in bandgap in $CH_3NH_3PbI_{3-x}Cl_x$ films by Chae *et al.*[149] that were attributed to the heterogeneity of a Cl-doped perovskite phase. The spatial segregation of Cl seen may suggest a preferential heterojunction band alignment forms at grain boundaries, enhancing device performance by limiting recombination. Similarly, scanning Kelvin-probe force microscopy has found potential differences across grain boundaries relative to the grain interior, possibly due to PbI_2 phase segregation at grain boundaries.[164, 165] On the other hand, other Kelvin-probe force microscopy studies of grain boundaries in $CH_3NH_3I_{3-x}Cl_x$[121] films reveal insignificant potential variation across the bulk or at boundaries, suggesting that no

depletion region develops at these interfaces.

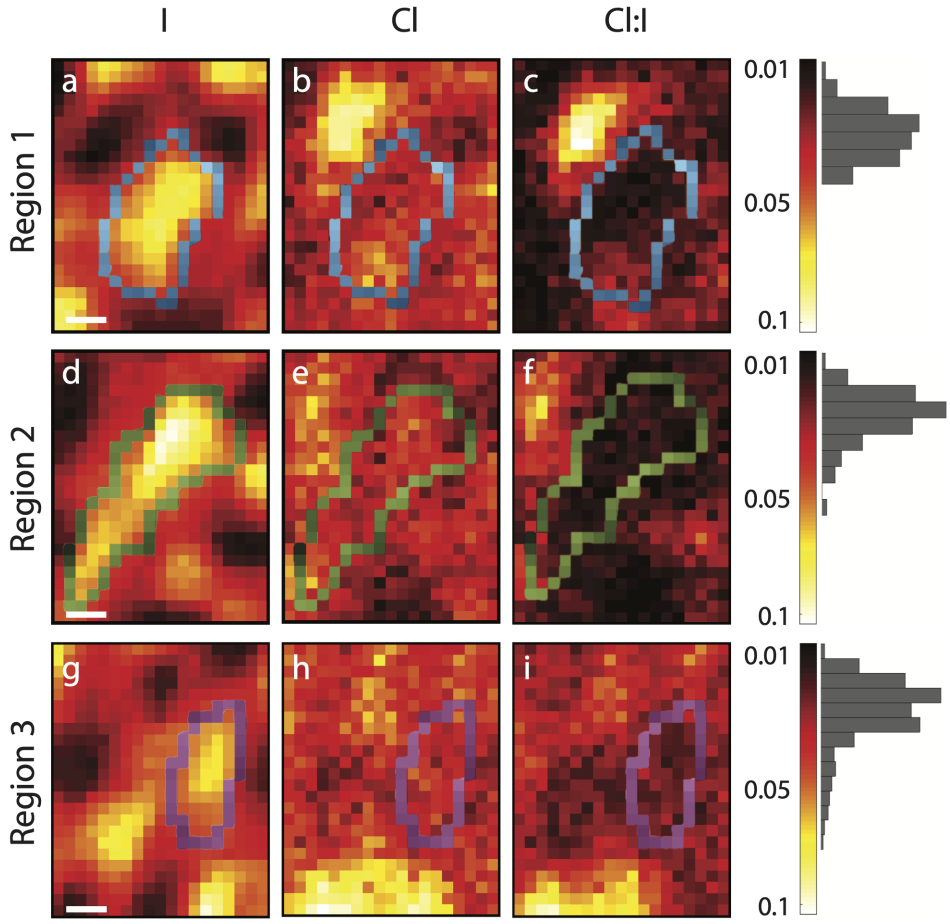

Figure 3.3. Three high-resolution images of regions of interest randomly selected from the Cl-containing PbI_2 + MACl:MAI (1:1, *1s*) sample. The highlighted boundary indicates the approximate outline of a single particle. The Cl:I map visualizes the varying chemical distribution. Within each boundary, the Cl:I ratio is computed with a summary histogram shown next to the Cl:I color bar. Scale bar is 100 nm.

3.1.5 Electronic Contribution of Chlorine Clusters

Building from the detection of a varying Cl distribution within perovskite films, it is crucial to gain clearer insight into its nanoscale electronic impacts. deQuilettes *et al.* explored the role of Cl in $MAPbI_{3-x}Cl_x$ film by correlating SEM/EDX and μ-PL mapping.[155] Brighter PL regions are detected where Cl content is high. However, the electronic role of Cl is still somewhat inconclusive. Other indirect effects due to presence of Cl, such as better crystal crystallinity,

cannot be entirely neglected. For example, first-principles calculations indicate that Cl may play a role in passivating defect states at grain boundaries.[45] As an alternative to looking at PL of band-to-band recombination at open-circuit,

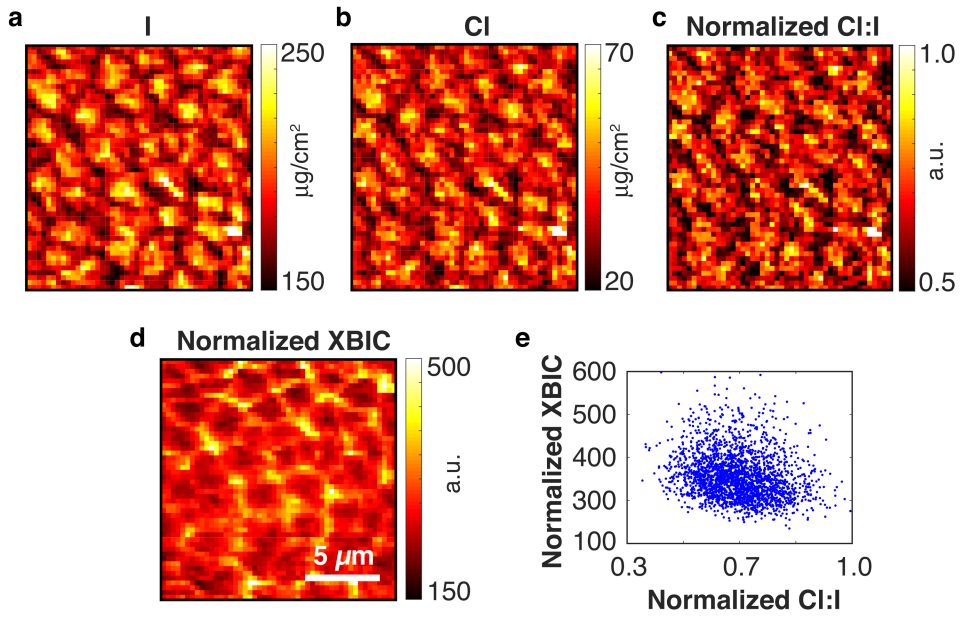

Figure 3.4. n-XRF/XBIC study of the optoelectronic role of Cl. (a-c) I, Cl, and normalized Cl:I n-XRF maps illustrate the varying halide distribution within $MAPbI_{3-x}Cl_x$ films over many grains. (d) Normalized XBIC mapping of the same film shows strong variations in nanoscale charge collection. (d) Scatter plot of normalized XBIC and Cl:I mass ratio reveals little relationship local Cl incorporation and charge collection, indicating that the spatial variation in current collection is not a direct result of the Cl distribution.

Here, we utilize n-XRF/XBIC to look at a $MAPbI_{3-x}Cl_x$ device under charge-extracting short-circuit conditions with result shown in Figure 3.4. A two-step deposition process was used to deposit perovskites on a mesoporous TiO_2 scaffold. The organic precursor solution had MAI:MACl = 2:1. The iodide map shows the individual grains and grain boundaries within the film, and the normalized Cl:I ratio map again indicates a highly heterogeneous distribution of Cl in the system (Figure 3.4a to c). The normalized XBIC appears to show enhanced charge collection in the thinnest part of the film near the grain boundaries Figure 3.4d. A plot of normalized XBIC vs. local Cl content is shown in Figure 3.4e. No correlation is found between

the relative enrichment of Cl content and current collection. It seems that the Cl does not play a direct role in either enhancing carrier collection or preventing it. Instead, the data support arguments that the overall improvement on device performance and longer carrier lifetime upon addition of Cl containing precursors are likely due to the indirect effect of improving crystal quality or enhancing surface/defect passivation.

3.2 Heterogeneous Distribution of Bromine and Its Impact on Local Charge Collection

As mentioned in Chapter 1.1, a small amount of Br incorporation benefits phase stability and optical absorption tunability. In this chapter, a nanoscale spatial variation of Br incorporation is found in both iodide rich and poor $FAPbI_{3-x}Br_x$ solar cells by n-XRF. Simultaneous collection of spatially-resolved X-ray beam induced current (XBIC) maps reveal large variations in local photocurrent collection. The application of these characterization techniques to the mixed-halide perovskites allows us to precisely superimpose the halide heterogeneity on the corresponding photocurrent response with resolution down to 200 nm. Combining the local elemental information from n-XRF and the local optoelectronic response from XBIC reveals the electronic role of Br substitution and Br-rich regions are shown to have efficient current collection.

3.2.1 Introduction

The benign role of Cl raises questions regarding the role of Br in the widely used mixed halide $MAPb(I_{1-x}Br_x)_3$ and $MA_{1-y}FA_yPb(I_{1-x}Br_x)_3$. Incorporating a small fraction of Br has shown to stabilize the black phase of $FAPbI_3$ in particular.[69] The $FAPbI_{3-x}Br_x$ composition range has been studied in detail by Eperon *et al.* and Rehman *et al.* investigating the band gap tunability, phase stability and charge carrier dynamics at various levels of Br incorporation.[10, 166] The band gap of the $FAPbI_{3-x}Br_x$ compositions can be tuned from 2.2 to 1.5 eV, with a shift from cubic to tetragonal phase as x varies from 0 to 1. An obstacle to homogeneous chemical mixing is the crystal structure difference between the tetragonal triiodide

and cubic tribromide FA lead perovskites, and only a small fraction of Br can coexist and be incorporated to produce a stable film in the FA-based perovskites.[10] Perovskite films with higher Br:I ratio exhibit a reduction in crystallinity and even amorphization along with X-ray diffraction (XRD) peak shifting and boarding, particularly for the (110) tetragonal peak.[10, 167] THz photoconductivity measurements at high Br incorporation (Br > 0.3) reveal that the regions of poor crystallinity that form due to the phase mismatch hinder charge-carrier transport with vanishing carrier mobility.[166]

Even in optimized 1:5 Br:I MAPb$(I_{0.2}Br_{0.8})_3$ perovskite films, abnormal optoelectronic behavior is observed including a reversible photo-induced trap formation in which the photoluminescence wavelength is red-shifted upon illumination[15, 168] and hysteresis during JV measurements where the forward and reverse biased conditions produce JV curves particularly in the triiodide perovskites.[169, 170] Multiple researchers have implicated ion migration[171, 172] in combination with charge collecting at low-bandgap iodide-rich regions[173] to explain the local bandgap shifting under illumination. The intrinsic heterogeneity in bromide-iodide nanoscale chemistry in mixed-cation films has been evidenced indirectly by Kelvin Probe force microscopy with nanoscale potential fluctuations that are thought to fundamentally limit solar cell performance.[174]

3.2.2 Spatial Distribution of Halides and Their Impacts on Charge Collection

Microscopic evidence of the nanoscale variations in chemistry and carrier collection underlying these important findings is provided by n-XRF/XBIC investigation of $FAPbI_{3-x}Br_x$. Figure 3.5 shows the nanoprobe XRF and XBIC maps for samples with different Br:I ratios (x = 0.25 and 0.75). The Br incorporation is highly varied as seen in the Br:(Br+I) ratio maps in Figure 3.5 a and b. The average Br:(Br+I) ratio and its standard deviation for the nominally $FAPbI_{2.75}Br_{0.25}$ and $FAPbI_{2.25}Br_{0.75}$ films are 0.08 ± 0.01 and 0.25 ± 0.04, respectively, indicating good agreement between the average measured composition and the targeted com-

position. Though the characteristic grain sizes are smaller in the x = 0.25 film than in the x = 0.75 film, a similar degree of Br segregation is observed in both films, as quantified by a coefficient of variation in Br:(Br+I) (standard deviation/average) of 0.17 for both $FAPbI_{2.75}Br_{0.25}$ and $FAPbI_{2.25}Br_{0.75}$.

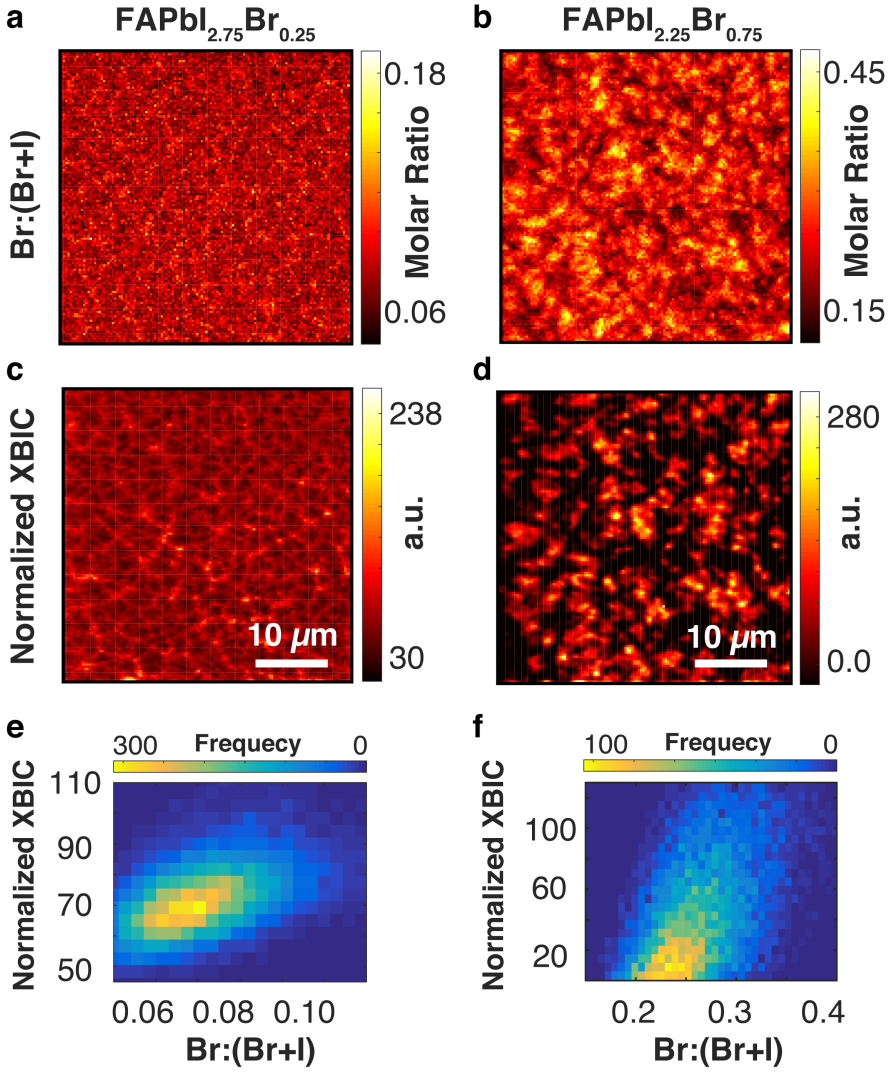

Figure 3.5. Halide distribution in $FAPbI_{3-x}Br_x$ and its impact on charge collection. (a,b) n-XRF maps showing the Br:Br+I ratio in films with x = 0.25 and 0.75. Heterogeneity increases with x but is seen in both films. (c,d) Normalized *operando* XBIC maps reveal highly non-uniform charge collection, with some locals areas exhibiting far better current collection than others. Large fractions of the x = 0.75 film show little photoresponse. (e,f) Two-dimensional histograms of normalized XBIC vs Br:(Br+I) ratio for x = 0.25 and 0.75 show a positive correlation between local Br enrichment and current collection probability.

The observed composition variation can potentially lead to the heterogeneous current collection in the FA based mixed Br/I devices. The normalized XBIC electronic map accentuates the evident phase segregation within the films. Especially in the higher Br content $FAPbI_{2.25}Br_{0.75}$, large non-collecting regions are observed in Figure 3.5 c and d. A two-dimensional histogram is used to illustrate the relation between Br incorporation and charge collection within each film as shown in Figure 3.5 e and f. In both cases, the regions within the film with higher Br content seems to yield better charge collection. This observation can be attributed to the band gap difference between $FAPbBr_3$ and $FAPbI_3$, in which the local regions of I-rich perovskite phase serve as sinks for generated carriers, with carriers generated in the Br-rich regions efficiently swept away and collected.[173] Although the Br-rich regions show improved charge collection, the tendency of mixed bromide iodide films to segregate on the nanoscale may limit the ability of these perovskites to reach their ultimate voltage limits due to bandgap-related Voc fluctuations.[174, 175]

Besides composition-performance relationship, the *operando* XRF/XBIC also provide evidence of composition determined phase stability in $FAPbI_{3-x}Br_x$ absorbers. As illustrated in Figure 3.5 c-d, larger photoinactive regions are seen in $FAPbI_{2.25}Br_{0.75}$ absorber than in $FAPbI_{2.75}Br_{0.25}$. The observed phase segregation agrees with both experimental findings that high Br concentration (Br$>$0.3) can result in poor crystallinity of due to phase mismatch between $FAPbI_3$ and $FAPbBr_3$.[10, 167]

3.3 Acknowledgement

Chapter 3, in full, is a reprint of the material "Spatially Heterogeneous Chlorine Incorporation in Organic-Inorganic Perovskite Solar Cells" as it appears in Chemistry of Materials, Yanqi Luo, Shany Gamliel, Sally Nijem, Sigalit Aharon, Martin Holt, Benjamin Stripe, Volker Rose, Mariana I. Bertoni, Lioz Etgar, and David P. Fenning, 2016, 28, 6536-6543, and a reprint of the material "The Relationship between Chemical Flexibility and Nanoscale Charge Collection in

Hybrid Halide Perovskites" as it appears in Advanced Functional Materials, Yanqi Luo, Sigalit Aharon, Michael Stuckelberger, Ernesto Magaña, Barry Lai, Mariana I. Bertoni, Lioz Etgar, and David P. Fenning, 2018, 28 (18), 1706995. The dissertation author was the primary investigator and author of this material.

Chapter 4

Mobile Bromine Ions: Direct Observation of Halide Migration and Its Effect on Photoluminescence

Challenge in homogenize mixing, phase mismatch, and chemical instability under operating conditions are the potential factors that attribute to the resulting phase segregation observed in both mixed Cl/I and Br/I perovskite absorber shown in Chapter 3. Eliminating the influence evolved from grain boundaries or heterogeneous halide mixing, we prepare a simpler material system, methylammonium lead bromide ($CH_3NH_3PbBr_3$) single crystal, to assist us understand the nature of halide stability. To investigate the instability and its consequences, we varied the electric field applied to single crystals and mapped changes in both their elemental composition and photoluminescence. Synchrotron-based n-XRF with 250 nm resolution revealed quasi-reversible field-assisted halide migration, with corresponding changes in photoluminescence. We observed that higher local bromide concentration was correlated to superior optoelectronic performance in $CH_3NH_3PbBr_3$. A lower limit on the electromigration rate is calculated from these experiments, and we interpret the motion as vacancy-mediated migration based on nudged elastic band density functional theory simulations. The XRF mapping data provides direct evidence of field-assisted ionic migration in a model hybrid perovskite thin single crystal, while the link with photoluminescence proves the halide stoichiometry plays a key role in the optoelectronic properties of the perovskite.

4.1 The Mobile Nature of Halides

Many groups have suspected ionic migration under an electric field and illumination as an important limiting mechanism in hybrid perovskite devices, particularly in regard to current-voltage sweep hysteresis.[49, 176, 170, 177, 169] Assuming thermal equilibrium and non-interacting defects, perovskites are predicted to have a high concentration of vacancies (10^{17}-10^{20} cm^{-3} for $CH_3NH_3PbI_3$).[178] Evidence of vacancy-mediated diffusion of X-site anions (in the ABX_3 structure) with low activation energy through the conventional hopping mechanism along the anion octahedral edge has been determined for oxide[22] and inorganic halide perovskites.[179] In the analogous hybrid halide perovskites, extensive computational investigations, particularly in the methylammonium lead iodide ($CH_3NH_3PbI_3$) system, have shown that I^- is likely the most mobile ion because it exhibits a lower energy barrier to migration in comparison to Pb^{2+} and $CH_3NH_3^+$.[49, 177, 171] Serval groups have observed ionic migration of both organic cations and halide anions and in $CH_3NH_3PbI_3$ and $CH_3NH_3PbI_{3-x}Cl_x$ using energy-dispersive x-ray spectroscopy (EDS),[176, 180] time-of-flight secondary-ion-mass spectrometry (tof-SIMS),[181] X-ray photoemission spectroscopy (XPS)[182] and IR microscopy mapping techniques.[181] These analytical techniques each have their own specific limitations. For instance, tof-SIMS involves sample fragmentation and physical destruction of the investigated area;[183] IR microscopy can detect bond stretches of the organic components in perovskite films but is generally not sensitive to the low-frequency vibrations of the inorganic components;[184] and XPS is sensitive only to the first few nanometers near the surface and requires high vacuum conditions. EDS must be applied with caution to halide perovskites because of their sensitivity to electron beam damage.[15, 79] Finally, the n-XRF technique maps heavy elements throughout the bulk of the sample with higher spatial resolution and sensitivity than XPS, tof-SIMS, EDX or IR microscopy.

The best way to provide a direct link between composition and performance is to combine spatially-resolved elemental or chemical detection methods with techniques that probe

the material's local optoelectronic properties. Luminescence spectroscopy and imaging are versatile techniques to probe recombination mechanisms and dynamics in semiconductors. For example, recently researchers have used spatially-resolved luminescence to reveal the role of Cl in $CH_3NH_3PbI_{3-x}Cl_x$,[155] to correlate contact resistance with morphology,[185, 186] and to understand the degradation of the perovskite layer[186] and its interfaces.[187] Despite the importance of ionic migration, open questions remain as to how stoichiometric changes affect photoluminescence – a property directly linked to device performance.[188, 189]

In this chapter, we identify a direct relationship between halide migration and local optoelectronic quality. Direct elemental evidence of halide migration in a $CH_3NH_3PbBr_3$ single crystal is detected using n-XRF. Thin single crystals[190] of $CH_3NH_3PbBr_3$, which are tens of microns wide and $\sim$ 500 nm thick, are used as a model system to study the fundamental properties of ionic migration in hybrid perovskites, avoiding complications from grain boundaries that are present in perovskite thin films. In response to an applied electric field, local stoichiometric variations appear along the crystal, which are correlated to local changes in the PL intensity. PL intensity increases in halide-rich regions and decreases in halide-poor ones, with quasi-reversible variation observed over multiple voltage biasing cycles. Furthermore, nudged elastic band (NEB) density functional theory (DFT) computations confirm that Br- ions experience a low energy barrier to migration within the $CH_3NHP_3bBr_3$ structure. The direct link between local stoichiometry and optoelectronic quality also clarifies that halide migration is a challenge that is intrinsic to the absorber and one that may play a determining role in the ultimate performance limits of perovskite devices.

4.2 Materials and Methods

Nano-XRF mapping is used to identify the spatial distribution of elements within a $CH_3NH_3Pb_3Br_3$ single crystal under applied bias. The crystals span Pt electrodes, and the voltage is applied laterally across the device as shown in Figure 4.1. Pt electrodes prevent any

driving force from a difference in the work functions of two different metals and also minimize chemical reactions or diffusion[53] of metallic atoms at the metal/perovskite interface.[191] Prior to the XRF measurement, electrical contact between the perovskite crystal and Pt electrodes was confirmed by current-voltage (I-V) scans and evaluate the semiconducting nature of lead halide perovskite in both light and dark conditions (Figure 4.2). Fluorescence spectra were collected at each point during the XRF mapping using a synchrotron X-ray beam with a 250 nm full-width half maximum. Figure 4.3a shows the corresponding optical micrograph of the $CH_3NH_3PbBr_3$ crystal studied by XRF. Note that the light elements in the methylammonium cation are not detectable by XRF, but the major heavy elements Pb and Br are detectable with sensitivity down to parts per million.

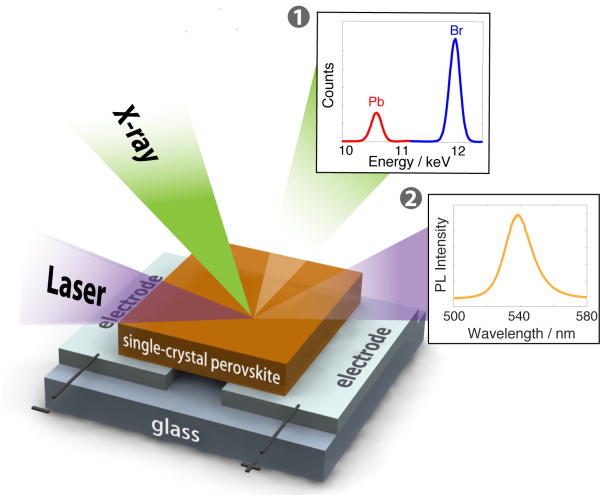

Figure 4.1. Photon-in Photon-Out Correlative Microscopy: schematic of nanoprobe X-ray fluorescence and spatially-resolved photoluminescence (PL) measurement. A 250 nm X-ray beam excites elemental fluorescence that reveals the local perovskite stoichiometry in single crystals bridging Pt-Pt electrodes. Subsequently, a laser beam excites optical luminescence to elucidate local optoelectronic quality. Note XRF and PL were not performed at the same time, but sequentially in a correlative microscopy approach.

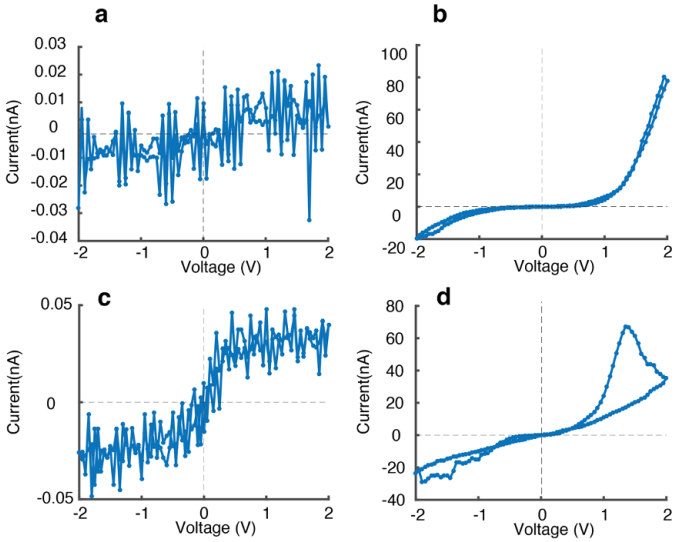

Figure 4.2. The electrical contact and photoresponse of $MAPbBr_3$ crystals on Pt-Pt electrodes were ensured before XRF and PL experiments. Current-voltage curves of $MAPbBr_3$ crystal before X-ray (for XRF) exposure under (a) dark condition, (b) AM1.5G illumination, crystal before laser (for PL) exposure under (c) dark condition and (b) AM1.5G illumination show clearly the crystals were electrically contacted to the electrodes and their current enhances by light illumination.[54]

4.3 Observing Br Migration upon Bias via n-XRF Mapping

The local Br:Pb stoichiometry within the $CH_3NH_3PbBr_3$ single crystal is initially homogeneous across the crystal but changes systematically during application of an external electric field (Figure 4.3). The seven XRF maps of the Br:Pb atomic ratio in the 30 x 30 μm^2 crystal are arranged from left (Map 1) to right (Map 7) based on the chronological sequence of applied bias. Map 1 is the initial scan showing the Br:Pb atomic ratio. As expected, the initial area-averaged Br:Pb ratio across the crystal was 3.08 +/- 0.2. An arrow above each XRF map measured under bias indicates the direction of the electric field, where the left electrode is held at ground and the right electrode has the applied voltage bias V_{app} (orange arrow: V_{app} = -2V and blue arrow: V_{app} = +2V). The Br:Pb ratio is plotted because it removes the effects of small spatial variations in thickness, but the shift in Br:Pb ratio seen in Figure 4.3b results entirely from a change in the Br distribution, as the Pb distribution remains constant throughout the XRF mapping (not

shown).

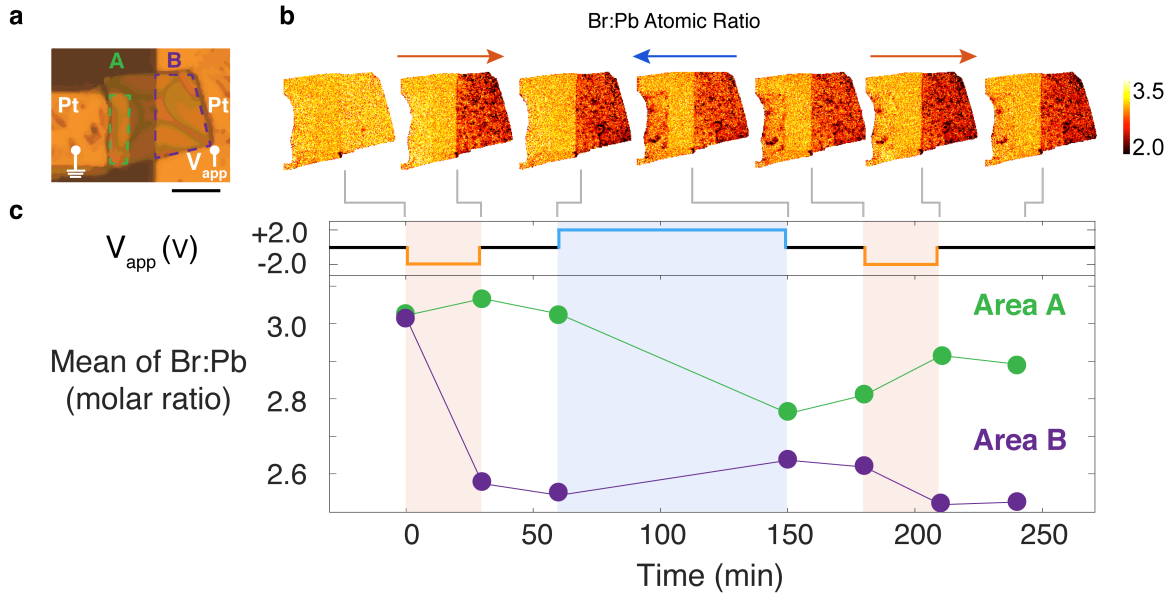

Figure 4.3. n-XRF measurement of the changes in elemental distribution in a $CH_3NH_3PbBr_3$ single crystal under bias. (a) An optical image of the $CH_3NH_3PbBr_3$ crystal characterized by n-XRF. Regions A and B where the crystal covers the two different electrodes are indicated. The electrode under region A is grounded and the other electrode is biased. Scale bar is 15 μm. (b) X-ray fluorescence maps of the Br:Pb elemental ratio with 250 nm step size and 100 ms dwell time per point under a sequence of +/- 2V biases. The direction of the corresponding electric field for each map under bias is denoted by an arrow above the map (-2V orange and +2V blue). (c) The mean Br:Pb ratio of Area A and Area B (*cf.* Figure 4.3a) as measured by X-ray fluorescence during the bias sequence with the corresponding bias condition (top). Time spent at -2V is shaded in orange and +2V in blue.

To examine the migration in detail, the perovskite crystal underwent a total of three poling cycles, from unbiased to +/- 2V bias to unbiased. After collecting the initial unbiased map (left of Figure 4.3b), a -2V DC bias was applied. After 30 minutes of bias applied without X-ray irradiation, we collected an XRF map (25 min duration) with the bias still applied to observe the effect of the electric field. The change in the Br:Pb atomic ratio between Maps 1 and 2 clearly indicates depletion of Br above the electrode at lower potential (right Pt pad). This depletion is consistent with the direction that Br^- anions would migrate. The bias was then removed, and after a 30 min relaxation period, a third XRF map was taken to visualize any diffusion along

the Br concentration gradient. The Br concentration is then slightly depleted over the left-hand electrode as Br^- diffuses back in the absence of bias.

When the direction of the bias is reversed (+2V), the Br shifts toward the positively biased electrode, also consistent with migration of Br^- anions. A significant Br shift away from the left-hand negative electrode is observed in Map 4, while the Br concentration recovers slightly on the right-hand electrode (Map 2 vs 4). Upon subsequent relaxation in Map 5, a small recovery in the Br distribution is again seen. The last cycle seen in Maps 6 and 7 repeats the same -2V and 0V bias condition as Maps 1 and 2, respectively, and confirms that the observed changes in the Br:Pb distribution are repeatable. Given the observed migration across the 10 μm electrode gap within 30 min at a 2V bias, the lower bound estimate of Br mobility at room temperature is 2.78×10^{-10} $cm^2/(V \cdot s)$ (see Chapter 4.7 for details).

To assess the migration of Br^- within the crystal more quantitatively, the changes in average Br:Pb atomic ratio above each of the two electrodes are presented in Figure 4.3c. The average ratio is plotted with respect to time and applied bias. As Br:Pb increases on one electrode, a decreasing ratio is seen on the other, providing additional support for an ion migration mechanism. The largest Br concentration change occurs above the lower potential electrode (Electrode B) right after the first bias is applied, when the Br:Pb ratio drops from 3.0 ± 0.03 to 2.6 ± 0.07. All subsequent changes are smaller, and the Electrode B area never recovers fully to its initial Br concentration. On the other hand, Electrode A exhibits a more reversible response to applied bias and largely recovers from the smallest Br:Pb ratio near 2.8 ± 0.09 to 2.9 ± 0.06 after final relaxation. Small, severely Br-deficient regions evidenced by localized dark spots in Figure 4.3b develop above both electrodes over time. These regions indicating local degradation of the perovskite phase and possible formation of $PbBr_2$. After biasing the crystal for 4 hours, the area-averaged Br:Pb ratio in the last XRF map (rightmost) is 2.69. The loss of Br occurs predominantly during the first negative bias of each electrode, after which the total average concentration of Br was fairly stable (Figure 4.4). Given what appears to be nanoscopic local formation of $PbBr_2$ in some regions, one could speculate that trace amounts of MABr leaves

the sample in an electrochemical reaction in regions of negative bias under X-ray irradiation, or the gradual formation of gas phase methyl bromide (CH_3Br) and ammonia (NH_3).[192] On the other hand, little change of the Br:Pb ratio away from 3.0 is observed between the electrode gap throughout the biasing cycles. Overall, the Br:Pb distribution shifts in the direction opposite the applied field at all time points.

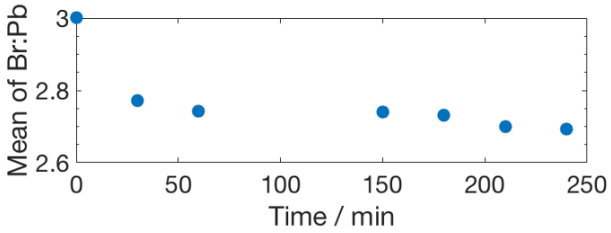

Figure 4.4. Average Br:Pb ratio with respect to time over the entire crystal as measured by n-XRF in Figure 4.3.

4.4 Impact of Br Migration on Optoelectronic Properties

A fresh $CH_3NH_3PbBr_3$ microcrystal, (optical image shown in Figure 4.5a, I-V scan in Figure 4.2), from the same sample chip is used to explore how the local optoelectronic properties vary in response to a similar bias sequence used in the n-XRF experiments.The photoluminescence (PL) data presented in the rest of the chapter was collected by Dr. Parisa Khoram, one of the co-authors of this work. The crystal was excited using a 15 μW, 405 nm continuous-wave violet laser while performing PL mapping before, during, and after bias. PL spectra were collected for each point of the crystal by moving the stage in the X and Y directions by 333 nm steps. PL maps were constructed from the integration of the total emission intensity over the wavelength 500-580 nm. Enhancement of PL intensity under bias at the forward biased electrode and its reduction at the reverse biased electrode is attributed to the change of the depletion region width at each contact. Similar changes in PL emission intensity with the variation of DC bias were reported in other semiconductors such as InP, GaAs and chalcopyrite ($CuGaSe_2$).[193, 194, 195]. To compare crystals at the same bias condition, the PL emission

spectra averaged over the area of each electrode (area A and B) were collected at zero bias after applying and removing the electric field as shown in Figure 4.5b-c. An increase in PL intensity relative to its initial value was observed in the region above the electrode previously held at higher potential. A decrease was observed over the contact at lower potential. According to the XRF maps in Figure 4.3, the contact with the higher potential is where the Br concentration is higher; therefore, the Br^- rich regions exhibit enhanced PL after removal of the electric field.

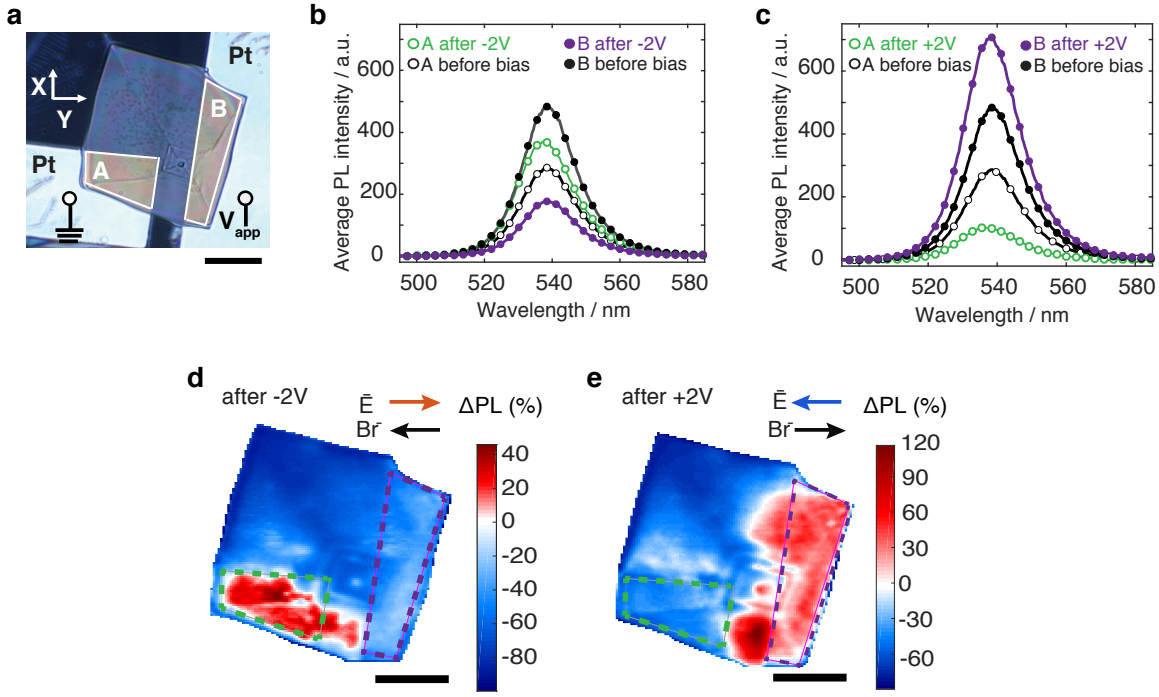

Figure 4.5. Photoluminescence variation of $CH_3NH_3PbBr_3$ after cyclic biasing. (a) Optical image of a hybrid perovskite crystal on Pt electrodes with labeled regions of interest A and B. (b) and(c) Overlaid photoluminescence spectra in Areas A and B after -2V and after +2V biasing, respectively. Black curves in each figure represent the initial PL intensity before any biasing in areas A and B. Plots with empty and filled markers correspond to average PL spectra of areas A and B, respectively. The corresponding spatially-resolved relative PL intensity maps are shown in (d) for -2V bias and (e) for 2V bias relative to the initial unbiased PL map. Scale bar is 10 μm.[54]

Figures 4.5d-e show the spatial variation of PL intensity across the crystal in response to biasing as the percentage change of PL intensity (ΔPL%). Each map represents the percentage

change of PL after removing the electric field and returning the crystal to the initial 0 V condition. (Details of the calculation are in Chapter 4.7.) The orange and blue arrows on figures 4.5 d and e, respectively, show the electric field that the crystal experienced before collecting the PL maps. Comparing the relative changes with the direction of the electric field, one sees that the PL intensity increases in the region that experienced higher potential (see the red regions at left side Figure 4.5d and right side Figure 4.5e), and decreases in the region that was previously at lower potential (see the blue regions at right side Figure 4.5d and left side Figure 4.5e). This anti-correlation between Electrodes A and B after bias mirrors the trend seen in XRF. The bias-dependence of the local photoluminescence is confirmed in $CH_3NH_3PbBr_3$ crystals deposited onto different electrodes (Au-Au and Au-Ti electrodes) as shown in Figure 4.6, indicating that the increase of PL in the opposite direction of electric field is independent of the particular metal/perovskite interface. In all cases, the peak of the PL spectrum does not shift in energy significantly (less than 2 nm) between the Br-rich and Br-poor regions (see Figure 4.7).

The PL mapping experiment was also done on the crystal that was exposed to the X-ray beam during XRF mapping, and its the PL spectra were comparable to those of a fresh crystal (Figure 4.7 k and l) with the PL peak being blue shifted by 10 nm. A similar trend in PL intensity shift with electrical biasing is seen for this crystal, although the change in PL intensity is not as clear as it is for the fresh crystals (Figure 4.8 b and c). Synchrotron X-ray irradiation has been shown to degrade carrier collection in hybrid perovskites within seconds of exposure at a single spot,[196] and it is thus not surprising that the PL changes are more clear in the fresh crystal.

The changes in PL intensity may be explained by vacancy-mediated halide migration. Initially, the PL intensity was inhomogeneous across the single crystal suggesting that surface or bulk defects dominate the PL response. Upon applying bias across the crystal, it is observed that Br moves opposite to the direction of the electric field and the local PL increases where Br increases. This enhanced PL in bromide-rich regions may originate from three distinct but related mechanisms, triggered by the ionic migration seen in the XRF maps (schematic of mechanisms in Figure 4.9). First, bromide migration will lead to local changes in the bromide vacancy

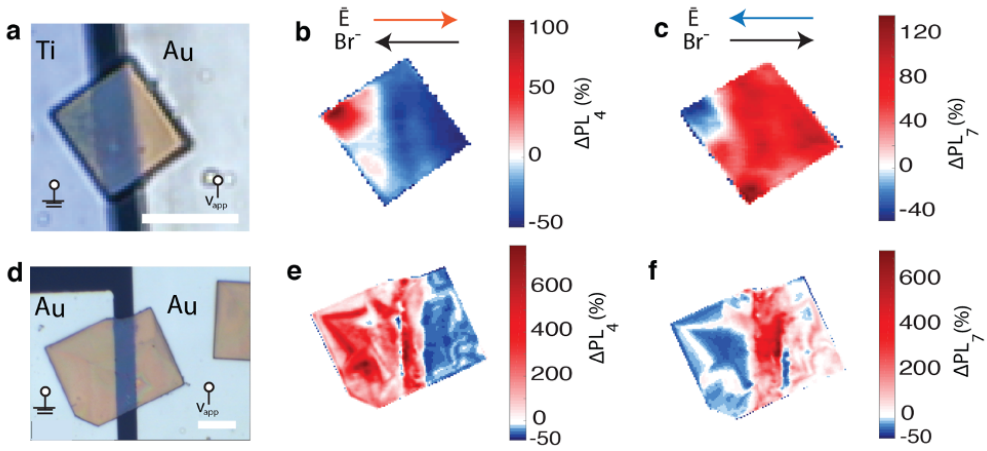

Figure 4.6. Series of relative PL maps for $CH_3NH_3PbBr_3$ crystal on Au-Ti (a-c) or Au-Au electrodes (d-f). The trend of an increase in PL intensity in the opposite direction of electric field is independent of electrode material. a) optical image of the crystal sitting on the gap between Au-Ti electrodes. b) relative PL intensity map of the crystal after applying -2V bias. c) relative PL intensity map of the crystal after applying +2V bias. d) optical image of the crystal sitting on the gap between Au-Ti electrodes. e) relative PL intensity map of the crystal after applying -2V bias. f) relative PL intensity map of the crystal after applying +2V bias. The arrows on top of each column show the direction of electric field and expected direction of Br- movement. Scale bar is 10 μm.[54]

concentration, which has been proposed to play an important role in the photoluminescence quantum yield.[197, 198]. Crystal point defects such as vacancies may act as non-radiative recombination centers; therefore, a higher Br vacancy concentration could lead to lower radiative recombination efficiency, causing the band-to-band PL intensity to decrease. Second, bromine stoichiometry may play a role in the density of interface states at the contacts. The migration of the bromine away from the contact interface at the lower potential electrode may lead to a higher density of interface states, and at the other contact, the higher Br content may passivate interface states. Finally, ionic migration will cause some residual change in the potential at the perovskite/metal contact interface even after the electric field is removed, due to slow ionic diffusion. At the lower-potential contact the perovskite/metal interface behaves as in reverse bias: the residual change in potential increases the depletion region, which helps to split the photogenerated carriers and prevents them from recombining radiatively, suppressing PL intensity.

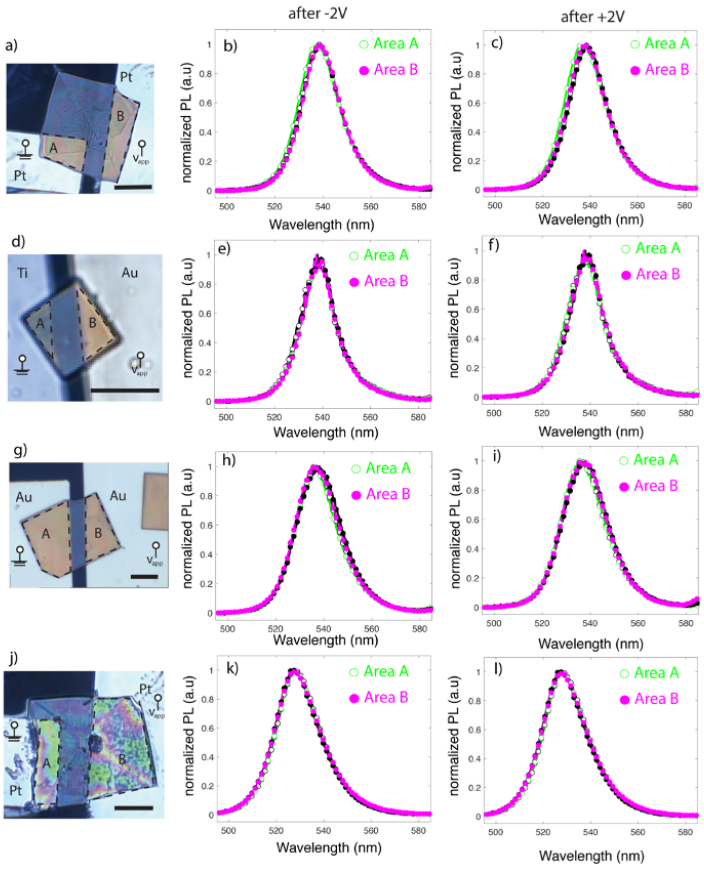

Figure 4.7. Normalized PL spectra of $CH_3NH_3PbBr_3$ crystals with different electrodes shows that the energy of PL peak does not vary upon applying electric field. The first column shows the optical image of the tested crystals on different electrode materials. Areas A and B are shown with dashed line on each figure. Second column presents normalized PL spectra after -2V poling for selected regions A and B. Third column shows normalized PL spectra after +2V poling for selected regions A and B. Scale bar is 10 μm.[54]

At the higher-potential contact the interface behaves as in forward bias: the depletion region becomes smaller and PL intensity is enhanced. Further studies are necessary to quantify the relative importance of each mechanism. Self-trapped carriers in the crystal lattice (strong-coupled polarons) have been suggested to play a role in charge carrier dynamics of hybrid perovskites and affect radiative recombination rate.[199] In the case of polaron formation, a red shift in the energy of the PL peak is expected, but no red shift was resolved within the detection limit of the PL setup in this study (SI, Figure 4.7). Continued detailed study of ionic migration is critical

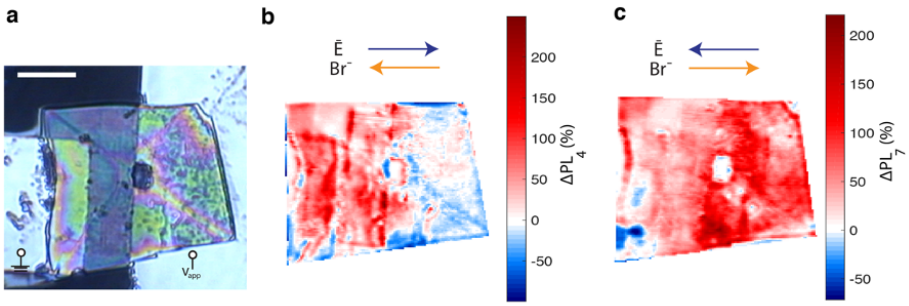

Figure 4.8. Percentage changes of PL intensity of the of $CH_3NH_3PbBr_3$ crystal after XRF measurement. (a) optical image of the crystal. (b) and (c) are relative PL maps after -2V and +2V poling respectively.[54]

because vacancies, as inherent material defects, may act as mediator or direct participants in non-radiative recombination centers in $CH_3NH_3PbBr_3$.

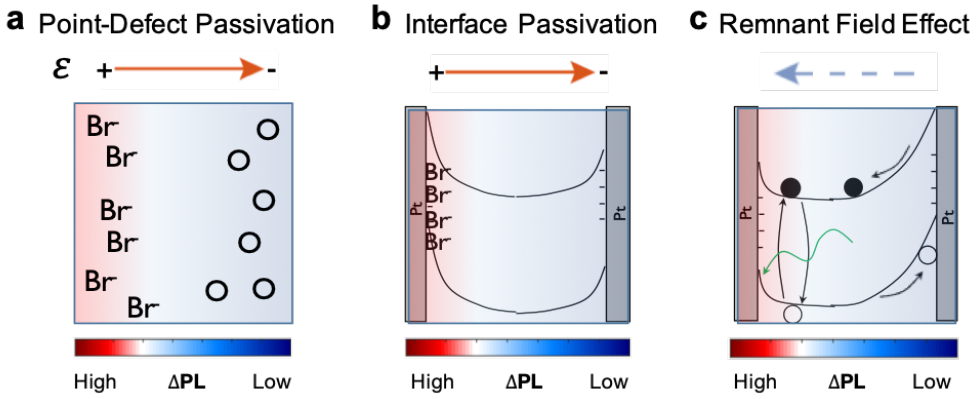

Figure 4.9. Schematic of mechanisms that can explain the observed PL intensity variation. At the positive (negative) electrode, Br migration may (a) reduce (increase) a vacancy-related, recombination active point-defect concentration, or (b) passivate (expose) surface states at the contact interface. Alternatively, (c) the remnant field due to slow ionic back-diffusion after the electric field is removed may leave a narrower (wider) depletion region.

4.5 Halide Migration Barrier Estimated by Density Functional Theory (DFT)

By collaborating with Dr. Zhuoying Zhu, the experimentally observed changes in Br concentration in the $CH_3NH_3PbBr_3$ single crystal are substantiated by the low energetic barrier to migration of Br^- found by DFT climbing-image nudged elastic band (CI-NEB) calculations. To elucidate the ionic migration mechanism under applied bias, CI-NEB calculations were performed using $2 \times 2 \times 2$ supercells (computational details in Chapter 4.7). CI-NEB is a common method for finding minimum energy paths for ion migration.[200, 201, 202] A single positively-charged Br^- vacancy (V_{Br^+}) was introduced, and overall charge neutrality was achieved via a compensating background charge. We find that the lowest energy configuration for pristine $CH_3NH_3PbBr_3$ is in which the polar methylammonium (MA) cations are aligned, which is the expected orientation under an applied bias.[177, 180] This alignment of the MA cations breaks the cubic symmetry, resulting in three distinct migration paths for Br^-, which are shown in Figure 4.10. The hops where the Br^- moves with a component in the direction of the C-N bond alignment, denoted as BCB and BAB, show the lowest migration energy barriers of 227 meV and 306 meV, respectively. The other hop, CAC, shows a migration energy of 425 meV. The alignment of the MA cations under bias appears to create a channel with a lower energy of Br^- vacancy migration along the field direction. In the absence of an electric field, this lowered barrier will be averaged out as methylammonium molecules are randomly oriented at room temperature per $MAPbBr_3$ single crystal neutron diffractometry.[203] Halide migration appears to benefit from MA alignment that results in a lower migration energy barrier under an applied bias. The migration, in turn, is correlated with the density of recombination active defects as evidenced by the changes seen in the photoluminescence response under bias.

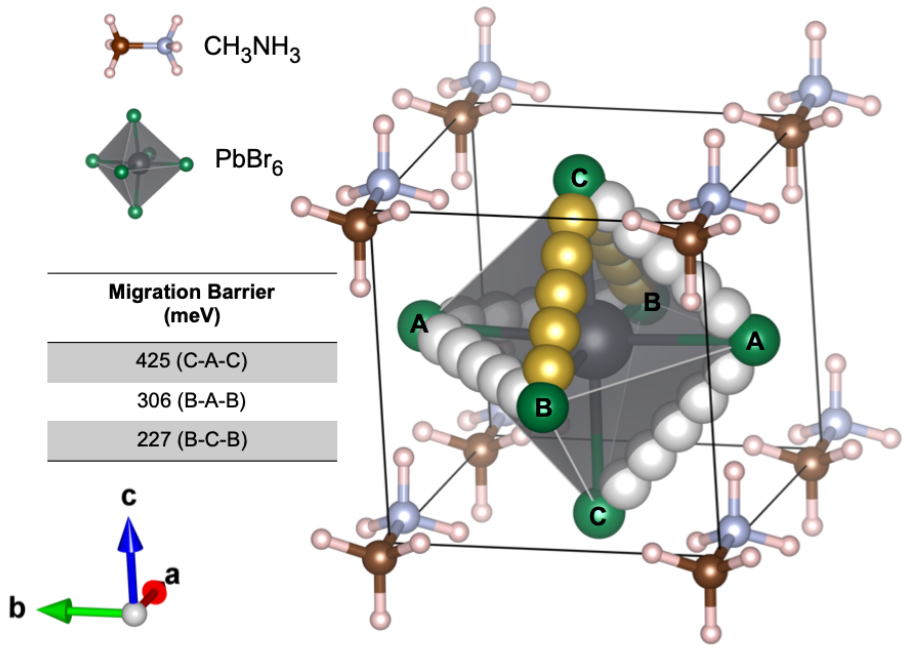

Figure 4.10. Estimated Br migration barrier via DFT. Schematic of Br^- diffusion pathways in $CH_3NH_3PbBr_3$ by nudged elastic band (NEB). The $PbBr_6$ octahedron becomes distorted after NEB relaxation resulting in primitive cell has lattice constants of 6.017, 6.041, and 6.115 Å, along the a-, b-, and c-axis, respectively. The geometrically distinct Br atoms are labelled as A, B and C and the corresponding migration energy barriers between Br atoms are shown in the table. White spheres represent the interpolated Br trajectories along pathway B-A-B and C-A-C, while yellow spheres indicating the smallest barrier migration for pathway B-C-B.[54]

4.6 Conclusion

In summary, we systematically manipulate the halide concentration laterally within a thin $CH_3NH_3PbBr_3$ single crystal by applying a voltage bias. We observe the changes of Br distribution at the nanoscale by means of n-XRF. The halide migration is directly correlated to variations in PL response. As Br^- migrates away from the negatively-biased electrode and the perovskite becomes locally sub-stoichiometric, the PL intensity decreases. NEB calculations indicate that the alignment of the methylammonium cation under bias forms channels that facilitate halide migration along the field direction. Combining the quantitative analysis of ion migration with local optoelectronic characterization provides insight into the fundamental operation of halide perovskite devices. The link between intrinsic point defect migration and

photoluminescence intensity makes it clear that controlling the crystal chemistry is paramount. Possible strategies to mitigate the effects of Br migration and improve optoelectronic performance in the perovskite include growing perovskites in halide-rich conditions[52] or applying post-growth treatments to lower the concentration of halide vacancies. Future work is needed to understand the defect kinetics of ion migration as a function of the absorber chemistry and to reveal the nature of the optoelectronic defects that arise under bias to achieve the full potential of the hybrid perovskite materials for optoelectronic devices.

4.7 Supplemental Information

Estimation of Br mobility

Given the applied voltage 2V and the gap space between electrodes 10 μm, the calculated electric field (E) is 2000 V/cm. Our lower bound for the drift velocity v is estimated to be $5.56 \times 10^{-7} cm/s$ using the distance d between electrodes and the 1800s duration t of apply bias, $v = d/t$. The lower bound estimate of the Br mobility at room temperature is calculated using Eq. 4.1,

$$\mu = v/E \tag{4.1}$$

where v is the velocity, μ is the mobility and E is the applied electric field.

Spatially resolved photoluminescence

A WITec alpha300 SR confocal imaging microscope was used to collect photoluminescence spectra of $CH_3NH_3PbBr_3$ crystals while the crystal was being moved using a piezostage. Sample was excited with a 405 nm diode laser (Thorlabs S1FC405) through a NA 0.9 objective and the luminescence was collected in reflection using a UHTS 300 spectrometer. The spectral resolution of the spectrometer is ¡ 0.09 nm. The calibration of the spectral response of the collection optics, fiber, and spectrometer was done with a standard mercury light source, and the spectrum was corrected accordingly.

The spatially-resolved PL maps are obtained by integrating the PL intensity within the optical fluorescence peak width, from 500-580 nm. The relative changes of PL intensity (ΔPL) is computed using Eq. 4.2,

$$\Delta PL^{X}(\%) = \frac{PLI^{X} - PLI_{initial-0V}}{PLI_{initial-0V}} \times 100 \tag{4.2}$$

where *PLI* is the photoluminescence intensity and X indicates the number of map.

Br vacancy migration barrier from NEB simulations

All density functional theory (DFT) calculations were performed using the Vienna *Ab initio* Simulation Package (VASP)[204] within the projector augmented-wave approach.[205] Spin-polarized calculations using the Perdew-Burke-Ernzerhof (PBE) generalized-gradient approximation (GGA)[206] functional were used for structure relaxations and all analyses were carried out using the Python Materials Genomics (pymatgen) library.[207] We performed climbing image nudged elastic band (Cl-NEB) calculations using $2 \times 2 \times 2$ supercells (8 formula units) of the lowest energy structure obtained for cubic $CH_3NH_3PbBr_3$ to minimize the interaction between periodic images. To study Br^- vacancy migration, a single positively-charge Br^- vacancy (V_{Br^+}) was introduced and overall charge neutrality was achieved by compensating background charge. A $2 \times 2 \times 2$ k-point grid and energy cutoff of 520 eV were adopted for NEB calculations. The forces were converged to 0.05 eV/Å.

4.8 Acknowledgement

Chapter 4, in full, is a reprint of the material "Direct Observation of Halide Migration and its Effect on the Photoluminescence of Methylammonium Lead Bromide Perovskite Single Crystals" as it appears in Advanced Materials, Yanqi Luo, Parisa Khoram, Sarah Brittman, Zhuoying Zhu, Barry Lai, Shyue Ping Ong, Erik C. Garnett, and David P. Fenning, 2017, 1703451, 1-7. The dissertation author was one of the primary investigators and author of this material.

Chapter 5

Mixed A-site and A Single Halide Composition Results in A-site Instability

In Chapter 3 and 4, evident n-XRF data illustrates the challenge in homogenized chemical mixing and the present of highly mobile Br ions even at room temperature. These phase segregation and chemical instability, leading to poor device stability under various environmental stressors, are the great hindrance to their development. A-site modulation in ABX3 (methylammonium (MA) free in particular) have proven to be effective in improving the operational stability of perovskite absorbers. Most absorbers, however, still suffer from degradation under operating conditions, the mechanism of which requires investigation. Here, we systematically monitor the evolution of photovoltaic performance in high-performing formamidinium-cesium lead iodide ($FA_{0.9}Cs_{0.1}PbI_3$) perovskite solar cells (PSCs) over 600 hours of aging under stressors intrinsic to operating conditions: heat, one-sun illumination, and stabilized power output (SPO). We find that although $FA_{0.9}Cs_{0.1}PbI_3$-based PSCs exhibit reasonable thermal stability, their stability under illumination or SPO is far behind commercial demands. Synchrotron-based nanoprobe X-ray fluorescence and X-ray beam induced current measurements reveal that current-blocking Cs-rich phases segregate during stress testing. The decrease in performance correlates with the resulting number density of the Cs-rich clusters, and this number density increases in conditions with higher carrier concentration. Our findings provide a microscopic view of $FA_{0.9}Cs_{0.1}PbI_3$ absorber in response to the intrinsic stressors, and shed light on the cation-dependent phase

segregation under operational conditions, which can be expanded to other hybrid perovskite systems and guide in composition design for more stable perovskite optoelectronic devices. Note that device fabrication and accelerated aging tests were conducted by Nengxu Li, one of the co-authors of this work.

5.1 Introduction

The performance of organic-inorganic halide perovskite solar cells (PSCs) has improved dramatically in the past decade, with the highest certified power conversion efficiency (PCE) of 25.2% using a polycrystalline perovskite absorber,[7] which is approaching the state-of-art for crystalline silicon solar cells. However, the poor stability of perovskite-based devices in environments of elevated temperature, high humidity, and/or intense irradiation has delayed the commercial deployment of PSCs.[208, 209, 210] Although packaging can extend the stability of PSCs by preventing moisture ingress and reducing evaporation of volatile components in perovskite absorbers upon heating,[211, 75] the continuous operation under intense irradiation for PSCs indicates that improving the intrinsic illumination and operational stability of perovskites and understanding the degradation mechanisms accounts for the poor stability remains crucial to the effort to harden PSCs for reliable commercial use.

Degradation pathways have been investigated in early developed perovskites, which are known to easily decompose and present a large amount of Schottky or Frenkel defects.[178, 212] For instance, MA-based PSCs are found to be thermally unstable at 85 °C under N_2 environment due to the decomposition of MA through gradual sublimation of HI and CH_3NH_2, leaving inactive PbI_2 behind.[67] Degradation can also be accelerated in an environment with oxygen and moisture,[213, 214] further pointing out the intrinsic instability of MA-based perovskites.[215] Defect formation is a prevailing issue in almost every type of halide perovskite absorber, and is mainly attributed to the weak bonding in the crystal (such as Pb-I ionic bonds, hydrogen bonds, and vander Waals interactions)[216, 217] and the soft crystal lattice.[218] Combined with the low

energy barrier for ionic migration,[49, 219] halides and organic cations readily migrate through perovskite films, leading to ionic redistribution or even phase segregation upon prolonged testing in the presence of an internal electric field, especially under illumination and/or applied electric load.[220, 221, 173] This raises a key challenge for the operation of perovskite solar cells under various stressors, including heat, continuous illumination and maximum power point tracking.

A-site compositional modulation is a common approach to tune the intrinsic stability of hybrid halide perovskites.[40, 168, 74] To overcome the poor thermal stability of MA, composition engineering using some combination of MA^+, FA^+, and Cs^+ appears to be very effective. Among these possible combinations, the double-cation, mixed FA^+ and Cs^+ compositions (*e.g.* $FA_{0.9}Cs_{0.1}PbI_3$) are commonly seen to stabilize the photoactive black phase of perovskite in high-performing PSCs,[72, 71, 73] so far as to pass standard 85°C/85% relative humidity accelerated testing with the aid of encapsulation.[75] In addition, the incorporation of cesium into FA/MA based perovskites to form triple cation configuration[11] or adding rubidium into CsFAMA perovskites to form "cation cascade" perovskite absorbers[12] all exhibited enhanced illumination and operational stability. However, although PSCs have demonstrated high efficiency (over 20%) with enhanced thermal stability by A-site component engineering,[222] they still exhibit undesirable performance losses under illumination and/or operational condition, of which the corresponding degradation mechanisms have been rarely investigated microscopically.

Herein, we systematically monitor the performance of high performing MA-free PSCs ($FA_{0.9}Cs_{0.1}PbI_3$) over 600 hours of various environmental conditions, including dark, heat, illumination, and stabilized power output (SPO, under illumination and fixed electric load). Current density-voltage (J-V) results indicate that while $FA_{0.9}Cs_{0.1}PbI_3$ based PSCs exhibit respectable thermal stability, they show considerable performance degradation under illumination and SPO stressors. Further, constant illumination have obvious impacts on absorber composition, resulting in phase segregation as suggested by X-ray diffraction (XRD) and photoluminescence (PL). Synchrotron based X-ray fluorescence microscopy with nanoscale spatial resolution (n-XRF) revealed heterogeneous Cs distribution after stress. *In-situ* XRF/X-ray-beam induced

current (XBIC) show the Cs-rich clusters to be photoinactive and current blocking, which is likely the main cause of performance loss in $FA_{0.9}Cs_{0.1}PbI_3$ PSCs.

5.2 Device Stability under Various Stressors Intrinsic to Operation

To assess PSCs instability and underlying failure modes under prolonged stressed testing, we monitor device photovoltaic performance over 600 hours of exposure to four distinct stress conditions: 85°C heating in the dark (labeled Heat), 1 sun illumination at near room temperature (35 $\pm$ 10 °C) in open circuit condition (labeled Light) and a stabilized power output at initial maximum power point under 1-sun illumination at near room temperature (labeled SPO). The reference sample (labeled Ref) is stored in the dark at room temperature. Notably, all samples are maintained in an N_2 environment. All devices are unencapsulated with a nominal composition of $FA_{0.9}Cs_{0.1}PbI_3$, and are fabricated in the conventional n-i-p architecture: ITO/SnO_2/Perovskite/Spiro-OMeTAD/Au. The distribution of PSC device performance and photovoltaic parameters after fabrication (Figure 5.1) show an average power conversion efficiency (PCE) of 19.16 $\pm$ 0.55 %, with the champion device achieving a PCE of 20.12% (Figure 5.2). Further details regarding device architecture and fabrication can be found in the supplemental information.

The evolution of photovoltaic performance of devices under Ref, Heat, Light and SPO stressing are shown using J-V measurements in Figure 5.3. J-V data indicates that while the Ref devices show nearly no loss in PCE (–1.0 %) after 600 hours, the Heat, SPO, and Light samples all show significant losses in PCE (–18.0, –47.7, and –66.3%, respectively). Except for the Ref samples, Heat caused the slowest PCE decay and expressed symptom of a slight decrease in fill factor (FF). On the other hand, SPO and Light stressors affected device performance considerably, resulting in significant declines in open-circuit voltage (Voc), short-circuit current (Jsc), and FF Figure 5.3. These phenomena suggest that the $FA_{0.9}Cs_{0.1}PbI_3$ absorber has good

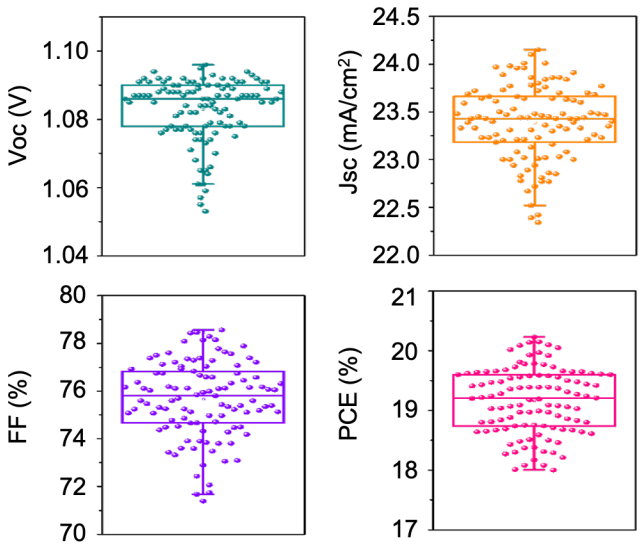

Figure 5.1. Distribution of device parameters of $FA_{0.9}Cs_{0.1}PbI_3$ based Perovskite Solar Cells. A total of 109 cells was fabricated and tested.[114]

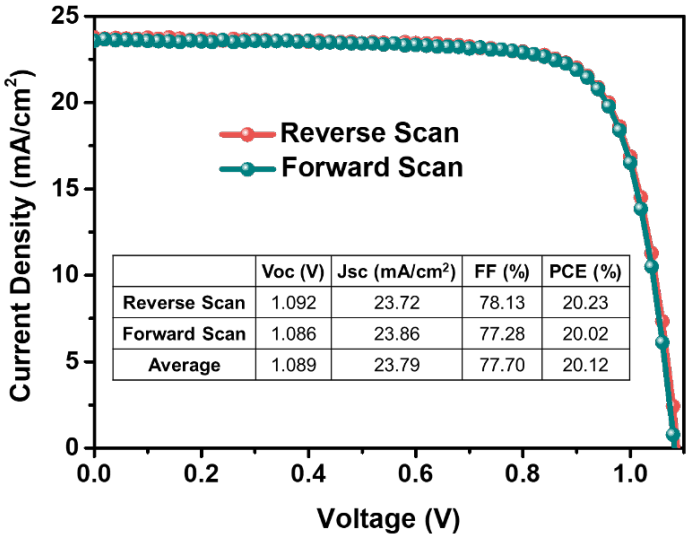

Figure 5.2. Current density-voltage (J–V) measurement with reverse (1.2 V to –0.2 V) and forward (–0.2 V to 1.2 V) scan of the best performing $FA_{0.9}Cs_{0.1}PbI_3$ perovskites device under 1 Sun illumination.[114]

thermal stability, but is unstable in illuminated conditions.

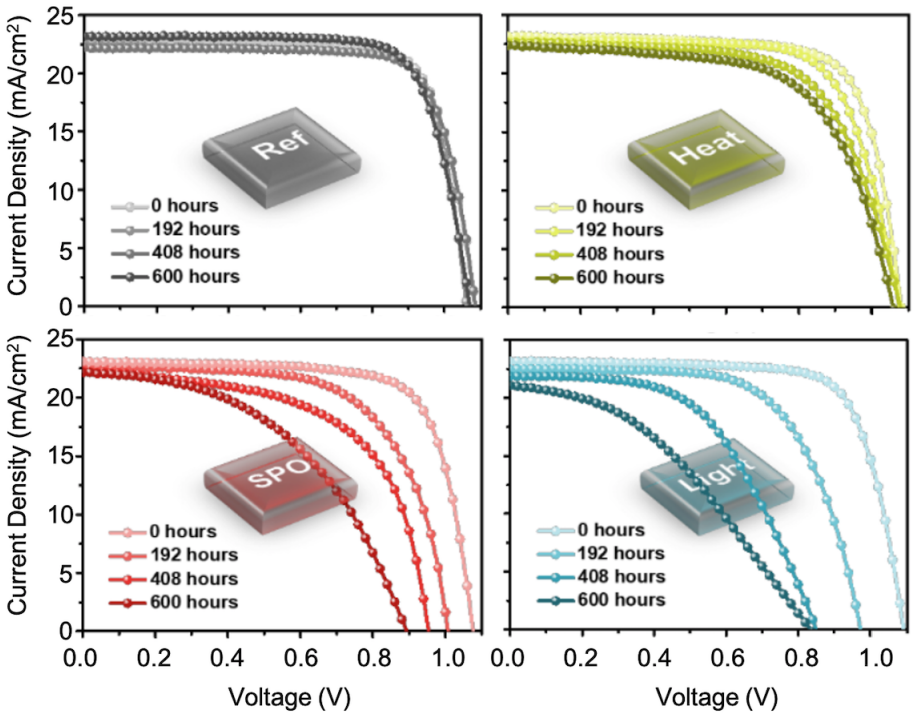

Figure 5.3. PSCs performance as a function of aging time. (A-D) are J-V curves of samples stored in dark at near room temperature (35 ± 10°C), in elevated temperature with temperature of 85°C, in 1 Sun illumination at near room temperature, and in stablized power output at V_{app} = 0.7 V, respectively.[114]

5.3 Micron-scale Cs-rich particles form in stressed PSCs

n-XRF is used to study in greater detail the spatial distribution of the film constituents. Fluorescence maps were collected using a focused synchrotron X-ray probe with a 250 nm full-width half maximum (FWHM). The X-ray energy was set at 7 keV to maximize the measurement sensitivity for I and Cs L-line excitation. The light elements (C, H, N) in the formamidium (FA^+) cation are not observable in the XRF measurement.

The local Cs:I stoichiometry is homogenous within the Ref device, but Cs-rich clusters are observed in all stressed devices (Figure 5.4A-D). The number density and size of Cs-rich clusters vary across these three stressors. A few large Cs-rich clusters are seen in the Heat sample, while the clusters become increasingly small and numerous in the SPO and Light conditions.

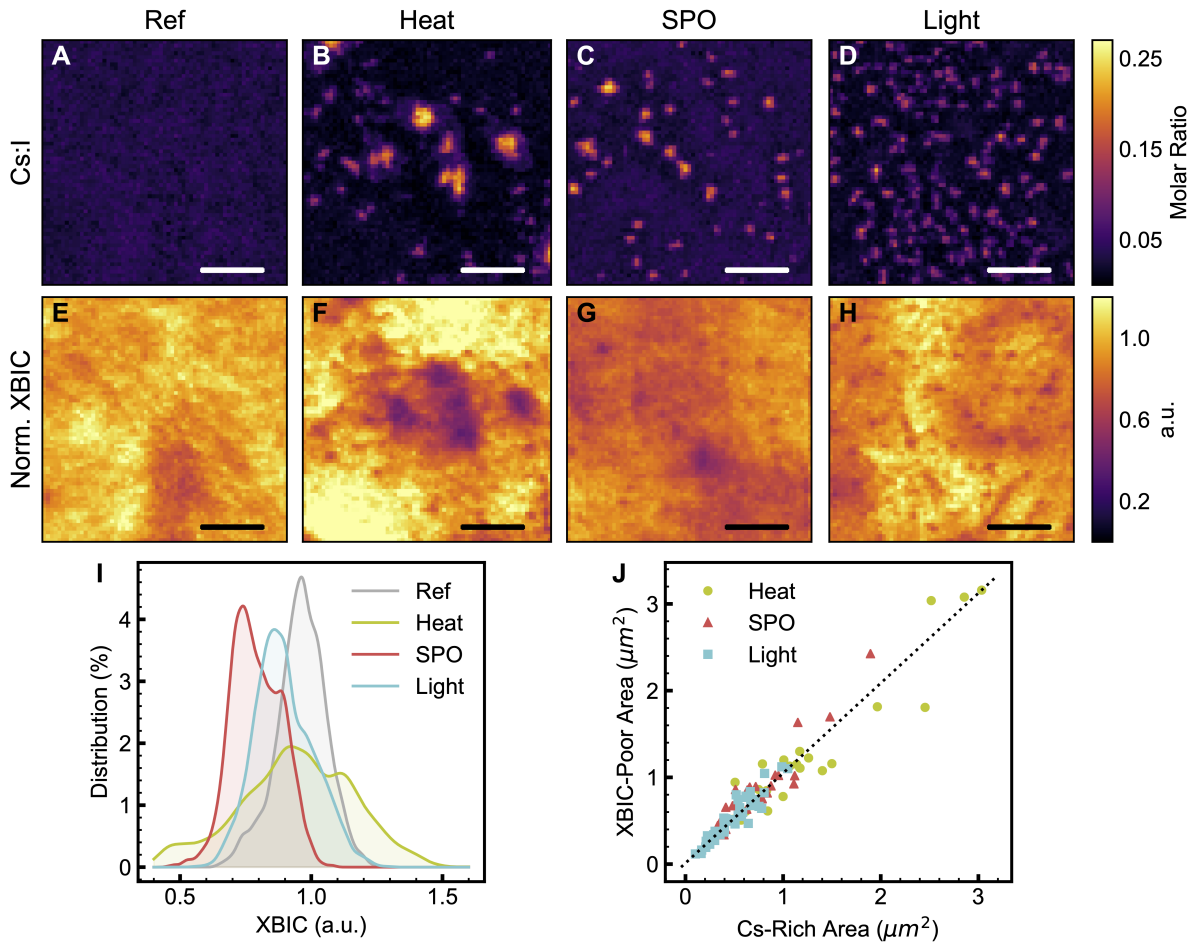

Figure 5.4. (A-D) X-ray fluorescence (XRF) mapping of perovskite devices that are subjected to Ref, Heat, SPO, and Light stressing conditions. (E-H) X-ray beam induced current (XBIC) mapping of the corresponding regions shown in (A-D). Scale bar is 5 μm. (I) Pixel-wise frequency distribution of the XBIC current observed in each sample. (J) Correlation of feature areas as measured by XRF (Cs-rich regions) and XBIC (current-poor regions) in Heat, SPO and Light treated samples.

The chemical nature of the Cs aggregates is likely to be Cs-rich phase (such as $CsPbI_3$, which is detected in Light and SPO samples as shown in Figure 5.5) with the highest Cs:I molar ratio of 0.27, which is almost an order of magnitude higher than the ratio in originally prepared perovskite, where the nominal Cs:I molar ratio is expected to be 0.033 for the $FA_{0.9}Cs_{0.1}PbI_3$ stoichiometry.

To reveal the electronic role of these Cs-clusters, *in-situ* X-ray-beam-induced current (XBIC) was conducted for Ref and stressed devices simultaneously with XRF measurements.

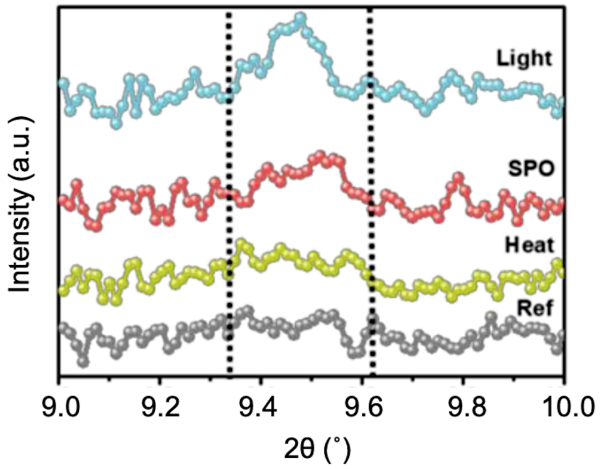

Figure 5.5. X-ray diffraction (XRD) patterns of perovskite samples that are subjected to Ref, Heat, SPO, and Light stressing conditions.

The close correlation between local Cs enrichment and reduced current collection indicates that the Cs-rich clusters observed in the Heat, SPO and Light treated devices suppress charge collection (Figure 5.4E-H). For example, XBIC poor areas in the centre of Figure 5.4F are found to align well with the large Cs-rich clusters in the centre of Figure 5.4B. Similarly, small current suppressing areas in Figure 5.4G correspond to Cs-rich regions in Figure 5.4C. This can be easily illustrated by overlaying and the Cs-XRF and XBIC maps together shown in Figure 5.6. The overall effect of the appearance of current suppressing areas is illustrated by histograms of the XBIC signal in each sample shown in Figure 5.4I. To avoid misinterpretation, the XBIC data shown was corrected to the extent possible for variations in X-ray absorption and subsequent carrier generation due to absorber thickness and morphology variation (Figure 5.7, see Chapter 2 for details). This procedure does not remove the effect of morphology fully (*e.g.* variations remain in the relatively homogeneous Ref sample in Figure 5.4E), likely due to experimental uncertainty of local film thickness and variation of carrier collection probability with film thickness.

We conclude that the Cs-rich clusters are current-blocking and photoinactive. This is determined by performing a cluster analysis and comparing the feature size of XBIC-poor and Cs-rich areas. A correlation plot of the Cs cluster feature sizes as measured by XRF and XBIC is

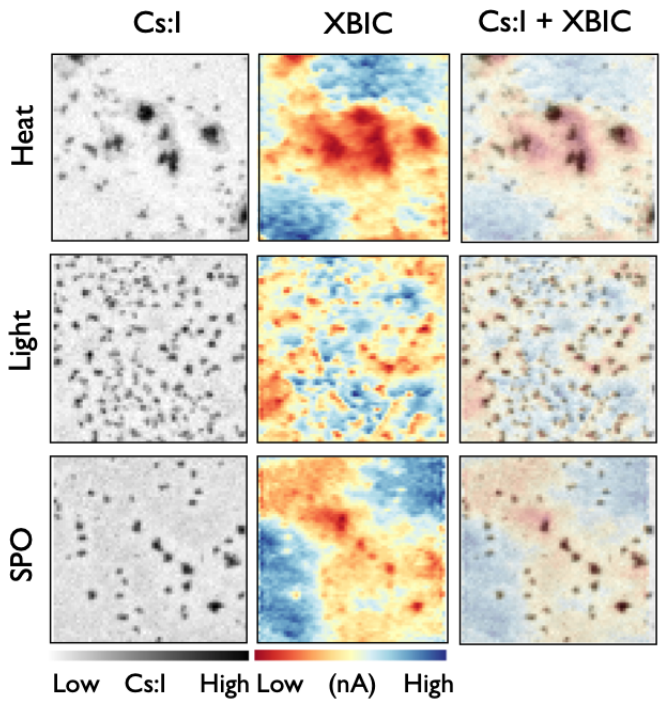

Figure 5.6. Overlaying normalized Cs-XRF and XBIC maps to illustrate the current blocking effects from Cs-rich clusters. These are the same Cs:I XRF and XBIC maps shown in Figure 5.4 previously.

shown in Figure 5.4J, in which data from all stressed devices is distributed along the guideline with a slope of 1. The cluster analysis makes explicit the positive correlation and reveals that the XBIC feature size is very close to the size of Cs aggregates in the elemental map.

5.4 Photo Induced Carriers May Provide Additional Driving Force for Phase Segregation

This microscopic assessment using n-XRF/XBIC of A-site instability in $FA_{0.9}Cs_{0.1}PbI_3$ devices reveals that the metstability of the mixed A-site perovskite phase is overcome by even mild thermal and optical energy inputs. Interestingly, a high density of Cs-rich clusters nucleate upon continuous light soaking (Light and SPO conditions), while Cs aggregates are larger in size and fewer in number after elevated thermal exposure (85°C). This finer distribution after extended illumination compared to the Heat sample suggests that there is a smaller critical nucleus size

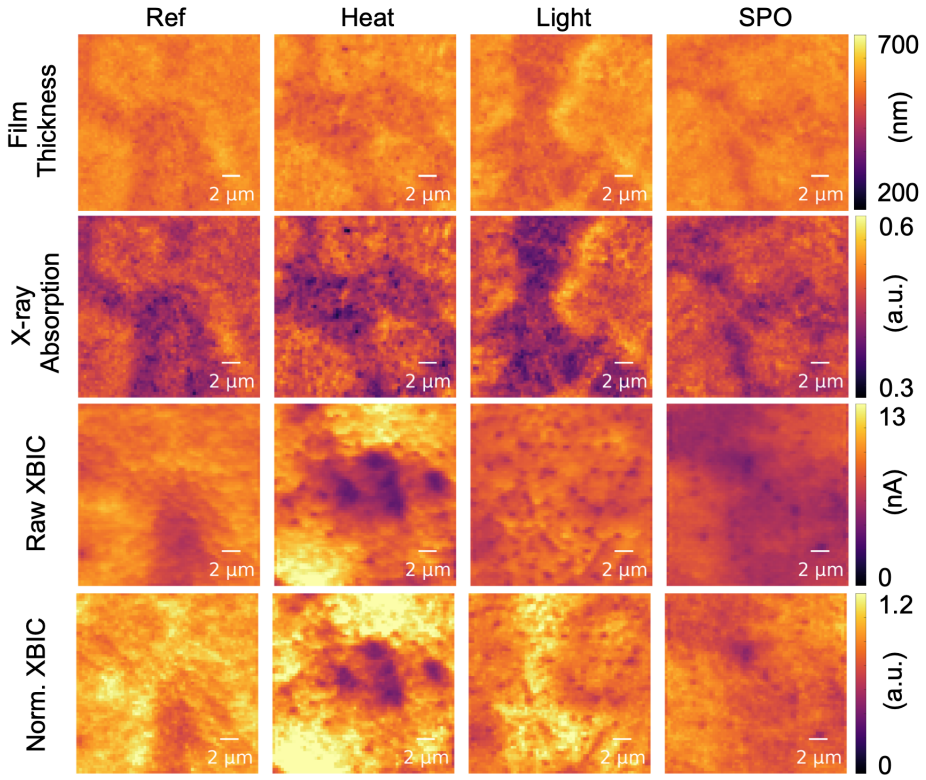

Figure 5.7. Perovskite film thickness estimation is shown in Row 1 by scaling average of Pb+I XRF maps to nominal film thickness of 500 nm. Row 2 is the X-ray absorption profiles approximated using Eq 2.5. Row 3 has the raw XBIC prior to absorption normalization and the normalized data is shown in Row 4.

for nucleation of the Cs-rich phase under illuminated conditions. The temperature difference is not enough to substantially enhance ripening kinetics.[49, 223] On the contrary, illumination is known to enhance ionic conductivity by orders of magnitude.[224] Such enhancements in ion transport would in principle facilitate the illuminated sample reaching a more ripened distribution relative to the Heat sample within the same stressing time. That the Cs-rich particles are smaller and more numerous in the illuminated sample instead suggests that a larger energetic driving force exists for phase segregation under illumination than at 85 °C, as in classical nucleation theory the critical radius is inversely related with the thermodynamic driving force.[225]

We interpret the presence of a larger driving force for phase separation in the Light and SPO samples to indicate that the presence of photoexcited carriers helps drive the phase segregation. Amongst the samples, the higher the carrier concentration, the higher the density

and the smaller the Cs clusters (Figure 5.4A-D). In the Light and SPO samples, where a higher density of smaller Cs clusters correlates with high carrier concentration.

In conclusion, we have evaluated MA free mixed FA-Cs iodide perovskite stability upon prolonged accelerated testing under various environmental stressors intrinsic to PV operation. Either 1-sun illumination or heating like that present in the field is enough to induce degradation over hundreds of hours of operation by microscopic phase separation into an inactive Cs-rich secondary phase. Although heterogeneous halide distribution in microscopic scale is avoided with this simpler composition, $FA_{0.9}Cs_{0.1}PbI_3$ is hindered by A-site instability particularly.

5.5 Acknowledgement

Chapter 5, in full, is currently being prepared for submission for publication of the material "Microscopic degradation mechanism in MA-free perovskite solar cells under various stressors intrinsic to operation", Nengxu Li, Yanqi Luo, Zehua Chen, Xiuxiu Niu, Xiao Zhang, Jiuzhou Lu, Rishi Kumar, Junke Jiang, Huifen Liu, Xiao Guo, Barry Lai, Geert Brocks, Qi Chen, Shuxia Tao, David P. Fenning, Huanping Zhou. The dissertation author was one of the primary investigators and author of this material.

Chapter 6

Incorporation of A-site alkaline ions to achieve homogeneous halide distribution in high performing perovskite solar cells

The high degree of in-plane spatial variation and mobile nature of halide ions, perovskite thin films may potentially face the big challenge in scaling highly-efficient devices to larger areas. To achieve films with homogenized halide distribution , composition engineering on A-site mixing appears to be effective with evident data provided in this chapter. Using synchrotron-based nano–x-ray fluorescence and complementary measurements, we found that the halide distribution becomes homogenized upon addition of cesium iodide, either alone or with rubidium iodide, for substoichiometric, stoichiometric, and overstoichiometric preparations, where the lead halide is varied with respect to organic halide precursors. Halide homogenization coincides with the improved photovoltaic device performance. We found that rubidium and potassium phase-segregate in highly concentrated clusters. Alkali metals are beneficial at low concentrations, where they homogenize the halide distribution, but at higher concentrations, they form recombination-active second-phase clusters. Note that device fabrication was conducted by Dr. Juan Pablo Correa-Baena, one of the co-authors of this work.

6.1 Introduction

The highest reported power conversion efficiencies (PCEs) for lead halide perovskite solar cells (PSCs) have been achieved with mixed methylammonium (MA) and formamidinium (FA) A-site cations.[68, 226, 69, 171] When utilizing FA and I as the main composition, incorporation of methylammonium chloride (MACl) has shown to increase the device performance from below 20 to 24.02% with 1200 hr operational lifetime at room temperature, by forming the an intermediate-phase that suppressed the crystallization of the photoinactive $FAPbI_3$.[227] Additionally, phenethylammonium iodide (PEAI) was applied as a surface passivating agent on 3D $FA_{1-x}MA_xPbI_3$ perovskite with stable performance for 500 hr at $85°C$.[228] Tuning the stoichiometry of the organic to the inorganic ions is critical for achieving high photocurrents and stability.[134] Cs has been used as the A-site cation to explore more complex compositions, including Cs and MA, Cs and FA, and Cs, MA, and FA.[68, 71, 73, 11, 10, 229] Cs containing $Cs_{0.17}FA_{0.83}Pb(Br_{0.17}I_{0.83})_3$ was demonstrated to have respectful thermal stability by withstanding temperature cycling test with advanced encapsulation.[211] Similarly, adding Rb into a multi-cation perovskite improved efficiency [12, 230] and enhanced device stability at elevated temperatures of 85°C.[12] The improved performance may be the result of increased charge carrier lifetime and mobility.[231]

Despite these impressive results, the mechanisms that form the basis for improved electronic properties, performance, and stability upon changes in the precursor stoichiometry and the addition of alkali metals are not yet well understood. Past work hinted at the suppression of low-dimensional wide–band gap polymorphs, which may act as recombination-active sites.[11, 12, 231] In addition, previous studies with bulk techniques[71, 73, 11, 12, 232] averaged over large areas (0.2 to 1 cm^2) may have overlooked minority-phase formation and elemental agglomeration at the nanoscale.

We used mapping techniques with nanoscale resolution to elucidate the elemental distribution of the alkali metals and their relation to electronic properties and device performance.

Synchrotron-based nanoscale x-ray fluorescence (n-XRF) mapped the elemental distribution in multi-ion perovskites. Where alkali metals were added, the halide distribution became homogeneous for films with excess lead halide precursor. Transient absorption spectroscopy mapping showed that perovskite films without addition of alkali metal iodides (and with segregated halides) had greater heterogeneity in the charge carrier dynamics than those with CsI, RbI, or both. Also, Rb and K could segregate into large clusters. When the alkali metal additives exceeded 1%, we observed second-phase alkali metal–rich aggregates that induce charge carrier recombination at Rb-rich clusters.

6.2 Experimental Design and Device Performance

In addition to the perovskite films with 10% excess PbI_2 and $PbBr_2$ [overstoichiometric (OSt)], we prepared samples containing no excess (St) and with deficient lead halide precursor stoichiometry [substoichiometric (SSt)] with respect to the organic cations MA and FA. These perovskites have a composition of $(MAPbBr_3)_{0.17}(FAPbI_3)_{0.83}$, similar to those previously studied.[226, 11] We added 5% CsI, 5% RbI, 5% CsI and 5% RbI, or 5% KI with respect to the PbI2 (see Table 6.1 for details on compositions) for the OSt, St, and SSt samples, which we refer to as Cs-I/Br, Rb-I/Br, RbCs-I/Br, and K-I/Br, respectively. FAI and MAI were also added to understand the effect of adding additional organic cations to the OSt solutions. Perovskite thin films were prepared with the combinations X-I/Br, where X is the alkali metal added (or FAMA) and I/Br refers to the baseline perovskites.

Solar cells were prepared with a typical device structure (Figure 6.1A, see supplementary materials in Chapter 6.6). A transmission electron microscopy (TEM) cross-sectional image is shown for a PSC with I/Br (6.1b) perovskite [see Figure 6.2 for scanning electron microscopy (SEM) cross-sectional images of several compositions]. Representative current density–voltage ($J-V$) curves, including the back- ward and forward scans, for OSt I/Br and top performer RbCs-I/Br are shown in Figure 6.1, C and D, respectively. The champion device for the I/Br

Table 6.1. Compositions of the perovskite samples studied

Additive	Overstoichiometric	Stoichiometric	Substoichiometric
No alkali additives	[MABr]:[$PbBr_2$]=0.9 [FAI]:[PbI_2]=0.9	[MABr]:[$PbBr_2$]=1 [FAI]:[PbI_2]=1	[MABr]:[$PbBr_2$]=1.1 [FAI]:[PbI_2]=1.1
5% RbI (Rb-I/Br)	[MABr]:[$PbBr_2$]=0.9 [FAI]:[PbI_2]=0.9 + [RbI]:[PbI_2]=0.05	[MABr]:[$PbBr_2$]=1 [FAI]:[PbI_2]=1 + [RbI]:[PbI_2]=0.05	[MABr]:[$PbBr_2$]=1.1 [FAI]:[PbI_2]=1.1 + [RbI]:[PbI_2]=0.05
5% CsI (Cs-I/Br)	[MABr]:[$PbBr_2$]=0.9 [FAI]:[PbI_2]=0.9 + [CsI]:[PbI_2]=0.05	[MABr]:[$PbBr_2$]=1 [FAI]:[PbI_2]=1 + [CsI]:[PbI_2]= 0.05	[MABr]:[$PbBr_2$]=1.1 [FAI]:[PbI_2]=1.1 + [CsI]:[PbI_2]=0.05
5% KI (K-I/Br)	[MABr]:[$PbBr_2$]=0.9 [FAI]:[PbI_2]=0.9 + [KI]:[PbI_2]=0.05	[MABr]:[$PbBr_2$] =1 [FAI]:[PbI_2]=1 + [KI]:[PbI_2]=0.05	[MABr]:[$PbBr_2$]=1.1 [FAI]:[PbI_2]=1.1 + [KI]:[PbI_2]=0.05
5% CsI, 5% RbI (CsRb-I/Br)	[MABr]:[$PbBr_2$]=0.9 [FAI]:[PbI_2]=0.9 +[CsI]:[PbI_2]=0.05 + [RbI]:[PbI_2]=0.05	[MABr]:[$PbBr_2$]=1 [FAI]:[PbI_2]=1 +[CsI]:[PbI_2]=0.05 +[RbI]:[PbI_2]=0.05	[MABr]:[$PbBr_2$]=1.1 [FAI]:[PbI_2]=1.1 +[CsI]:[PbI_2]=0.05 +[RbI]:[PbI_2]=0.05
8.3% FAI 1.7% MAI (FAMA-I/Br)	[MABr]:[$PbBr_2$]=0.9 [FAI]:[PbI_2]=0.983 [MAI:[PbI_2]=0.017	No sample prepared	No sample prepared

perovskites yielded an open-circuit voltage (V_{OC}) of 1.09 V, short-circuit current density (J_{SC}) of 22.8 mA/cm^2, fill factor (FF) of 51%, and PCE of 12.6% under AM1.5 illumination. In contrast, the champion device prepared with RbCs-I/Br yielded V_{OC} = 1.10 V, J_{SC} = 22.7 mA/cm^2, FF = 76%, and PCE = 19%. The parameters were extracted from the backward scan, and no appreciable difference was observed between backward and forward scans.[12]

The performance of device replicates for each of the studied compositions is shown in Figure 6.1, E and F. For the OSt samples, V_{OC} (Figure 6.1E) and performance (PCE; Figure 6.1F) increased with the addition of Rb or Cs (or both) or FAMA, but decreased upon KI addition. The beneficial effect of cation addition has been ascribed to the reduction in concentration of the "yellow-phase" impurity of the FA-based perovskites.[73, 11] The time-resolved photoluminescence decay of the perovskites slowed considerably with the addition of the alkali metal iodides to the OSt perovskites (Figure 6.3),[233] in agreement with the increase in V_{OC} and other studies.[231] The J_{SC} values of these devices remained relatively constant with perovskite composition, and FF markedly increased with the addition of alkali metal iodides, with an especially large discrepancy between I/Br and RbCs-I/Br samples (with the exception of KI).

The St and SSt samples showed a very different trend. The former showed an increase in

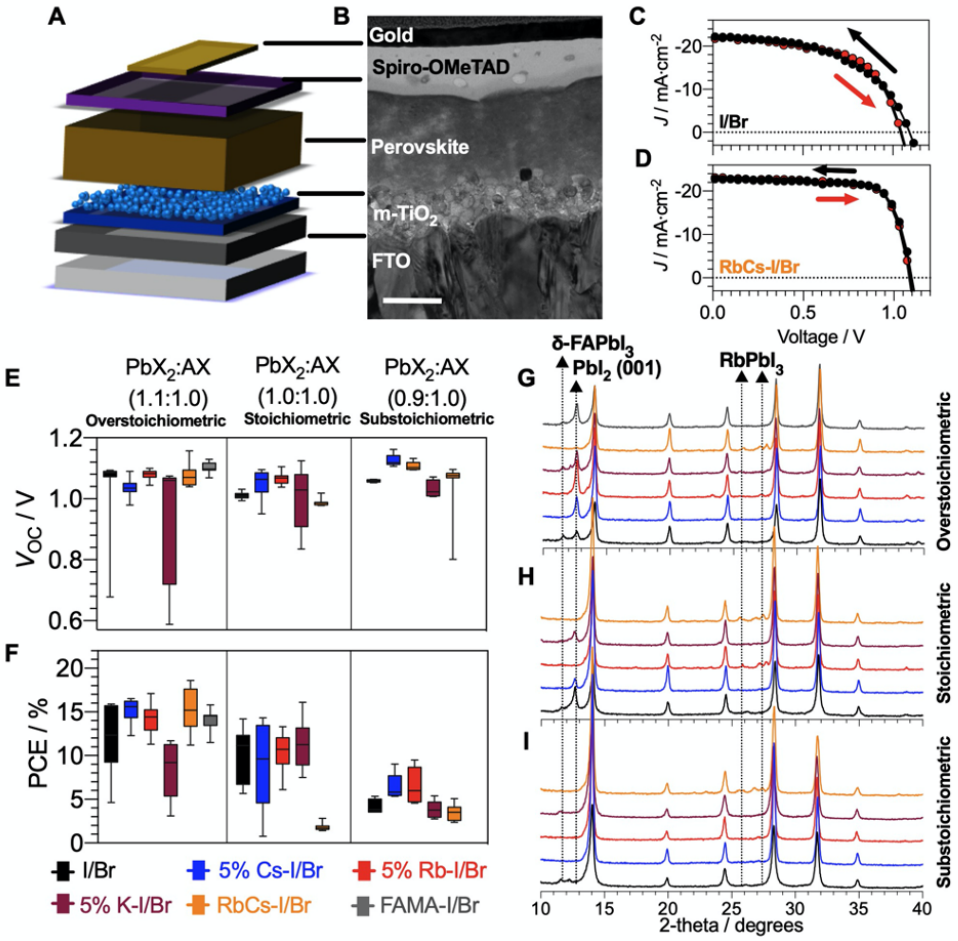

Figure 6.1. Perovskite thin film and solar cell characterization. (A) Schematic of the perovskite solar cells studied, accompanied by (B) the cross-sectional TEM for CsRb-I/Br device; scale bar is 200 nm. Perovskite solar cell current-voltage characteristics for (C) I/Br and (D) CsRb-I/Br. (E) Time-resolved photoluminescence decay, (F) X-ray diffractograms for the studied perovskite compositions with the estimated lattice constants and unit cell volume (G). (H) Full width at half maximum as obtained from select peaks in the 10 to 40 degree range, for a the perovskite films in (F).

V_{OC} (Figure 6.1E) upon alkali metal halide addition, with the exception of RbCs-I/Br, and an unmodified FF. However, performance was lower than that of the OSt samples (Figure 6.1I). The SSt samples showed an increase in V_{OC} and J_{SC} upon addition of CsI or RbI, but there was no benefit to adding KI or both RbI and CsI. All of the SSt samples showed low FF and low PCE (Figure 6.1F). We ascribed this lower performance to the formation of a thick organic layer at

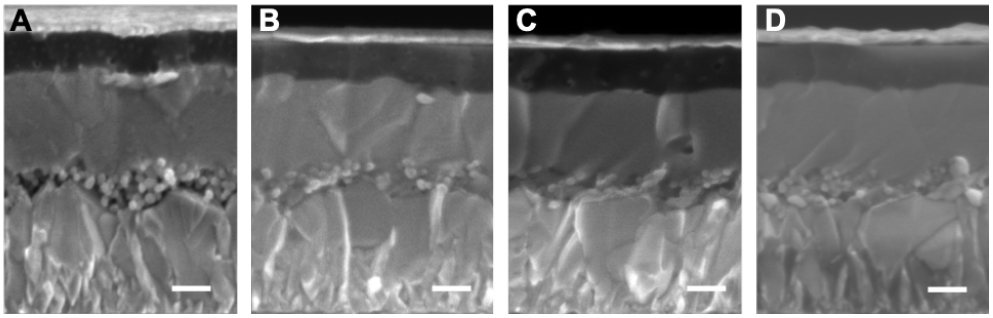

Figure 6.2. Cross-sectional SEM images of PSCs with an architecture FTO/compact TiO2/mesoporous TiO2/perovskite/Spiro-OMeTAD/Gold. The perovskite photoabsorber is varied as (A) I/Br, (B) Rb-I/Br, (C) Cs-I/Br, and (D) CsRb-I/Br. The scale bars are 200 nm.

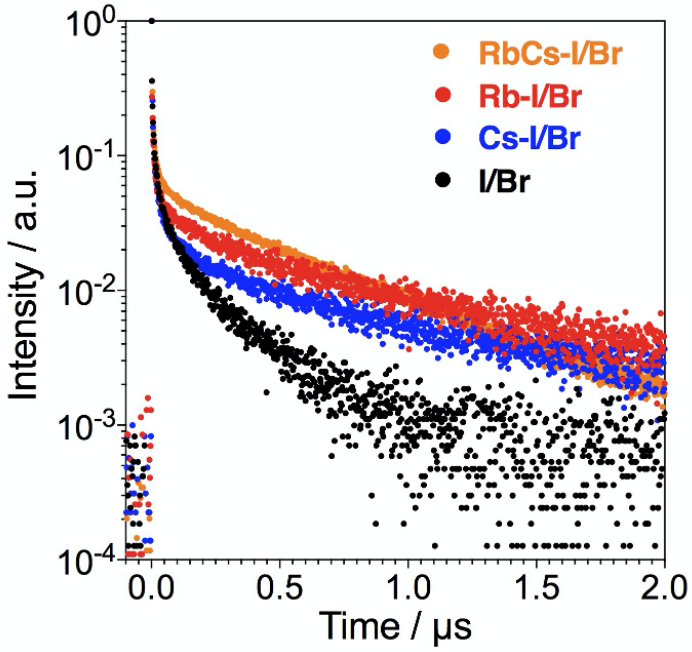

Figure 6.3. Time-resolved photoluminescence of perovskite thin film with different alkali-iodides and an overstoichiometric (Ost) composition.

the surface of the perovskite crystal, with a passivating effect.[134]. The highest V_{OC} and PCE values were measured for OSt samples with addition of both RbI and CsI.

Grazing incidence X-ray diffraction confirmed that the crystalline phases of the perovskite thin films (Figure 6.1, G to I) were bulk structures with cubic symmetry. We attribute the impurity peaks at low angles to small amounts of the nonperovskite one-dimensional (1D) phase of δ-

$FAPbI_3$ present in the OSt and St films. The peaks between 25° and 28° were assigned to the non-perovskite 1D $RbPbI_3$ (Figure 6.4).

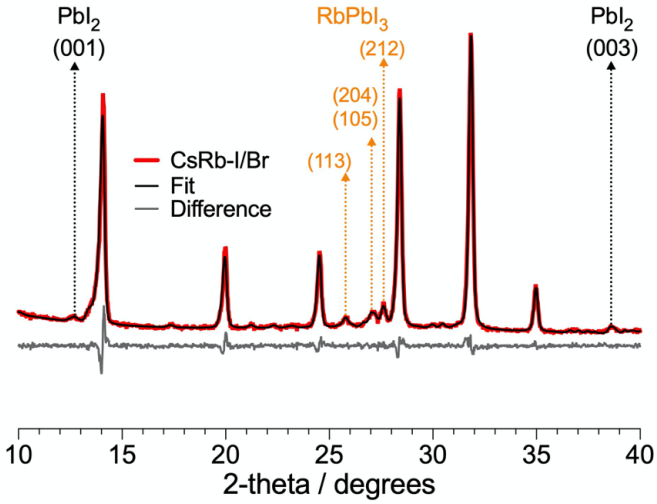

Figure 6.4. Structural analysis for CsRb-I/Br perovskite.Refined scan over the whole range of angles is shown to highlight secondary phases of 1D $RbPbI_3$ between 25° and 28°.

Our results confirmed that addition of RbI and CsI suppresses the formation of the PbI_2 phase. The relative peak intensity of the PbI_2 (001) peak at 12.63° decreased drastically upon addition of both RbI and CsI, with little to no effect with the addition of CsI, RbI, KI, and FAI and MAI in the OSt films (Fig. 1G). Similarly, the addition of both CsI and RbI markedly suppressed the PbI_2 peak; a more modest effect was seen with the addition of the individual alkali iodides in the St films (Figure 6.1H). Samples based on the SSt perovskite showed suppression of the PbI_2 (001) peak upon addition of all alkali iodides, with a δ-FAPbI3 phase remaining upon KI addition (Figure 6.1I).

6.3 Distribution of Halide in Perovskites with Alkaline Ions

To further understand the role of CsI, RbI, or KI addition, we performed n-XRF on all perovskites. The n-XRF resolution was limited by a 250-nm x-ray beam (FWHM at 16.3 keV). $Rb_{K\alpha}$, $I_{L\alpha}$, $Br_{K\alpha}$, and $Pb_{L\alpha}$ XRF emission from the perovskite absorber was detected, but C

and H in the FA and MA cations are too light to be detected. In the n-XRF maps, all of the OSt samples exhibited Br-poor clusters (Br:Pb molar ratio less than 0.48, versus the expected molar ratio of 0.49).

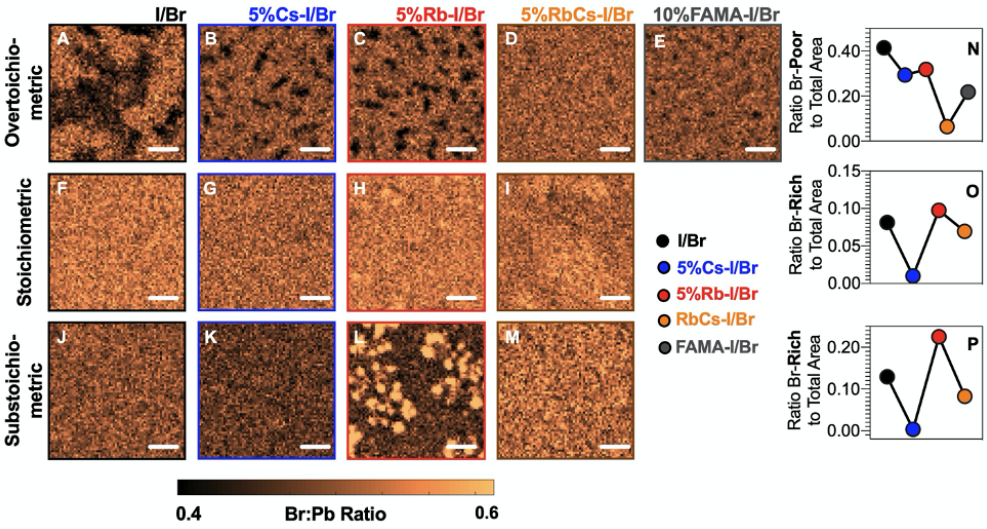

Figure 6.5. Halide Distribution. (A to M) n-XRF mapping indicates heterogeneous distribution of Br as a function of alkali metal incorporation and stoichiometric composition of the perovskite films. Br-poor [(A) to (E)] and Br-rich [(F) to (M)] areas are discernable. (N) Area fraction of the overstoichiometric Br-poor regions with respect to the whole n-XRF map. (O and P) Area fraction of the stoichiometric (O) and substoichiometric (P) Br-rich regions. Scale bars, 2 μm.

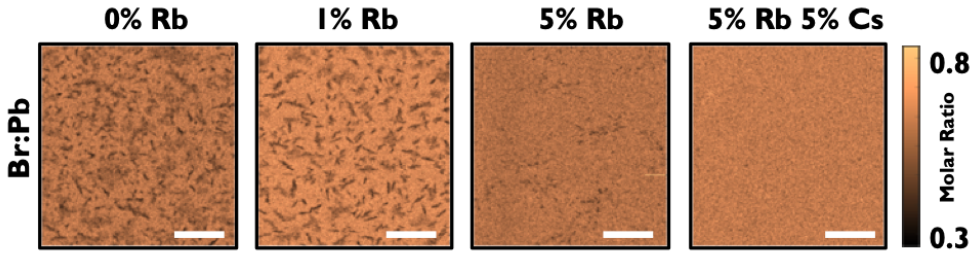

Figure 6.6. Halide homogenization as alkali ion loading increases. The Br:Pb XRF maps are used to reveal the halide homogenization in various alkali ion loadings. The alkali ion assisted homogenization effect occurs with Rb concentrations above 1% Rb is introduced. Scale bars are 10 μm.

The OSt I/Br perovskite, containing no alkali ions, showed large clusters of lower Br content, 6 to 8 μm in size; 41% of the scanned region was Br-poor (Figure 6.5, A and N). Upon

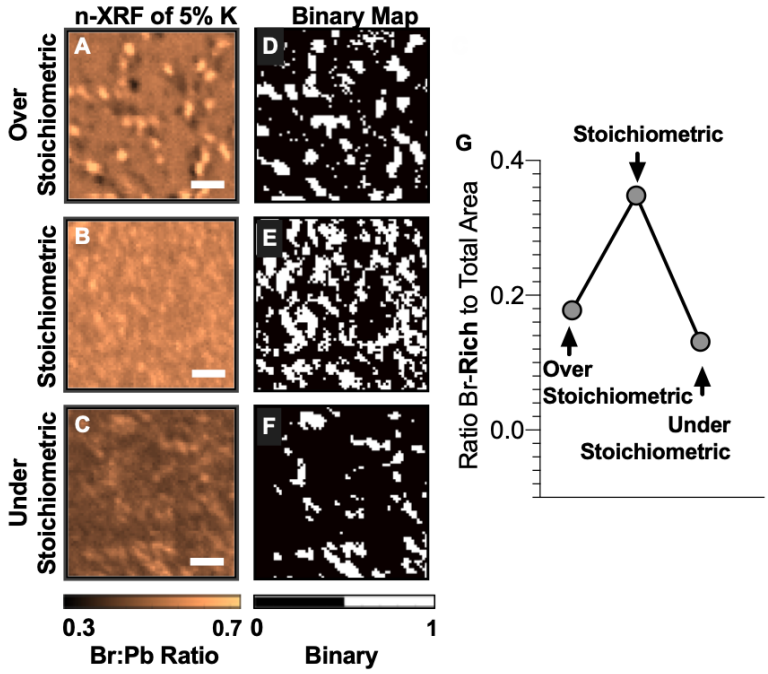

Figure 6.7. Example of Br cluster selection in samples with different stoichiometries and the addition of 5% molar of KI. (A to C) The Br:Pb XRF ratio maps with different stoichiometries. (D to F) The corresponding Br:Pb binary maps are produced by thresholding the maps in A to C, where pixels with Br:Pb value smaller than 0.54, 0.57, or 0.5 for over-stoichiometric, stoichiometric and substoichiometric respectively, are assigned to have value of 1 and the is assigned to have value of 0. (G) The area fraction of Br-rich with respect to total area of the over stoichiometric, stoichiometric, substoichiometric. The length of scale bar is 2 μm. The cluster analysis for distinguishing Br:Pb rich areas was carried out using *bwconncomp* and *regionprops* algorithm in MATLAB.

RbI or CsI addition, or both, we observed homogenization in Br (Figure 6.5, B to D). The Br-poor area fraction was reduced to 32% and 29% for individual RbI and CsI addition, respectively. As a control experiment, we added FAMA to the OSt I/Br solution (Figure 6.5E) and observed modestly improved homogeneity of Br. With both RbI and CsI addition, only 6% of the total area was Br-poor (Figure 6.5D), hence this combination yields the most halide homogenization. Slight halide homogenization by RbI occurred for samples containing $>$1% in solution (Figure 6.6). Addition of KI did not induce homogenization of the Br but rather formed aggregates that were Br-rich relative to the I/Br sample (Figure 6.7).

To understand the effects of Br segregation on the short-lived carrier recombination

dynamics of the perovskite films, we compared transient absorption microscopy (TAM) images to the n-XRFmaps (Figure 6.8). The OSt I/Br sample showed a large range of TAM dynamics, ranging from short to long-lived decays(Figure 6.8), whereas samples with added CsI and/or RbI showed much narrower distributions, as expected from the maps in Figure 6.8 A-D. Quantification of the n-XRF and TAM distributions provided corroborating evidence of reduced elemental and electronic heterogeneity in samples with alkali metal ion incorporation.

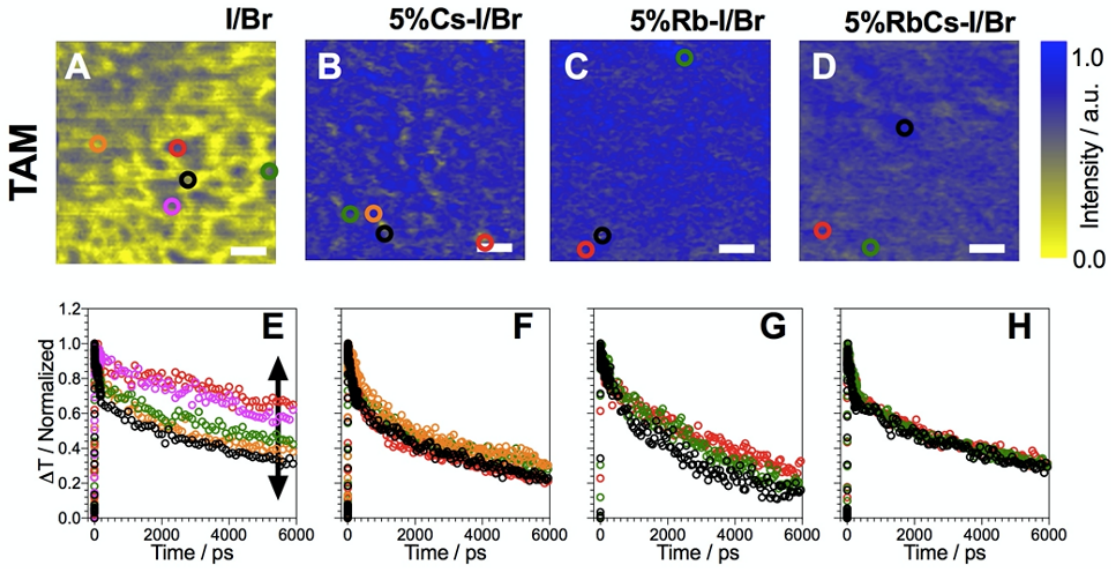

Figure 6.8. Charge carrier dynamics as measured by transient absorption microscopy (TAM). (A-D), the relative change in TA signal $[\delta T(0ps) - \delta T(5ns)]/\delta T(0ps)$ is mapped as function of sample location. The pump wavelength is at 700 nm with a pump fluence of 10 $\mu J/cm^2$. The corresponding time resolved traces below each TAM panel show carrier dynamics taken at positions as indicated. The perovskites studied are: MAFA (A, E), 5% CsMAFA (B, F), 5% RbMAFA (C, G) and 5% Cs 5% RbMAFA (D, H). All scale bars are 1 μm. Note: The maps seen here were prepared in the same batch on different substrates, and the n-XRF results show the same trends in halide homogenization with alkali-metal addition when compared to those shown in Figure 6.5A-D.

We analyzed St and SSt preparations and detected Br-rich cluster areas (Figure 6.5, F to M). Although the Br-rich clusters were difficult to recognize visually, the St and SSt samples without CsI and RbI addition exhibited Br-rich cluster area ratios of 0.08 and 0.13, respectively (Figure 6.5, O and P). Similar to the OSt samples, however, the St and SSt analogs benefited

from the addition of CsI, yielding small Br-rich area ratios of 0.01 and 0.003, respectively. Br-rich aggregates were formed with the addition of RbI alone in both St and SSt. A slight homogenization of Br was observed upon addition of RbI and CsI, yielding a smaller Br-rich area ratio of 0.07 for the St films. Similar to the St conditions, samples prepared in SSt conditions yielded identical trends of Br distribution upon alkali metal halide addition. These SSt materials yielded higher V_{OC} values and lower photocurrents than the St and OSt samples.[134, 234]. We attribute the higher V_{OC} to the homogenization of Br, which reduced recombination-active areas. The lower photocurrent has been suggested to be the result of hindered charge extraction at the charge-selective contact and perovskite interface.[134]. These mea- surements confirmed the importance of addition of CsI and/or RbI for halide homogenization.

6.4 Detection of Alkaline-Rich Clusters

Several recent reports show that adding Rb and Cs yields higher stabilized efficiencies,[11, 231] and solid-state nuclear magnetic resonance experiments have provided some evidence that Rb and K are not incorporated into the lattice of the perovskite structure.[41] We used n-XRF to map the Rb and K concentration and distribution within the perovskite absorbers in fully functional devices (Figure 6.9) with Ost, St, and SSt perovskites. Evaluation of the Cs elemental distribution is challenging in the I-containing perovskites because of the overlapping Cs_L and I_L XRF emission lines. We measured the Rb XRF signal (Figure 6.9, A to C) for all Rb-I/Br samples; all showed large clusters of Rb, with varying sizes and distributions depending on the stoichiometry of the perovskite solution. Loading as little as 1% Rb into the perovskite precursor caused segregation of highly concentrated Rb clusters, and with a further increase in the Rb concentration, large aggregates appeared (Figure 6.10, A to C).

By introducing Cs (forming the composition RbCs-I/Br), the Rb aggregates changed from large precipitates to rodlike structures of lower density, especially for the St and SSt samples. Similarly, K-I/Br perovskite samples [deposited as thin films on fluorine-doped tin

oxide (FTO) glass] containing varying amounts of KI showed aggregates of high concentration of K at a concentration of 5%, and needle-like structures at a concentration of 10% (Figure 6.10). Although some of the K and Rb may be incorporated into the film homogeneously and below the n-XRF bulk detection limits [232, 41] either as constituent atoms or passivants,[235] we observed an appreciable amount of the K and Rb agglomerates in large clusters.

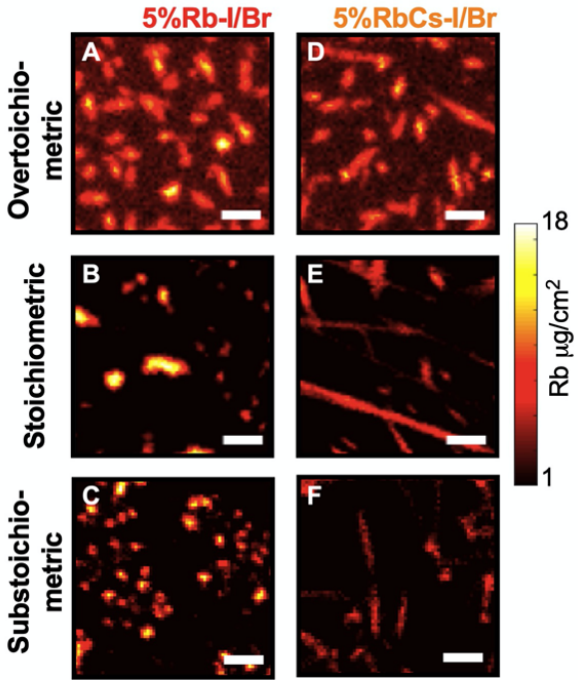

Figure 6.9. Elemental distribution of Rb in perovskites of different compositions. (A to C) Rb XRF maps of the 5% Rb–added samples with different stoichiometries. (D to F) Rb XRF maps of the 5% Rb and 5% Cs–added samples with different stoichiometries. Scale bar, 5 μm.

6.5 Reduced Current Collection at Regions with Alkaline-Rich clusters

To reveal the electronic role of these large aggregates of alkali metals in the Rb-I/Br samples, we conducted n-XRF/x-ray beam–induced current (XBIC) measurements for the devices containing different RbI concentrations (Figure 6.11). The in situ measurement of n-XRF/XBIC suggests that these Rb aggregates suppressed charge collection in the 5% Rb-I/Br

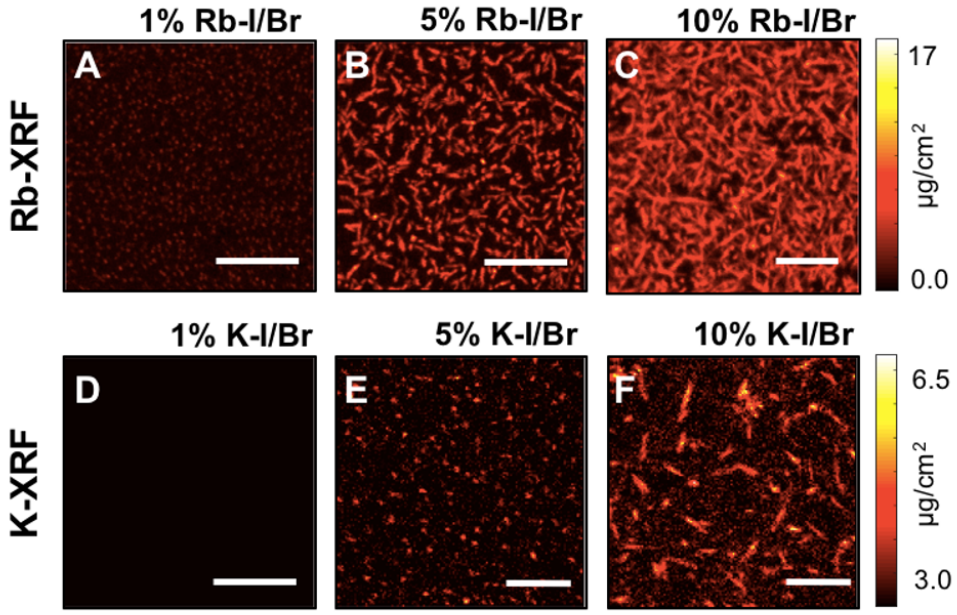

Figure 6.10. Elemental distribution of Rb and K.(A to C) Rb XRF maps of the RbI-added samples with 1%Rb, 5%Rb, and 10%Rb to I/Br perovskite. (D to F) K XRF maps of KI-added samples with different KI loadings in I/Br perovskites. These samples were deposited on FTO glass substrates as opposed to mesoporous TiO_2, which is the substrate for devices. The length of scale bar is 5 μm. No considerable signal was detected for samples containing 1% KI, which we attribute to the detection limits of the low-energy K X-ray fluorescence.

device. However, because the XBIC showed relatively poor signal-to-noise ratio, we performed electron beam–induced current (EBIC) measurements, which provided improved images. The plan-view EBIC profile of the Rb-I/Br sample (Figure 6.12A) was collected and used to create fiducial markers by focused ion beam (FIB) for subsequent n-XRF investigation (Figure 6.12B).

Two distinct regions, one of lower EBIC and one of higher EBIC, are marked in Figure 6.12A. In the corresponding Rb XRF map (Figure 6.12B), the dark circles are the FIB markers. To assess the correlation between Rb distribution and local carrier collection, we divided the EBIC map and the normalized Rb elemental map into 10 $\times$ 10 boxes; Figure 6.12C is a plot of the average value within each box of the EBIC current *versus* the corresponding local average Rb concentration. Figure 6.12C displays a negative correlation (r^2 = 0.6) between charge collection and local Rb concentration, suggesting a detrimental effect from the Rb clusters.

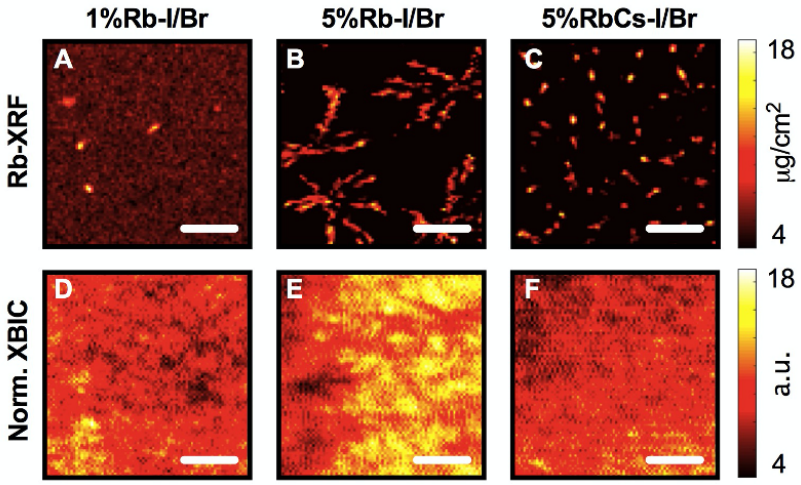

Figure 6.11. Elemental distribution of Rb and its electronic role in charge collection. (A to C) Rb XRF maps of the alkali-added samples (1%Rb, 5%Rb, and 5%RbCs). (D to F) Normalized simultaneously collected in-situ X-ray-beam-induced current (XBIC) mapping while collecting the Rb XRF maps. The length of scale bar is 5 μm.

Current suppression in EBIC has several possible origins, including low carrier generation, current blocking, and carrier recombination- active sites. The correlative study allowed us to compare the Rb aggregate size and its current collection profile directly to evaluate whether the aggregates were recombination-active. The low-EBIC features in Figure 6.12A were broader than the Rb ones in XRF. Broadening can be caused by a larger size of the carrier generation volume under the electron beam excitation relative to the n-XRF probe, by carrier diffusion away from this generation volume followed by recombination of free carriers near or at the Rb clusters, or by both effects. If the Rb aggregates were only charge-blocking and recombination-inactive, then we would expect the EBIC maps to correspond with the Rb n-XRF maps once we accounted for the smearing caused by a large carrier generation volume in EBIC. We modeled electron beam broadening by convoluting the Rb elemental distribution map with a simulated carrier generation profile under the electron beam [simulated using CASINO [236]; see supplementary materials in Chapter 6.6 and Figure 6.13, A and C, for details, beam profile, and simulated map].

Alternatively, if the Rb aggregates were recombination-active, then their interfaces would act as a sink for diffusing excited carriers, and we would need to account for carrier diffusion to

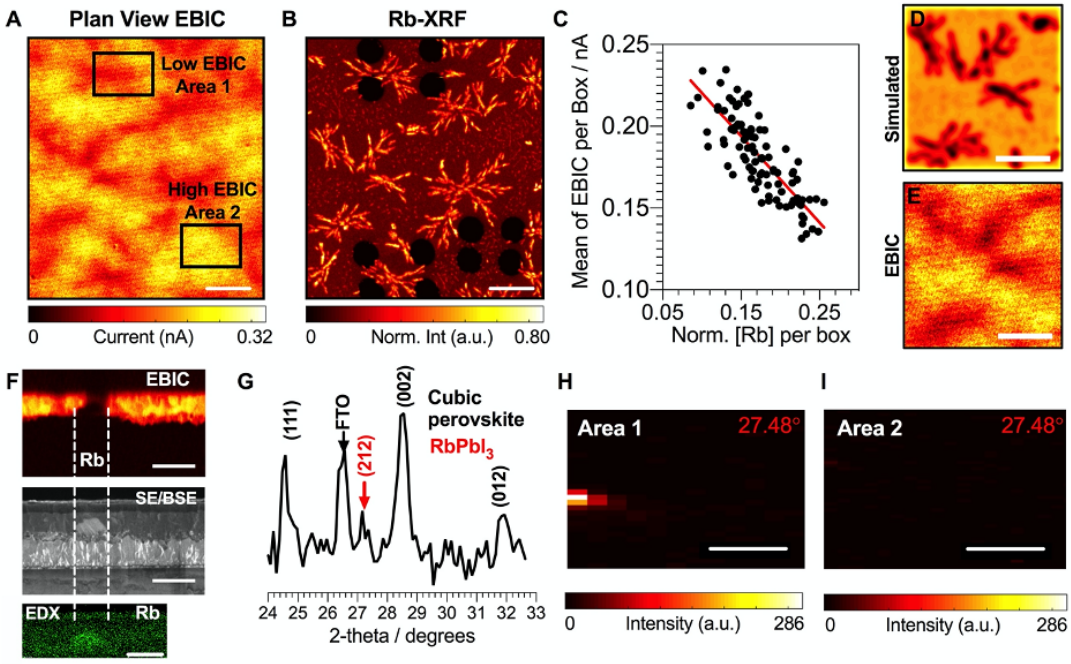

Figure 6.12. The chemical nature and the electronic properties of Rb aggregates in OSt perovskites.(A and B) Plan-view EBIC profile (A) and the correlated Rb-XRF map (B) of the 5%Rb-I/Br perovskite device. Three regions are marked with focused ion beam (FIB). Area 1 and area 2 are the low- and high-EBIC regions, respectively. Scale bars, 10 μm. (C) Scatterplot between Rb concentration and its effect on EBIC charge collection. The individual data points are produced by taking the average within 10 $\times$ 10 square pixel boxes in (B). (D) The Rb XRF map convoluted with the beam generation profile and a Gaussian diffusion broadening of 600 nm. (E) The corresponding EBIC profile of the selected Rb XRF maps. Scale bars, 5 μm. (F) An x-ray diffraction pattern taken at 8 keV with 50 μm spot size in the area within the whole region shown in (A). (G and H) The scanning x-ray Bragg diffraction microscopy map for areas 1 and 2 taken at the $RbPbI_3$ Bragg condition where $2\Theta = 27.48°$. Scale bars, 5 μm. (I) Cross-section EBIC, simultaneously collected SE/BSE, and corresponding EDX. Scale bars, 1 μm.

the aggregates. To model broadening caused by free carrier diffusion and recombination, we further convoluted the beam-broadened Rb map with a Gaussian diffusion profile with a diffusion length of 600 nm. Upon addition of this simulated charge carrier diffusion (Figure 6.12D), the broadening of the signal approached that of the EBIC (Figure 6.12E).

As a further illustration of the importance of accounting for carrier diffusion to the Rb aggregates, a randomly selected line profile is highlighted in Figure 6.14, A and B (blue dotted line). Modeled beam- and diffusion-broadened line profiles were plotted against the n-XRF and

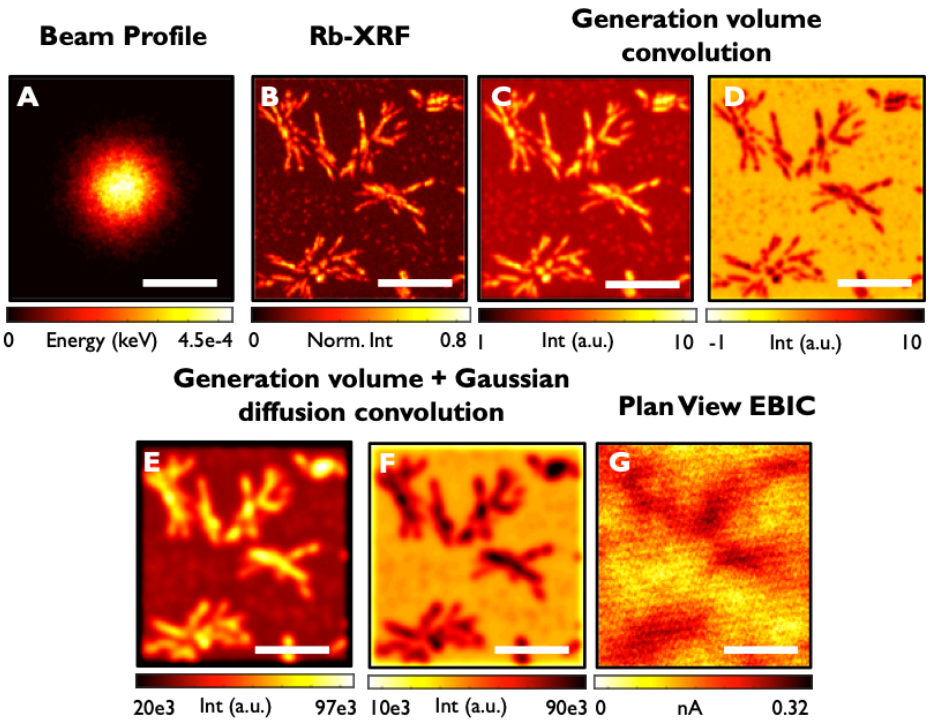

Figure 6.13. The effect of electron beam and diffusion broadening on Rb clusters. (A) Simulated profile of energy deposited in the perovskite layer by a 10 keV beam penetrating the Au and HTL layers of the device. The length of scale bar is 500 nm. (B) The Rb XRF map of the 5%Rb-I/Br sample. (C and D) The profiles of the generation volume convoluted Rb XRF maps with the simulated electron beam profile, in which D is shown in reverse color scale. (E and F) The profiles of the Rb XRF maps with generation volume and Gaussion diffusion broadening with diffusion length of 600 nm, in which F is shown in reverse color scale. (G) The corresponding EBIC profile of the selected Rb XRF maps. The length of scale bar in B to G is 5 μm.

EBIC profiles (Figure 6.14C). Comparison of the profiles indicated that although strong contrast at the n-XRF Rb features was maintained by convolution with the beam profile, this contrast was smeared out by convolution with the diffusion profile. This smearing was observed in the actual EBIC profile, indicating that carrier diffusion was critical to explaining the low-EBIC areas corresponding to Rb-rich aggregates. (See Figure 6.15 for quantification of the induced current loss from EBIC-poor regions related to the Rb aggregates.)

To understand the crystal structure of the Rb clusters, we used a synchrotron-based nano-diffraction technique to enable detection of the secondary phase locally (Figure 6.12F).

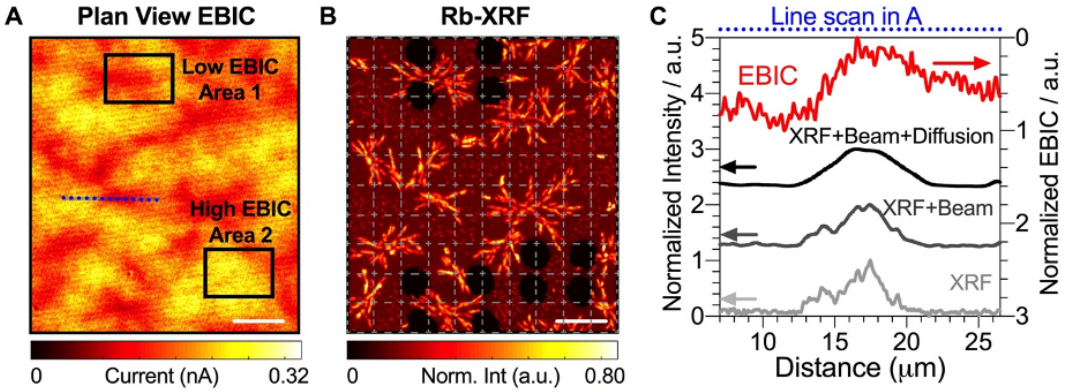

Figure 6.14. (A) Plan view EBIC profile and (B) the correlated Rb-XRF map of 5%Rb-I/Br perovskite device. Three regions are marked with focused ion beam (FIB). Area 1 and Area 2 is the low and high EBIC region respectively. Length of the scale bar is 10 μm. (C) Displays four different line profiles. The XRF and EBIC profiles are obtained from (A) and (B). The other two profiles, XRF + Beam and XRF + Beam + Diffusion, are simulated by convoluting the XRF profile with the E-beam FWHM of 400 nm and a 600 nm diffusion length.

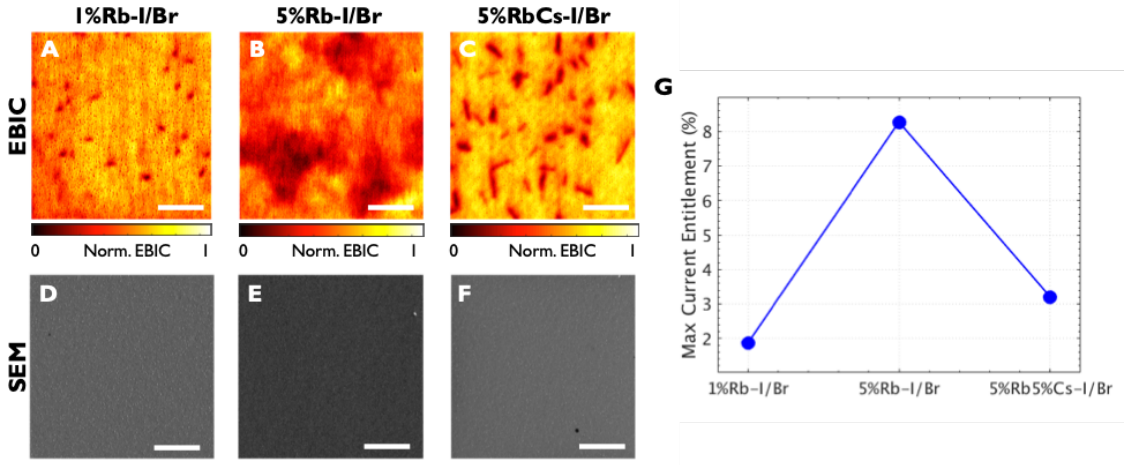

Figure 6.15. The EBIC current is adversely affected by Rb aggregates as seen in EBIC maps of the (A) 1%Rb-I/Br, (B) 5%Rb-I/Br, and (C) 5% RbCs-I/Br samples. Corresponding SEM images in for each sample are shown in (D-F). SEM reveals no pinholes or systematic variations in morphology.

(See Figure 6.16 for XRD of other possible precursor phases and Rb perovskites.) The small peak at 27.48° belongs to the $RbPbI_3$ phase. Scanning x-ray Bragg diffraction microscopy (SXDM; beam spot size ∼150 nm) was then used to map the low- and high- EBIC regions

at the $RbPbI_3$ Bragg angle ($2\theta = 27.48°$) to understand the spatial distribution of this phase (Figure 6.12, G and H). With this nano-diffraction setup, the (212) $RbPbI_3$ crystal planes must be oriented out of plane to be detectable. Although only part of the Rb clusters met this criterion and diffracted in area 1, the SXDM maps exhibited the presence of the secondary phase $RbPbI_3$ in the Rb-rich aggregates, whereas no $RbPbI_3$ diffraction was detected in the high-EBIC area 2. Cross-sectional EBIC (Figure 6.12I) and the corresponding secondary electron/ backscattered electron microscopy (SE/BSE) and energy-dispersive x-ray spectroscopy (EDX) images suggested that Rb aggregates likely nucleated and formed near the TiO_2 interface, and that the aggregate itself was EBIC-inactive and current-blocking.

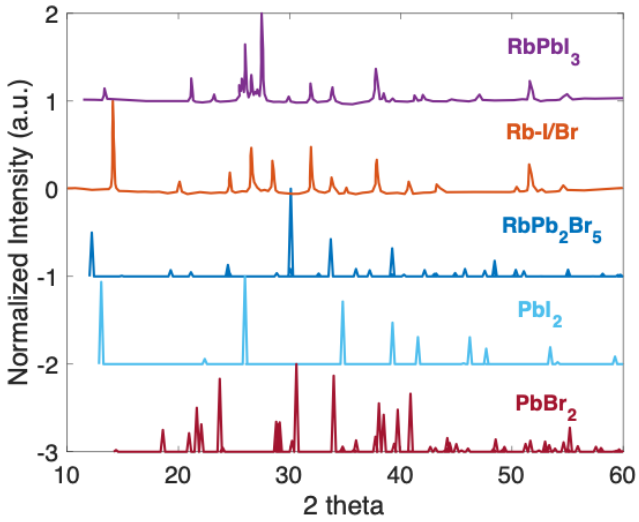

Figure 6.16. The RbPbI3 and Rb containing perovskite phases are obtained from report published by Saliba *et al.*.[12] The $RbPb_2Br_5$ phase is plotted with pattern number: 96-101-0212. PbI_2 and $PbBr_2$ has pattern number, 96-101-0063 and 96-101-0620.

Together, these data suggest that Rb aggregates were optoelectronically inactive, current-blocking, possibly recombination-active, and detrimental to device performance. Thus, all of the samples showed room for improved performance by addressing alkali-rich precipitates, with the largest potential current gains available in the samples with 5% Rb-I/Br (8% relative; FIgure 6.15). Note that this detrimental impact occurs in parallel to any advantageous effect on halide

homogenization caused by RbI and CsI addition. This work helps to elucidate the limitations of adding these alkali metal halides.

6.6 Supporting Information

Device Fabrication. The patterned-F-doped SnO2 (FTO, Pilkington, TEC8) substrates were cleaned by sonicating sequentially in 2% Hellmanex detergent in water, ethyl alcohol and acetone. A dense electron selective layer of TiO_2 (bl-TiO_2,$\sim$50 nm in thickness) was deposited onto a cleaned substrate by spray pyrolysis, using a 20 mM titanium diisopropoxide bis(acetylacetonate) solution (Aldrich) at 450°C. A mesoporous TiO_2 (meso-TiO_2, Dyesol particle size: about 30 nm, crystalline phase: anatase) film was spin-coated onto the bl-TiO_2/FTO substrate using a diluted TiO_2 paste (5:3 paste:ethanol), followed by calcining at 500°C for 1 h in air to remove organic components.

The perovskite films were deposited from a precursor solution containing FAI (1 M, Dyesol), PbI_2 (1.1 M, TCI Chemicals), MABr (0.2 M, Dyesol) and $PbBr_2$ (0.22 M, TCI Chemicals) in anhydrous DMF:DMSO 9:1 (v : v, Acros). All the final precursor solutions had the following concentrations: [$PbBr_2$] = 0.22 M (TCI Chemicals), [PbI_2] = 1.04 M (TCI Chemicals), [MABr] = [$PbBr_2$] = 0.22 M. To probe the importance of the stoichiometry, the ratio of the organics to the lead halides were varied. Over-stoichiometric compositions have an excess of 10 % PbI_2/$PbBr_2$ with respect to FAI/MABr, which is prepared with a [FAI]:[PbI_2] of 0.9 and [MABr]:[$PbBr_2$] of 0.9. Analogously, the substoichiometric films were prepared with 10% lead halide deficiency, meaning that [FAI]:[PbI_2] was 1.1 and [MABr]:[$PbBr_2$] of 1.1. The over-stoichiometric composition thus means a 10% surplus of $PbBr_2$ and PbI_2 in the solution (or a deficiency of FA), which results in excess PbI_2 in the perovskite films.

The alkali-metal iodides were added as CsI, RbI, and KI, in molar ratios of the alkali-metal to lead, ranging from 1% to 10%, as these are widely reported concentrations in the literature. Table 6.1 below shows the compositions used in this work.

The perovskite solution was spin-coated in a two-step program; first at 1000 for 10 s and then at 6000 rpm for 30 s. During the second step, 200 μL of chlorobenzene were poured on the spinning substrate 15 s prior the end of the program. The substrates were then annealed at 100°C for 1 h in a nitrogen filled glove box. The spiro-OMeTAD (Merck) solution (70 mM in chlorobenzene) was spun at 4000 rpm for 20 s. The spiro-OMeTAD was doped at a molar ratio of 0.5, 0.03 and 3.3 with bis(trifluoromethylsulfonyl)imide lithium salt (Li-TFSI, Sigma Aldrich), tris(2-(1H-pyrazol-1-yl)-4-tert-butylpyridine)-cobalt(III) tris(bis(trifluoromethylsulfonyl)imide) (FK209, Dyenamo) and 4-tert-Butylpyridine (TBP, Sigma Aldrich), respectively. Finally, a 100 nm Au top electrode was deposited by thermal evaporation. The active area of this electrode was fixed at 0.16 cm^2.

General Characterization. Grazing incidence X-ray diffraction was performed using a Rigaku SmartLab Diffractometer. Pawley refinements of all compounds were performed using Highscore Plus version 4. The cross-sectional images were investigated by a Zeiss Merlin field-emission scanning electron microscopy (FESEM, Zeiss). Time-resolved photoluminescence measurements were obtained by time-correlated single photon counting (TCSPC). The sample was excited by a pulsed 405 nm wavelength laser (PicoQuant LDH-P-FA-530-B) and the laser power was adjusted by a neutral density filter wheel to obtain a $<5\%$ count rate in each measurement to avoid pile-up artifacts in the detector. The repetition rate was set to 200 kHz for Rb, K and 100 kHz for Cs. The emission was collected by parabolic mirrors and focused onto a silicon single-photon avalanche photodiode (Micro Photon Devices PD-100-C0C) and photon arrival times were recorded using a PicoHarp 300 (PicoQuant) using an integration time of 300 s. Excess laser scatter was removed by a 532 notch filter (Chroma Technology Corp.) and a 550 nm long-pass filter (ThorLabs).

n-XRF Characterization. To obtain quantitative elemental distributions in the perovskite films, functional hybrid perovskite solar cells were investigated by means of synchrotron-based

nanoprobe X-ray fluorescence (n-XRF) with a 250 nm full-width half-maximum (FWHM) focused beam at 16.3 keV at beamline 2-IDD in a helium environment of the Advanced Photon Source (APS) at Argonne National Laboratory. The n-XRF measurement was conducted with the backside Au contact facing the incident X-ray beam, with a full fluorescence spectrum collected point-by-point during mapping. The MAPS software was used to fit and deconvolute overlapping peaks and the background from the fluorescence data.[99] The stoichiometry of Br:Pb in the absorbers was then quantified using a thin film methylammonium lead bromide single crystal as a reference.

SXDM Characterization. The SXDM (scanning X-ray Bragg diffraction mapping) was conducted using Hard X-ray Nanoprobe (HXN) of the Center for Nanoscale Materials (CNM) at sector 26-IDC of the Advanced Photon Source (APS) at Argonne National Laboratory. SXDM used a focused beam with Bragg diffraction geometry and rastered the X-ray beam across the sample with the scattering recorded on a single-photon counting pixel-array detector (Medipix) at every point. Measurements were taken in vacuum environment ($< 5 \times 10^4$ torr). A Fresnel zone plate (Xradia Inc., 133-μm diameter gold pattern, 24-nm outer zone, 300-nm thickness) focused the monochromatic incident X-ray beam (photon energy 8 keV, λ = 1.55Å) onto the sample and was positioned at slight defocus to match the beam size of the n-XRF characterization. The perovskite sample was mapped with 200 nm stepsize. To image the scattered intensity from the $RbPbI_3$ phase, the sample was positioned to bring the (212) $RbPbI_3$ Bragg diffraction on the detector, which was centered at $2\theta = 27.48^\circ$ (λ = 1.55Å). The scattering intensity is integrated from 26.98° to 27.98°.

Transient absorption imaging. The transient absorption images and dynamics were acquired by a home-built, femtosecond transient absorption spectroscopy setup. The output of a high repetition rate amplifier (PHAROS Light Conversion Ltd., FWHM = 200 fs, 400 kHz repetition rate, pulse energy of 100 μJ, 1030 nm fundamental) was used to feed two independent

optical parametric amplifiers (OPA, TOPAS-Twins, Light Conversion Ltd) to generate the pump beam (700 nm) and probe beam (755 nm). An acousto-optic modulator (Gooch and Housego, R23080-1) was used to modulate the pump beam at 100 kHz. A mechanical translation stage (Thorlabs, DDS600-E) was used to delay the probe with respect to the pump. Both the pump and probe beams were focused onto the sample by an oil immersion objective (CFI Apo TIRF, Nikon Inc., 60x, NA 1.49). With the pump beam being filtered out, the probe beam was collected by another objective (Nikon, S Plan Fluor ELWD 20x, NA 0.45) and was detected by an avalanche photodiode (APD; Hamamatsu, C5331-04). The change in the probe transmission (δT) induced by the pump was detected by a lock-in amplifier. A pair of Galvanometer mirrors (Thorlabs GVS012) was used to scan the probe beam and pump beam together in space to obtain the transient signal mapping. To construct Figures 6.8 A-D, we plot the difference between transient bleach signal at time zero (0 ns time delay, $\delta T0$) and that after a 5 ns time delay ($\delta T5$) is compared to the signal arising from the initially generated carriers at time zero.

In-situ n-XRF/XBIC Characterization. The *in-situ* n-XRF and XBIC (X-ray beam induced current) characterization was conducted using a similar setup as previous studies,[196] where the X-ray beam penetrates through the backside Au metal contact, allowing collection of both elemental distribution (XRF) and photocurrent (XBIC) simultaneously, with 250 nm step size and a dwell time per point of 50 ms. A lock-in current pre-amplifier at the beamline was used to collect the induced current signal for XBIC. To improve the signal-to-noise of the element XRF map further, a second "elemental" map was collected using a step size as small as 150 nm (oversampling) with the same amount of dwell time. The Rb incorporation was quantified using a RbI_2 Micromatter standard with known loading concentration of 6.2 $\mu g/cm^2$.

EBIC Characterization

The electron beam induced current (EBIC) was collected using an FEI Scios Dual Beam microscope with a Mighty EBIC 2.0 controller (Ephemeron Labs) and a Femto DLPCA-200

pre-amplifier.

Planar Configuration: Similar to XBIC measurements, the e-beam was rastered across the sample through the backside Au metal contact and the generated carriers were collected via the front/back contacts, Au and FTO. The accelerating voltage and current were 10 kV and 13 pA, respectively. The 10 kV accelerating voltage was chosen in order to allow electrons to penetrate the top contact and reach the perovskite layer. A beam current of 13 pA ensured that damage was minimized and injection was kept low. The pixel size varied between 21 nm and 84 nm depending on the magnification used, and the dwell time was 26.5 μs. EBIC and SEM images of the same region of interest were collected simultaneously as shown in Figure 6.15. The EBIC maps are normalized to the maximum current in each individual map, allowing cross-sample comparison for samples with different Rb loading. The comparison between EBIC and SEM further indicates that the variation shown in EBIC maps is not due to surface morphology nor pinholes. We observed an activation effect that depended on total electron dose. The total EBIC signal increased over several scans, before decreasing due to damage. However, the features observed in our images were not dose-dependent.

Cross-Section Configuration: For cross-section EBIC measurements, the sample was scribed by a diamond-wheel type glass cutter on the glass side. The sample was then cleaved by applying pressure on the device-side above the cleave with a diamond pen. The mechanically cleaved samples were then immediately loaded into the EBIC system. Imaging was performed in FEI Optiplan mode using the T2 (in-lens like) detector, at 3 kV and 1.6 pA. The pixel size and dwell time were 5.6 nm and 26.5 μs, respectively. We did not observe the same activation effect as in planar measurements, possible due to increased energy deposition under these conditions. We would like to stress that interpretation of cross-section EBIC measurements with mechanically cleaved devices must be done with care. The mechanical break leaves morphological artifacts that must be ruled out in the analysis. In order to obtain the reported result in Figure 6.12I in the main text, we established that the effect was repeatable and reliable regardless of the cross-section morphology at the Rb cluster.

CASINO Electron Beam Profile Modeling. We modeled the profile of energy deposited by the electron beam by Monte-Carlo simulation using the CASINO software. The energy deposited is directly proportional to the number of free carriers generated by the electron beam. We constructed a model consisting of a gold top layer, carbon middle layer to simulate the HTL, and perovskite bottom layer. A 10 keV beam impinged perpendicular to the layer structure. A matrix of gold and HTL thicknesses were tested to assess variability in the profile due to sample variation. As the Au and HTL layers generate negligible EBIC current (as verified from cross-section measurements), we considered only the energy deposited in the perovskite layer. As EBIC images are a 2D projection of a 3D process, we projected the 3D beam profile in the perovskite layer onto the plane parallel to the layer. This produced the beam profile shown in Figure 6.13a. Within the range of Au thicknesses of 80$\pm$10 nm and HTL thicknesses of 200$\pm$20 nm, this beam profile has a full-width-half-maximum of $\sim$400 nm, without much variation with contact thickness.

Transmission Electron Microscopy and Focused Ion Beam Sample Preparation.

Transmission electron microscopy (TEM) images were taken with a FEI 200 kV Sphera Microscope. Samples for TEM were prepared by focused ion beam (FEI Scios DualBeam FIB/SEM). The FIB-TEM sample preparation follows a previously reported procedure.[237]

6.7 Acknowledgement

Chapter 6, in full, is a reprint of the material ”Homogenized halides and alkali cation segregation in alloyed organic-inorganic perovskites”, Juan-Pablo Correa-Baena1, Yanqi Luo, Thomas M. Brenner, Jordan Snaider, Shijing Sun, Xueying Li, Mallory A. Jensen, Noor Titan Putri Hartono, Lea Nienhaus, Sarah Wieghold, Jeremy R. Poindexter, Shen Wang, Ying Shirley Meng, Ti Wang, Barry Lai, Martin V. Holt, Zhonghou Cai, Moungi G. Bawendi, Libai Huang,

Tonio Buonassisi, David P. Fenning. The dissertation author was one of the primary investigators and author of this material.

Chapter 7

Conclusion

This thesis consists of both technical and scientific contributions. The technical contribution is mostly present in Chapter 2 on establishing the optimal operating window for X-ray and E-beam microscopy characterization given the beam sensitive nature of halide perovskites. With the quantitative specification, it allowed the collection of the first successful elemental and electronic maps using synchrotron based X-ray microscopy.

Utilizing the powerful synchrotron nanoprobe, heterogeneous elemental distribution was revealed in mixed halides Br/I perovskite absorbers as shown in Chapter 3. The spatially segregated halide can be attributed to the difficulty in homogenized mixing due to ionic radii difference, or the halide instability and highly mobile nature in the methylammonium based system shown in Chapter 4. To avoid these problems, we originally suspected that perovskite absorbers without the unstable ions such as Br and MA with chemistry of $FA_{0.9}Cs_{0.1}PbI_3$ could result in more stable performance than the MA-based ones. With the A-site modulation, $FA_{0.9}Cs_{0.1}PbI_3$ absorbers yielded high device performance but were hindered by A-site instability. This was evidenced by the Cs-rich clusters observed after 600 hrs of the accelerated testing. These results suggest a balancing act is needed between A- and X- site composition, which leads us to explore one of the most complex absorbers that has mixed A-site (MA, FA, Cs, and Rb) and mixed Br/I systems. In the complex compositions, elemental information from XRF indicates that Cs and/or Rb addition homogenized the halide distribution in the mixed halide chemistry

shown in Chapter 6. Although Rb-rich aggregates are found to reduce current collection in perovskite devices, Cs appears to be incorporated with uniform elemental distribution. The halide homogenization upon alkaline ions addition is believed to be the key for yielding high performance and stable perovskite devices.

Hybrid halide perovskites are considered as a new emerging class of material that associates with lots of interesting physics and unknowns. Additives that enhance average opto-electronic properties may result in a large degree of spatial heterogeneity, which can potentially lead to device instability and poor reproducibility in large area fabrication. To understand the role of the additives or elements, a wide range of perovskite samples with different compositions were studied using correlative synchrotron based X-ray microscopy techniques. Overall, the halide perovskite appears to be a very delicate material and strongly dependent on the given material system. Therefore, careful considerations must be taken prior to modifying any of the A-site and halide substituents.

With the valuable microscopic characterization, we reveal that the $FA_{1-x}Cs_xPbI_3$ perovskite is metastable as fabricated but become unstable upon stress testing. Recent progress in perovskite community demonstrates that Cs containing triple cations (CsFAMA) devices have shown respectful stability with $>$ 1000 hr operational lifetime. Given 25 years of manufacturing warranty for silicon solar cells, the state-of-art stability of perovskite still seems short. To improve stability of the CsFAMA perovskite compositions, further investigation on the degradation modes of perovskites as a function of input energy (heat or light) may allow us to realize the limitations of perovskites upon the accelerated aging test. By obtaining both chemical and electronic information, we can potentially determine phase segregation initiation energy requirements or conditions, as well as its impact on carrier recombination dynamics. Elucidating these deeper insights on light induced degradation may help further improve stability of perovskite solar cells via device or interface engineering.

Bibliography

[1] T. Ma, M. Cagnoni, D. Tadaki, A. Hirano-Iwata, and M. Niwano, "Annealing-induced chemical and structural changes in triiodide and mixed-halide organometal perovskite layers," *J. Mater. Chem. A*, vol. 3, pp. 14195–14201, 2015.

[2] M. Saliba, "Polyelemental, multicomponent perovskite semiconductor libraries through combinatorial screening," *Advanced Energy Materials*, vol. 1803754, pp. 1–8, 2019.

[3] Q. Dong, Y. Fang, Y. Shao, P. Mulligan, J. Qiu, L. Cao, and J. Huang, "Electron-hole diffusion lengths > 175 μm in solution-grown $CH_3NH_3PbI_3$ single crystals," *Science*, vol. 347, pp. 967–970, feb 2015.

[4] D. Shi, V. Adinolfi, R. Comin, M. Yuan, E. Alarousu, A. Buin, Y. Chen, S. Hoogland, A. Rothenberger, K. Katsiev, Y. Losovyj, X. Zhang, P. A. Dowben, O. F. Mohammed, E. H. Sargent, and O. M. Bakr, "Low trap-state density and long carrier diffusion in organolead trihalide perovskite single crystals," *Science*, vol. 347, no. 6221, pp. 519–522, 2015.

[5] B. Yang, O. Dyck, J. Poplawsky, J. Keum, A. Puretzky, S. Das, I. Ivanov, C. Rouleau, G. Duscher, D. Geohegan, and K. Xiao, "Perovskite solar cells with near 100% internal quantum efficiency based on large single crystalline grains and vertical bulk heterojunctions," *Journal of the American Chemical Society*, vol. 137, no. 29, pp. 9210–9213, 2015.

[6] R. Wang, J. Xue, K. L. Wang, Z. K. Wang, Y. Luo, D. Fenning, G. Xu, S. Nuryyeva, T. Huang, Y. Zhao, J. L. Yang, J. Zhu, M. Wang, S. Tan, I. Yavuz, K. N. Houk, and Y. Yang, "Constructive molecular configurations for surface-defect passivation of perovskite photovoltaics," *Science*, vol. 366, no. 6472, pp. 1509–1513, 2019.

[7] National Renewable Energy Laboratory (NREL), "Best research-cell efficiencies," 2019.

[8] H.-S. Kim, C.-R. Lee, J.-H. Im, K.-B. Lee, T. Moehl, A. Marchioro, S.-J. Moon, R. Humphry-Baker, J.-H. Yum, J. E. Moser, M. Grätzel, and N.-G. Park, "Lead iodide perovskite sensitized all-solid-state submicron thin film mesoscopic solar cell with efficiency exceeding 9%," *Scientific Reports*, vol. 2, no. 1, p. 591, 2012.

[9] J. H. Noh, S. H. Im, J. H. Heo, T. N. Mandal, and S. I. Seok, "Chemical management for colorful, efficient, and stable inorganic-organic hybrid nanostructured solar cells," *Nano Letters*, vol. 13, no. 4, pp. 1764–1769, 2013.

[10] G. E. Eperon, S. D. Stranks, C. Menelaou, M. B. Johnston, L. M. Herz, and H. J. Snaith, "Formamidinium lead trihalide: a broadly tunable perovskite for efficient planar heterojunction solar cells," *Energy & Environmental Science*, vol. 7, pp. 982–988, 2014.

[11] M. Saliba, T. Matsui, J.-Y. Seo, K. Domanski, J.-P. Correa-Baena, M. K. Nazeeruddin, S. M. Zakeeruddin, W. Tress, A. Abate, A. Hagfeldt, and M. Grätzel, "Cesium-containing triple cation perovskite solar cells: improved stability, reproducibility and high efficiency," *Energy Environ. Sci.*, vol. 9, no. 6, pp. 1989–1997, 2016.

[12] M. Saliba, T. Matsui, K. Domanski, J.-Y. Seo, A. Ummadisingu, S. M. Zakeeruddin, J.-P. Correa-Baena, W. R. Tress, A. Abate, A. Hagfeldt, and M. Gratzel, "Incorporation of rubidium cations into perovskite solar cells improves photovoltaic performance," *Science*, vol. 354, no. 6309, pp. 206–209, 2016.

[13] H. J. Snaith, A. Abate, J. M. Ball, G. E. Eperon, T. Leijtens, N. K. Noel, S. D. Stranks, J. T. W. Wang, K. Wojciechowski, and W. Zhang, "Anomalous hysteresis in perovskite solar cells," *Journal of Physical Chemistry Letters*, vol. 5, no. 9, pp. 1511–1515, 2014.

[14] W. Tress, N. Marinova, T. Moehl, S. M. Zakeeruddin, N. Mohammad K., M. Grätzel, M. K. Nazeeruddin, and M. Grätzel, "Understanding the rate-dependent J–V hysteresis, slow time component, and aging in CH 3 NH 3 PbI 3 perovskite solar cells: the role of a compensated electric field," *Energy Environ. Sci.*, vol. 8, no. 3, pp. 995–1004, 2015.

[15] E. T. Hoke, D. J. Slotcavage, E. R. Dohner, A. R. Bowring, H. I. Karunadasa, and M. D. McGehee, "Reversible photo-induced trap formation in mixed-halide hybrid perovskites for photovoltaics," *Chemical Science*, vol. 6, pp. 613–617, 2015.

[16] W. S. Yang, J. H. Noh, N. J. Jeon, Y. C. Kim, S. Ryu, J. Seo, and S. I. Seok, "High-performance photovoltaic perovskite layers fabricated through intramolecular exchange," *Science*, vol. 348, no. 6240, pp. 1234–1237, 2015.

[17] S. D. Stranks and H. J. Snaith, "Metal-halide perovskites for photovoltaic and light-emitting devices," *Nature Nanotechnology*, vol. 10, no. 5, pp. 391–402, 2015.

[18] J. Berry, T. Buonassisi, D. A. Egger, G. Hodes, L. Kronik, Y. L. Loo, I. Lubomirsky, S. R. Marder, Y. Mastai, J. S. Miller, D. B. Mitzi, Y. Paz, A. M. Rappe, I. Riess, B. Rybtchinski, O. Stafsudd, V. Stevanovic, M. F. Toney, D. Zitoun, A. Kahn, D. Ginley, and D. Cahen, "Hybrid organic-inorganic perovskites (HOIPs): opportunities and challenges," *Advanced Materials*, vol. 27, no. 35, pp. 5102–5112, 2015.

[19] M. a. Green, A. Ho-Baillie, and H. J. Snaith, "The emergence of perovskite solar cells," *Nature Photonics*, vol. 8, no. 7, pp. 506–514, 2014.

[20] B. Saparov and D. B. Mitzi, "Organic-Inorganic Perovskites: Structural Versatility for Functional Materials Design," *Chemical Reviews*, vol. 116, no. 7, pp. 4558–4596, 2016.

[21] Y. B. Nian, J. Strozier, N. J. Wu, X. Chen, and A. Ignatiev, "Evidence for an oxygen diffusion model for the electric pulse induced resistance change effect in transition-metal oxides," *Physical Review Letters*, vol. 98, no. 14, pp. 3–6, 2007.

[22] M. Cherry, M. Islam, and C. Catlow, "Oxygen ion migration in perovskite-type oxides," 1995.

[23] A. Kojima, K. Teshima, Y. Shirai, and T. Miyasaka, "Organometal halide perovskites as visible-light sensitizers for photovoltaic cells," *Journal of the American Chemical Society*, vol. 131, no. 17, pp. 6050–6051, 2009.

[24] H. Zhou, Q. Chen, G. Li, S. Luo, T.-b. Song, H.-S. Duan, Z. Hong, J. You, Y. Liu, and Y. Yang, "Interface engineering of highly efficient perovskite solar cells," *Science*, vol. 345, no. 6196, pp. 542–547, 2013.

[25] A. Barrows, A. Pearson, C. Kwak, A. Dunbar, A. Buckley, and D. Lidzey, "Efficient planar heterojunction mixed-halide perovskite solar cells deposited via spray-deposition," *Energy & Environmental Science*, vol. 7, pp. 2944–2950, 2014.

[26] Y. Luo, F. A. Santos, T. W. Wagner, E. Tsoi, and S. Zhang, "Dynamic interactions between poly(3-hexylthiophene) and single-walled carbon nanotubes in marginal solvent," *Journal of Physical Chemistry B*, vol. 118, no. 22, pp. 6038–6046, 2014.

[27] J. Tilchin, D. N. Dirin, G. I. Maikov, A. Sashchiuk, M. V. Kovalenko, and E. Lifshitz, "Hydrogen-like wannier-mott excitons in single crystal of methylammonium lead bromide perovskite," *ACS Nano*, vol. 10, no. 6, pp. 6363–6371, 2016.

[28] K. Tanaka and T. Kondo, "Bandgap and exciton binding energies in lead-iodide-based natural quantum-well crystals," *Science and Technology of Advanced Materials*, vol. 4, no. 6, pp. 599–604, 2003.

[29] C. R. Kagan, "Organic-Inorganic Hybrid Materials as Semiconducting Channels in Thin-Film Field-Effect Transistors," *Science*, vol. 286, no. 5441, pp. 945–947, 1999.

[30] D. Mitzi, C. Feild, Z. Schlesinger, and R. Laibowitz, "Transport, Optical, and Magnetic Properties of the Conducting Halide Perovskite $CH_3NH_3SnI_3$," *Journal of Solid State Chemistry*, vol. 114, no. 1, pp. 159–163, 1995.

[31] J. Tong, Z. Song, D. H. Kim, X. Chen, C. Chen, A. F. Palmstrom, P. F. Ndione, M. O. Reese, S. P. Dunfield, O. G. Reid, J. Liu, F. Zhang, S. P. Harvey, Z. Li, S. T. Christensen, G. Teeter, D. Zhao, M. M. Al-Jassim, M. F. Van Hest, M. C. Beard, S. E. Shaheen, J. J. Berry, Y. Yan, and K. Zhu, "Carrier lifetimes of >1 μs in Sn-Pb perovskites enable efficient all-perovskite tandem solar cells," *Science*, vol. 364, no. 6439, pp. 475–479, 2019.

[32] R. Prasanna, T. Leijtens, S. P. Dunfield, J. A. Raiford, E. J. Wolf, S. A. Swifter, J. Werner, G. E. Eperon, C. de Paula, A. F. Palmstrom, C. C. Boyd, M. F. A. M. van Hest, S. F.

Bent, G. Teeter, J. J. Berry, and M. D. McGehee, "Design of low bandgap tin–lead halide perovskite solar cells to achieve thermal, atmospheric and operational stability," *Nature Energy*, 2019.

[33] V. M. Goldschmidt, "Die Gesetze der Krystallochemie," *Die Naturwissenschaften*, vol. 14, no. 21, pp. 477–485, 1926.

[34] G. Kieslich, S. Sun, and A. K. Cheetham, "Solid-state principles applied to organic–inorganic perovskites: new tricks for an old dog," *Chem. Sci.*, vol. 5, no. 12, pp. 4712–4715, 2014.

[35] G. Kieslich, S. Sun, and T. Cheetham, "An extended tolerance factor approach for organic-inorganic perovskites," *Chem. Sci.*, vol. 6, pp. 3430–3433, 2015.

[36] L. Pauling, "The principles determining the structure of complex ionic crystals," *Journal of the American Chemical Society*, vol. 51, no. 4, pp. 1010–1026, 1929.

[37] C. Li, X. Lu, W. Ding, L. Feng, Y. Gao, and Z. Guo, "Formability of ABX 3 (X = F, Cl, Br, I) halide perovskites," *Acta Crystallographica Section B: Structural Science*, vol. 64, no. 6, pp. 702–707, 2008.

[38] C. J. Bartel, C. Sutton, B. R. Goldsmith, R. Ouyang, C. B. Musgrave, L. M. Ghiringhelli, and M. Scheffler, "New tolerance factor to predict the stability of perovskite oxides and halides," *Science Advances*, vol. 5, no. 2, pp. 1–10, 2019.

[39] R. D. Shannon, "Revised effective ionic radii and systematic studies of interatomic distances in halides and chalcogenides," *Acta Crystallographica Section A*, vol. 32, no. 5, pp. 751–767, 1976.

[40] J.-P. Correa-Baena, Y. Luo, T. M. Brenner, J. Snaider, S. Sun, X. Li, M. A. Jensen, N. Titan, P. Hartono, L. Nienhaus, S. Wieghold, J. R. Poindexter, S. Wang, Y. S. Meng, T. Wang, B. Lai, M. V. Holt, Z. Cai, M. G. Bawendi, L. Huang, T. Buonassisi, and D. P. Fenning, "Homogenized halides and alkali cation segregation in alloyed organic-inorganic perovskites," *Science*, vol. 633, no. 6427, pp. 627–631, 2019.

[41] D. J. Kubicki, D. Prochowicz, A. Hofstetter, S. M. Zakeeruddin, M. Grätzel, and L. Emsley, "Phase Segregation in Cs-, Rb- and K-Doped Mixed-Cation $(MA)_x(FA)_{1-x}PbI_3$ Hybrid Perovskites from Solid-State NMR," *Journal of the American Chemical Society*, vol. 139, no. 40, pp. 14173–14180, 2017.

[42] X. Li, J. Yang, Q. Jiang, W. Chu, D. Zhang, Z. Zhou, Y. Ren, and J. Xin, "Enhanced photovoltaic performance and stability in mixed-cation perovskite solar cells via compositional modulation," *Electrochimica Acta*, vol. 247, pp. 460–467, 2017.

[43] R. E. Brandt, V. Stevanović, D. S. Ginley, and T. Buonassisi, "Identifying defect-tolerant semiconductors with high minority-carrier lifetimes: beyond hybrid lead halide perovskites," *MRS Communications*, vol. 5, no. 02, pp. 265–275, 2015.

[44] W.-j. Yin, T. Shi, Y. Yan, W.-j. Yin, T. Shi, and Y. Yan, "Unusual defect physics in CH3NH3PbI3 perovskite solar cell absorber Unusual defect physics in $CH_3NH_3PbI_3$ perovskite solar cell absorber," *Applied Physics Letters*, vol. 104, no. 063903, pp. 1–4, 2014.

[45] W.-J. Yin, T. Shi, and Y. Yan, "Unique Properties of Halide Perovskites as Possible Origins of the Superior Solar Cell Performance," *Advanced Materials*, vol. 26, no. 27, pp. 4653–4658, 2014.

[46] J. H. Heo, D. H. Song, and S. H. Im, "Planar CH 3 NH 3 PbBr 3 Hybrid Solar Cells with 10 . 4 % Power Conversion Effi ciency , Fabricated by Controlled Crystallization in the Spin-Coating Process," *Advanced Materials*, vol. 26, pp. 8179–8183, 2014.

[47] K. Osvald, R. E. Wasylishen, M. A. White, C. T. Stanley, and M. J. M. Van Oort, "Alkylammonium lead halides. Part 2. $CH_3NH_3PbX_3$ (X = C1, Br, I) perovskites: cuboctahedral halide cages with isotropic cation reorientation," *Can. J. Chem*, vol. 68, pp. 412–422, 1990.

[48] D. Solis-Ibarra, I. C. Smith, and H. I. Karunadasa, "Post-synthetic halide conversion and selective halogen capture in hybrid perovskites," *Chem. Sci.*, vol. 6, pp. 4054–4059, 2015.

[49] C. Eames, J. M. Frost, P. R. F. Barnes, B. C. O'Regan, A. Walsh, and M. S. Islam, "Ionic transport in hybrid lead iodide perovskite solar cells," *Nature Communications*, vol. 6, no. May, p. 7497, 2015.

[50] Y.-Y. Zhang, S. Chen, P. Xu, H. Xiang, X.-G. Gong, A. Walsh, and S.-h. Wei, "Intrinsic Instability of the Hybrid Halide Perovskite Semiconductor $CH_3NH_3PbI_3$," *Nature communications*, no. June, p. 11, 2015.

[51] N. J. Jeon, J. H. Noh, Y. C. Kim, W. S. Yang, S. Ryu, and S. I. Seok, "Solvent engineering for high-performance inorganic-organic hybrid perovskite solar cells.," *Nature materials*, vol. 13, no. July, pp. 1–7, 2014.

[52] J. T. Jacobsson, J. P. Correa Baena, M. Pazoki, M. Saliba, K. Schenk, M. Grätzel, and A. Hagfeldt, "Exploration of the compositional space for mixed lead halogen perovskites for high efficiency devices," *Energy Environ. Sci.*, vol. 9, no. 0, pp. 1706–1724, 2016.

[53] J. Li, Q. Dong, N. Li, and L. Wang, "Direct Evidence of Ion Diffusion for the Silver-Electrode-Induced Thermal Degradation of Inverted Perovskite Solar Cells," *Advanced Energy Materials*, no. 1602922, pp. 1–8, 2017.

[54] Y. Luo, P. Khoram, S. Brittman, Z. Zhu, B. Lai, S. P. Ong, E. C. Garnett, and D. P. Fenning, "Direct observation of halide migration and its effect on photoluminescence of methylammonium lead bromide perovskite single crystals," *Advanced Materials*, no. 1703451, pp. 1–7, 2017.

[55] C. Kagan, D. B. Mitzi, and C. D. Dimitrakopoulos, "Organic-Inorganic Hybrid Materials as Semiconductiong Channels in Thin-Film Field-Effect Transistors," *Science*, vol. 286, no. OCTOBER, pp. 945–947, 1999.

[56] N. Wang, L. Cheng, R. Ge, S. Zhang, Y. Miao, W. Zou, C. Yi, Y. Sun, Y. Cao, R. Yang, Y. Wei, Q. Guo, Y. Ke, M. Yu, Y. Jin, Y. Liu, Q. Ding, D. Di, L. Yang, G. Xing, H. Tian, C. Jin, F. Gao, R. H. Friend, J. Wang, and W. Huang, "Perovskite light-emitting diodes based on solution-processed self-organized multiple quantum wells," *Nature Photonics*, vol. 10, no. 11, pp. 699–704, 2016.

[57] M. Yuan, L. N. Quan, R. Comin, G. Walters, R. Sabatini, O. Voznyy, S. Hoogland, Y. Zhao, E. M. Beauregard, P. Kanjanaboos, Z. Lu, D. H. Kim, and E. H. Sargent, "Perovskite energy funnels for efficient light-emitting diodes," *Nature Nanotechnology*, vol. 11, no. 10, pp. 872–877, 2016.

[58] H. Tsai, W. Nie, J.-C. Blancon, C. C. Stoumpos, C. M. M. Soe, J. Yoo, J. Crochet, S. Tretiak, J. Even, A. Sadhanala, G. Azzellino, R. Brenes, P. M. Ajayan, V. Bulovic, S. D. Stranks, R. H. Friend, M. G. Kanatzidis, and A. D. Mohite, "Stable Light-Emitting Diodes Using Phase-Pure Ruddlesden–Popper Layered Perovskites," *Advanced Materials*, vol. 1704217, p. 1704217, 2017.

[59] C. C. Stoumpos, D. H. Cao, D. J. Clark, J. Young, J. M. Rondinelli, J. I. Jang, J. T. Hupp, and M. G. Kanatzidis, "Ruddlesden-Popper Hybrid Lead Iodide Perovskite 2D Homologous Semiconductors," *Chemistry of Materials*, vol. 28, no. 8, pp. 2852–2867, 2016.

[60] Y. Chen, Y. Sun, J. Peng, J. Tang, K. Zheng, and Z. Liang, "2D Ruddlesden-Popper Perovskites for Optoelectronics," *Advanced Materials*, vol. 1703487, pp. 1–15, 2017.

[61] B. E. Cohen, M. Wierzbowska, and L. Etgar, "High efficiency quasi 2D lead bromide perovskite solar cells using various barrier molecules," *Sustainable Energy Fuels*, vol. 1, no. 9, pp. 1935–1943, 2017.

[62] G. Grancini, C. Roldán-Carmona, I. Zimmermann, E. Mosconi, X. Lee, D. Martineau, S. Narbey, F. Oswald, F. De Angelis, M. Graetzel, and M. K. Nazeeruddin, "One-Year stable perovskite solar cells by 2D/3D interface engineering," *Nature Communications*, vol. 8, pp. 1–8, 2017.

[63] J. Zhang, J. Qin, M. Wang, Y. Bai, H. Zou, J. K. Keum, R. Tao, H. Xu, H. Yu, S. Haacke, and B. Hu, "Uniform Permutation of Quasi-2D Perovskites by Vacuum Poling for Efficient, High-Fill-Factor Solar Cells," *Joule*, vol. 3, no. 12, pp. 3061–3071, 2019.

[64] Z. Wang, Q. Lin, F. P. Chmiel, N. Sakai, L. M. Herz, and H. J. Snaith, "Efficient ambient-air-stable solar cells with 2D-3D heterostructured butylammonium-caesium-formamidinium lead halide perovskites," *Nature Energy*, vol. 2, no. 9, pp. 1–10, 2017.

[65] T. M. Koh, V. Shanmugam, X. Guo, S. S. Lim, O. Filonik, E. M. Herzig, P. Müller-Buschbaum, V. Swamy, S. T. Chien, S. G. Mhaisalkar, and N. Mathews, "Enhancing moisture tolerance in efficient hybrid 3D/2D perovskite photovoltaics," *Journal of Materials Chemistry A*, vol. 6, no. 5, pp. 2122–2128, 2018.

[66] K. T. Cho, G. Grancini, Y. Lee, E. Oveisi, J. Ryu, O. Almora, M. Tschumi, P. A. Schouwink, G. Seo, S. Heo, J. Park, J. Jang, S. Paek, G. Garcia-Belmonte, and M. K. Nazeeruddin, "Selective growth of layered perovskites for stable and efficient photovoltaics," *Energy and Environmental Science*, vol. 11, no. 4, pp. 952–959, 2018.

[67] B. Conings, J. Drijkoningen, N. Gauquelin, A. Babayigit, J. D'Haen, L. D'Olieslaeger, A. Ethirajan, J. Verbeeck, J. Manca, E. Mosconi, F. De Angelis, and H. G. Boyen, "Intrinsic Thermal Instability of Methylammonium Lead Trihalide Perovskite," *Advanced Energy Materials*, vol. 5, pp. 1–8, 2015.

[68] N. J. Jeon, J. H. Noh, W. S. Yang, Y. C. Kim, S. Ryu, J. Seo, and S. I. Seok, "Compositional engineering of perovskite materials for high-performance solar cells," *Nature*, vol. 517, pp. 476–480, 2015.

[69] W. S. Yang, B.-W. Park, E. H. Jung, N. J. Jeon, Y. C. Kim, D. U. Lee, S. S. Shin, J. Seo, E. K. Kim, J. H. Noh, and S. I. Seok, "Iodide management in formamidinium-lead-halide–based perovskite layers for efficient solar cells," *Science*, vol. 356, no. 6345, pp. 1376–1379, 2017.

[70] H. Choi, J. Jeong, H.-b. Kim, S. Kim, B. Walker, G.-h. Kim, and J. Young, "Cesium-doped methylammonium lead iodide perovskite light absorber for hybrid solar cells," *Nano Energy*, vol. 7, pp. 80–85, 2014.

[71] J.-w. Lee, D.-h. Kim, H.-s. Kim, S.-w. Seo, S. M. Cho, and N.-g. Park, "Formamidinium and Cesium Hybridization for Photo- and Moisture-Stable Perovskite Solar Cell," *Advanced Energy Materials*, vol. 5, no. 1501310, pp. 1–9, 2015.

[72] Z. Li, M. Yang, J.-s. Park, S.-h. Wei, J. J. Berry, and K. Zhu, "Stabilizing Perovskite Structures by Tuning Tolerance Factor: Formation of Formamidinium and Cesium Lead Iodide Solid-State Alloys," *Chemistry of Materials*, no. 28, pp. 284–292, 2016.

[73] C. Yi, J. Luo, S. Meloni, A. Boziki, N. Ashari-Astain, C. Gratzel, S. M. Zakeeruddin, U. Rothlisberger, and M. Gratzel, "Entropic stabilization of mixed A-cation ABX_3 metal halide perovskites for high performance perovskite solar cells," *Energy & Environmental Science*, vol. 9, pp. 656–662, 2016.

[74] K. A. Bush, K. Frohna, R. Prasanna, R. E. Beal, T. Leijtens, S. A. Swifter, and M. D. McGehee, "Compositional Engineering for Efficient Wide Band Gap Perovskites with Improved Stability to Photoinduced Phase Segregation," *ACS Energy Letters*, vol. 3, no. 2, pp. 428–435, 2018.

[75] R. Cheacharoen, C. C. Boyd, G. F. Burkhard, T. Leijtens, J. A. Raiford, K. A. Bush, S. F. Bent, and M. D. McGehee, "Encapsulating perovskite solar cells to withstand damp heat and thermal cycling," *Sustainable Energy and Fuels*, vol. 2, no. 11, pp. 2398–2406, 2018.

[76] J. A. Christians, P. Schulz, J. S. Tinkham, T. H. Schloemer, S. P. Harvey, B. J. Tremolet De Villers, A. Sellinger, J. J. Berry, and J. M. Luther, "Tailored interfaces of unencapsulated perovskite solar cells for >1,000 hour operational stability," *Nature Energy*, vol. 3, no. 1, pp. 68–74, 2018.

[77] E. M. Tennyson, T. A. Doherty, and S. D. Stranks, "Heterogeneity at multiple length scales in halide perovskite semiconductors," *Nature Reviews Materials*, vol. 4, no. 9, pp. 573–587, 2019.

[78] G. W. P. Adhyaksa, S. Brittman, A. Haralds, A. Lof, X. Li, J. D. Keelor, Y. Luo, T. Duevski, R. M. A. Heeren, S. R. Ellis, D. P. Fenning, and E. C. Garnett, "Understanding Detrimental and Beneficial Grain Boundary Effects in Halide Perovskites," *Advanced Materials*, vol. 30, no. 52, pp. 1–9, 2018.

[79] N. Klein-Kedem, D. Cahen, and G. Hodes, "Effects of Light and Electron Beam Irradiation on Halide Perovskites and Their Solar Cells," *Accounts of Chemical Research*, vol. 49, no. 2, pp. 347–354, 2016.

[80] S. A. McHugo and C. Flink, "Thermal stability of copper precipitates in silicon," *Applied Physics Letters*, vol. 77, no. 22, pp. 3598–3600, 2000.

[81] S. A. McHugo, A. C. Thompson, and H. Padmore, "METAL IMPURITY MAPPING IN SEMICONDUCTOR MATERIALS USING X-RAY FLUORESCENCE S.A. McHugo, A.C. Thompson and H. Padmore Lawrence Berkeley National Laboratory, Berkeley, CA, USA," *Mat. Res. Soc. Sympo. Proc*, vol. 510, pp. 589–594, 1998.

[82] M. A. Jensen, J. Hofstetter, A. E. Morishige, G. Coletti, B. Lai, D. P. Fenning, and T. Buonassisi, "Synchrotron-based analysis of chromium distributions in multicrystalline silicon for solar cells," *Applied Physics Letters*, vol. 106, no. 20, pp. 0–5, 2015.

[83] H. S. Laine, V. Vahanissi, A. E. Morishige, J. Hofstetter, A. Haarahiltunen, B. Lai, H. Savin, and D. P. Fenning, "Impact of Iron Precipitation on Phosphorus-Implanted Silicon Solar Cells," *IEEE Journal of Photovoltaics*, vol. 6, no. 5, pp. 1094–1102, 2016.

[84] D. P. Fenning, J. Hofstetter, M. I. Bertoni, G. Coletti, B. Lai, C. Cañizo, and T. Buonassisi, "Precipitated iron : A limit on gettering efficacy in multicrystalline silicon," *Journal of Applied Physics*, vol. 113, no. 4, pp. 044521–1–12, 2013.

[85] S. A. McHugo, A. C. Thompson, I. Périchaud, and S. Martinuzzi, "Direct correlation of transition metal impurities and minority carrier recombination in multicrystalline silicon," *Applied Physics Letters*, vol. 72, no. 26, pp. 3482–3484, 1998.

[86] S. A. McHugo, A. C. Thompson, A. Mohammed, G. Lamble, I. Perichaud, S. Martinuzzi, M. Werner, M. Rinio, W. Koch, H. Hoefs, and C. Haessler, "Nanometer-scale metal precipitates in multicrystalline silicon solar cells," *Journal of Applied Physics*, vol. 89, no. 8, pp. 4282–4288, 2001.

[87] A. A. Istratov, T. Buonassisi, R. J. McDonald, A. R. Smith, R. Schindler, J. Rand, J. P. Kalejs, and E. R. Weber, "Metal Content of Multicrystalline Silicon for Solar Cells and its Impact on Minority Carrier Diffusion Length," *Solid State Phenomena*, vol. 95-96, no. May 2003, pp. 175–180, 2004.

[88] T. Buonassisi, A. a. Istratov, M. Marcus, M. Heuer, M. Pickett, B. Lai, Z. Cai, S. M. Heald, and E. R. Weber, "Local Measurements of Diffusion Length and Chemical Character of Metal Clusters in Multicrystalline Silicon," *Solid State Phenomena*, vol. 108-109, pp. 577–584, 2005.

[89] M. Kodur, R. E. Kumar, Y. Luo, D. N. Cakan, X. Li, M. Stuckelberger, and D. P. Fenning, "X-Ray Microscopy of Halide Perovskites: Techniques, Applications, and Prospects," *Advanced Energy Materials*, vol. 1903170, pp. 1–25, 2020.

[90] R. P. Winarski, M. V. Holt, V. Rose, P. Fuesz, D. Carbaugh, C. Benson, D. Shu, D. Kline, G. Brian Stephenson, I. McNulty, J. Maser, G. B. Stephenson, I. McNulty, and J. Maser, "A hard X-ray nanoprobe beamline for nanoscale microscopy.," *Journal of Synchrotron Radiation*, vol. 19, no. 6, pp. 1056–60, 2012.

[91] F. Pfeiffer, "X-ray ptychography," *Nature Photonics*, vol. 12, no. 1, pp. 9–17, 2018.

[92] W. Chao, J. Kim, S. Rekawa, P. Fischer, and E. H. Anderson, "Demonstration of 12 nm Resolution Fresnel Zone Plate Lens based Soft X-ray Microscopy," *Optics Express*, vol. 17, no. 20, p. 17669, 2009.

[93] A. R. Sakulich and V. C. Li, "Comparison of the detection limits of EDS and EELS in S/TEM," *33rd Int'l Conf on Cement Microscopy, San Francisco, CA USA*, vol. 16, no. Suppl 2, pp. 1–10, 2011.

[94] N. Chatterjee, "Electron Microprobe Analysis," in *Electron Microprobe Analysis*, no. January, pp. 12–20, MIT, Cambridge, 2012.

[95] M. Nekkab, A. Kahoul, B. Deghfel, N. K. Aylikci, and V. Aylikçi, "Calculation of K-shell fluorescence yields for low-Z elements," *AIP Conference Proceedings*, vol. 1653, no. 020077, pp. 1–6, 2015.

[96] P. Willmott, *An Introduction to Synchrotron Radiation: Techniques and Applications*. John Wiley & Sons, Ltd, 2011.

[97] J. C. Fuggle and N. Martensson, "Core-Level Binding Energies in Metals," *Journal of Electron Spectroscopy and Related Phenomena*, vol. 21, no. 3, pp. 275–281, 1980.

[98] A. Thompson, I. Lindau, D. Attwood, Y. Liu, E. Gullikson, P. Piannetta, M. Howells, A. Robinson, K.-J. Kim, J. Scofield, J. Kirz, J. Underwood, J. Kortright, G. Williams, and H. Winick, *X-Ray Data Booklet*. Lawrence Berkeley National Laboratory, 2009 ed., 2001.

[99] S. Vogt, "MAPS: A set of software tools for analysis and visualization of 3D X-ray fluorescence data sets," *Journal of Chemical Information and Modeling*, vol. 104, pp. 635–638, 2003.

[100] Y. Luo, S. Aharon, M. Stuckelberger, E. Magaña, B. Lai, M. I. Bertoni, L. Etgar, and D. P. Fenning, "The Relationship between Chemical Flexibility and Nanoscale Charge Collection in Hybrid Halide Perovskites," *Advanced Functional Materials*, vol. 28, no. 18, pp. 1–22, 2018.

[101] Y. Luo, S. Gamliel, S. Nijem, S. Aharon, M. Holt, B. Stripe, V. Rose, M. I. Bertoni, L. Etgar, and D. P. Fenning, "Spatially Heterogeneous Chlorine Incorporation in Organic-Inorganic Perovskite Solar Cells," *Chemistry of Materials*, vol. 28, pp. 6536–6543, 2016.

[102] B. M. West, M. Stuckelberger, A. Jeffries, S. Gangam, B. Lai, B. Stripe, J. Maser, V. Rose, S. Vogt, and M. I. Bertoni, "X-ray fluorescence at nanoscale resolution for multicomponent layered structures: A solar cell case study," *Journal of Synchrotron Radiation*, vol. 24, no. 1, pp. 288–295, 2017.

[103] V. Thomsen, "Basic fundamental parameters in X-ray fluorescence," *Spectroscopy (Santa Monica)*, vol. 22, no. 5, pp. 46–50, 2007.

[104] T. Shiraiwa and N. Fujino, "Theoretical Calculation of Fluorescent X-Ray Intensities in Fluorescent X-Ray Spectrochemical Analysis.," *Japanese Journal of Applied Physics*, vol. 5, no. 10, pp. 886–899, 1966.

[105] B. L. Henke, E. M. Gullikson, and J. C. Davis, "X-ray interactions: Photoabsorption, scattering, transmission, and reflection at E = 50-30, 000 eV, Z = 1-92," 1993.

[106] O. F. Vyvenko, T. Buonassisi, A. A. Istratov, H. Hieslmair, A. C. Thompson, R. Schindler, and E. R. Weber, "X-ray beam induced current - A synchrotron radiation based technique for the in situ analysis of recombination properties and chemical nature of metal clusters in silicon," *Journal of Applied Physics*, vol. 91, no. 6, pp. 3614–3617, 2002.

[107] V. Orlov, O. Feklisova, and E. Yakimov, "A comparison of EBIC, LBIC and XBIC methods as tools for multicrystalline Si characterization," *Solid State Phenomena*, vol. 205-206, pp. 142–147, 2014.

[108] C. A. Klein, "Bandgap Dependence and Related Features of Radiation Ionization Energies in Semiconductors," *Journal of Applied Physics*, vol. 39, no. 4, p. 2029, 1968.

[109] O. F. Vyvenko, T. Buonassisi, a. a. Istratov, E. R. Weber, M. Kittler, and W. Seifert, "Application of synchrotron-radiation-based x-ray microprobe techniques for the analysis of recombination activity of metals precipitated at Si/SiGe misfit dislocations," *Journal of Physics: Condensed Matter*, vol. 14, pp. 13079–13086, 2002.

[110] A. Ulvestad, S. O. Hruszkewycz, M. V. Holt, M. O. Hill, I. Calvo-Almazán, S. Maddali, X. Huang, H. Yan, E. Nazaretski, Y. S. Chu, L. J. Lauhon, N. Rodkey, M. I. Bertoni, and M. E. Stuckelberger, "Multimodal X-ray imaging of grain-level properties and performance in a polycrystalline solar cell," *Journal of Synchrotron Radiation*, vol. 26, pp. 1316–1321, 2019.

[111] M. Stuckelberger, T. Nietzold, G. N. Hall, B. West, B. Niesen, C. Ballif, V. Rose, D. P. Fenning, and M. I. Bertoni, "Charge Collection in Hybrid Perovskite Solar Cells : Relation to the Nanoscale Elemental Distribution," *IEEE Journal of Photovoltaics*, vol. 7, no. 2, pp. 590–597, 2017.

[112] A. E. Morishige, H. S. Laine, E. E. Looney, M. A. Jensen, S. Vogt, J. B. Li, B. Lai, H. Savin, and T. Buonassisi, "Increased Throughput and Sensitivity of Synchrotron-Based Characterization for Photovoltaic Materials," *IEEE Journal of Photovoltaics*, vol. 7, no. 3, pp. 763–771, 2017.

[113] C. Ossig, T. Nietzold, B. West, M. Bertoni, G. Falkenberg, C. G. Schroer, and M. E. Stuckelberger, "X-ray Beam Induced Current Measurements for Multi-Modal X-ray Microscopy of Solar Cells," *Journal of Visualized Experiments*, pp. 1–20, aug 2019.

[114] N. Li, Y. Luo, Z. Chen, X. Niu, X. Zhang, J. Lu, J. Jiang, H. Liu, X. Guo, B. Lai, G. Brocks, Q. Chen, D. P. Fenning, and H. Zhou, "Microscopic degradation mechanism in MA-free perovskite solar cells under various stressors intrinsic to operation Nengxu," *submitted*, 2020.

[115] M. U. Rothmann, W. Li, Y. Zhu, A. Liu, Z. Ku, U. Bach, J. Etheridge, and Y.-b. Cheng, "Structural and Chemical Changes to CH3NH3PbI3 Induced by Electron and Gallium Ion Beams," *Advanced Materials*, vol. 30, no. 25, pp. 1–7, 2018.

[116] D. Zhang, Y. Zhu, X. Ying, C.-e. Hsiung, R. Sougrat, K. Li, and Y. Han, "Atomic-resolution transmission electron microscopy of electron beam – sensitive crystalline materials," *Science*, vol. 359, no. 6376, pp. 675–679, 2018.

[117] C.-c. Chang, C.-y. Chi, M. Yao, N. Huang, C.-c. Chen, J. Theiss, A. W. Bushmaker, S. Lalumondiere, T.-w. Yeh, M. L. Povinelli, C. Zhou, P. D. Dapkus, and S. B. Cronin, "Electrical and Optical Characterization of Surface Passivation in GaAs Nanowires," *Nano Letters*, vol. 12, no. 9, pp. 4484–4489, 2012.

[118] V. Kveder, M. Kittler, and W. Schröter, "Recombination activity of contaminated dislocations in silicon: A model describing electron-beam-induced current contrast behavior," *Physical Review B*, vol. 63, no. 11, pp. 1–11, 2001.

[119] Z. J. Wang, S. Tsurekawa, K. Ikeda, T. Sekiguchi, and T. Watanabe, "Relationship between electrical activity and grain boundary structural configuration in polycrystalline silicon," *Interface Science*, vol. 7, no. 2, pp. 197–205, 1999.

[120] H. Leamy, "Charge collection scanning electron microscopy," *Journal of Applied Physics*, vol. 53, no. 6, pp. 51–80, 1982.

[121] E. Edri, S. Kirmayer, S. Mukhopadhyay, K. Gartsman, G. Hodes, and D. Cahen, "Elucidating the charge carrier separation and working mechanism of CH3NH3PbI(3-x)Cl(x) perovskite solar cells.," *Nature communications*, vol. 5, no. 3461, pp. 1–8, 2014.

[122] N. Kedem, T. M. Brenner, M. Kulbak, N. Schaefer, S. Levcenko, I. Levine, D. Abou-Ras, G. Hodes, and D. Cahen, "Light-Induced Increase of Electron Diffusion Length in a p-n Junction Type CH3NH3PbBr3 Perovskite Solar Cell," *Journal of Physical Chemistry Letters*, vol. 6, no. 13, pp. 2469–2476, 2015.

[123] N. Kedem, M. Kulbak, T. M. Brenner, G. Hodes, and D. Cahen, "Type-inversion as a working mechanism of high voltage MAPbBr3(Cl)-based halide perovskite solar cells," *Phys. Chem. Chem. Phys.*, vol. 19, no. 8, pp. 5753–5762, 2017.

[124] B.-w. Park, N. Kedem, M. Kulbak, D. Y. Lee, W. S. Yang, N. J. Jeon, J. Seo, G. Kim, K. J. Kim, T. J. Shin, G. Hodes, D. Cahen, and S. I. Seok, "Understanding how excess lead iodide precursor improves halide perovskite solar cell performance," *Nature Communications*, vol. 9, no. 3301, pp. 1–8, 2018.

[125] H. Hieslmair, A. Istratov, R. Sachdeva, and E. Weber, "New synchrotron-radiation based technique to study localized defects in silicon: "EBIC" with X-ray excitation," *Cryst. Silicon Sol. Cell Mater. Process*, vol. 33, no. 46, pp. 162–165, 2000.

[126] M. Kittler and W. Seifert, "On the origin of EBIC defect contrast in silicon. A reflection on injection and temperature dependent investigations," *Physica Status Solidi (a)*, vol. 138, no. 2, pp. 687–693, 1993.

[127] P. Hovington, D. Drouin, and R. Gauvin, "CASINO : A New Monte Carlo Code in C Language for Electron Beam Interaction — Part I : Description of the Program," *Scanning*, vol. 19, no. 1, pp. 1–14, 1997.

[128] D. Drouin, P. Hovington, R. Gauvin, D. Joy, and N. Evans, "CASINO: A New Monte Carlo Code in C Language for Electron Beam Interaction - Part III: Stopping Power at Low Energies," *Scanning*, vol. 19, no. 1, pp. 29–35, 1997.

[129] D. Drouin, A. Couture, D. Joly, X. Tastet, V. Aimez, and R. Gauvin, "CASINO V2 . 42 — A Fast and Easy-to-use Modeling Tool for Scanning Electron Microscopy and Microanalysis Users," *Scanning*, vol. 29, no. 3, pp. 92–101, 2007.

[130] Y. Tian, M. Peter, E. Unger, M. Abdellah, K. Zheng, T. Pullerits, A. Yartsev, V. Sundström, and I. G. Scheblykin, "Mechanistic insights into perovskite photoluminescence enhancement: Light curing with oxygen can boost yield thousandfold," *Physical Chemistry Chemical Physics*, vol. 17, no. 38, pp. 24978–24987, 2015.

[131] H. Tsai, R. Asadpour, J.-c. Blancon, C. C. Stoumpos, O. Durand, J. W. Strzalka, B. Chen, R. Verduzco, P. M. Ajayan, S. Tretiak, J. Even, M. A. Alam, M. G. Kanatzidis, W. Nie, and A. D. Mohite, "Light-induced lattice expansion leads to high-efficiency perovskite solar cells," *Science*, vol. 360, no. 6384, pp. 67–70, 2018.

[132] S. D. Stranks, V. M. Burlakov, T. Leijtens, J. M. Ball, A. Goriely, and H. J. Snaith, "Recombination Kinetics in Organic-Inorganic Perovskites: Excitons, Free Charge, and Subgap States," *Physical Review Applied*, vol. 2, no. 3, pp. 1–8, 2014.

[133] W. A. Quitsch, D. W. Dequilettes, O. Pfingsten, A. Schmitz, S. Ognjanovic, S. Jariwala, S. Koch, M. Winterer, D. S. Ginger, and G. Bacher, "The Role of Excitation Energy in Photobrightening and Photodegradation of Halide Perovskite Thin Films," *Journal of Physical Chemistry Letters*, vol. 9, no. 8, pp. 2062–2069, 2018.

[134] T. J. Jacobsson, J. P. Correa-Baena, E. Halvani Anaraki, B. Philippe, S. D. Stranks, M. E. F. Bouduban, W. Tress, K. Schenk, J. Teuscher, J. E. Moser, H. Rensmo, and A. Hagfeldt, "Unreacted PbI2 as a Double-Edged Sword for Enhancing the Performance of Perovskite Solar Cells," *Journal of the American Chemical Society*, vol. 138, no. 32, pp. 10331–10343, 2016.

[135] K. A. Bush, A. F. Palmstrom, Z. J. Yu, M. Boccard, R. Cheacharoen, J. P. Mailoa, D. P. McMeekin, R. L. Hoye, C. D. Bailie, T. Leijtens, I. M. Peters, M. C. Minichetti, N. Rolston, R. Prasanna, S. Sofia, D. Harwood, W. Ma, F. Moghadam, H. J. Snaith, T. Buonassisi, Z. C. Holman, S. F. Bent, and M. D. McGehee, "23.6%-Efficient Monolithic Perovskite/Silicon Tandem Solar Cells With Improved Stability," *Nature Energy*, vol. 2, no. 4, pp. 1–7, 2017.

[136] F. Zhang, D. Bi, N. Pellet, C. Xiao, Z. Li, J. J. Berry, S. M. Zakeeruddin, K. Zhu, and M. Grätzel, "Suppressing defects through the synergistic effect of a Lewis base and a Lewis acid for highly efficient and stable perovskite solar cells," *Energy and Environmental Science*, vol. 11, no. 12, pp. 3480–3490, 2018.

[137] W. Rehman, D. P. Mcmeekin, J. B. Patel, R. L. Milot, M. B. Johnston, H. J. Snaith, and L. M. Herz, "Photovoltaic mixed-cation lead mixed-halide perovskites: links between crystallinity, photo-stability and electronic properties," *Energy & Environmental Science*, vol. 10, pp. 361–369, 2017.

[138] Y. Luo, "EBIC - CASINO Tool," 2019.

[139] D. S. Lee, J. S. Yun, J. Kim, A. M. Soufiani, S. Chen, Y. Cho, X. Deng, J. Seidel, S. Lim, S. Huang, and A. W. Ho-Baillie, "Passivation of Grain Boundaries by Phenethylammonium in Formamidinium-Methylammonium Lead Halide Perovskite Solar Cells," *ACS Energy Letters*, vol. 3, no. 3, pp. 647–654, 2018.

[140] W. Ke, C. Xiao, C. Wang, B. Saparov, H. S. Duan, D. Zhao, Z. Xiao, P. Schulz, S. P. Harvey, W. Liao, W. Meng, Y. Yu, A. J. Cimaroli, C. S. Jiang, K. Zhu, M. Al-Jassim, G. Fang, D. B. Mitzi, and Y. Yan, "Employing Lead Thiocyanate Additive to Reduce

the Hysteresis and Boost the Fill Factor of Planar Perovskite Solar Cells," *Advanced Materials*, vol. 28, no. 26, pp. 5214–5221, 2016.

[141] Y. Tidhar, E. Edri, H. Weissman, D. Zohar, D. Cahen, B. Rybtchinski, and S. Kirmayer, "Crystallization of Methyl Ammonium Lead Halide Perovskites : Implications for Photovoltaic Applications," *Journal of American Chemical Society*, vol. 136, pp. 13249–13256, 2014.

[142] Y. Zhao and K. Zhu, "CH ₃ NH ₃ Cl-Assisted One-Step Solution Growth of CH ₃ NH ₃ PbI ₃ : Structure, Charge-Carrier Dynamics, and Photovoltaic Properties of Perovskite Solar Cells," *The Journal of Physical Chemistry C*, vol. 118, no. 18, pp. 9412–9418, 2014.

[143] E. L. Unger, A. R. Bowring, C. J. Tassone, V. L. Pool, A. Gold-parker, R. Cheacharoen, K. H. Stone, E. T. Hoke, M. F. Toney, and M. D. Mcgehee, "Chloride in Lead Chloride-Derived Organo-Metal Halides for Perovskite-Absorber Solar Cells," *Chemistry of Materials*, vol. 26, pp. 7158–7165, 2014.

[144] H. Yu, F. Wang, F. Xie, W. Li, J. Chen, and N. Zhao, "The Role of Chlorine in the Formation Process of CH3NH3PbI3-xClx Perovskite," *Advanced Functional Materials*, vol. 24, pp. 7102–7108, 2014.

[145] Q. Chen, H. Zhou, Y. Fang, A. Z. Stieg, T.-B. Song, H.-H. Wang, X. Xu, Y. Liu, S. Lu, J. You, P. Sun, J. McKay, M. S. Goorsky, and Y. Yang, "The optoelectronic role of chlorine in CH3NH3PbI3(Cl)-based perovskite solar cells," *Nature Communications*, vol. 6, pp. 1–9, 2015.

[146] Q. Wang, M. Lyu, M. Zhang, J.-H. Yun, H. Chen, and L. Wang, "Transition from Tetragonal to Cubic Phase of Organohalide Perovskite: The Role of Chlorine in Crystal Formation of CH3NH3PbI3 on TiO2 Substrates," *The Journal of Physical Chemistry Letters*, vol. 6, pp. 4379–4384, 2015.

[147] M. I. Dar, N. Arora, P. Gao, S. Ahmad, M. Gratzel, and M. K. Nazeeruddin, "Investigation regarding the role of chloride in organic-inorganic halide perovskites obtained from chloride containing precursors," *Nano Letters*, vol. 14, no. 12, pp. 6991–6996, 2014.

[148] V. L. Pool, A. Gold-Parker, M. D. McGehee, and M. F. Toney, "Chlorine in PbCl2-Derived Hybrid-Perovskite Solar Absorbers," *Chemistry of Materials*, vol. 27, no. 21, pp. 7240–7243, 2015.

[149] J. Chae, Q. Dong, J. Huang, and A. Centrone, "Chloride Incorporation Process in CH3NH3PbI3-xClx Perovskites via Nanoscale Bandgap Maps," *Nano Letters*, vol. 15, no. 12, pp. 8114–8121, 2015.

[150] S. Colella, E. Mosconi, P. Fedeli, A. Listorti, F. Orlandi, P. Ferro, T. Besagni, A. Rizzo, G. Calestani, G. Gigli, F. D. Angelis, R. Mosca, and F. Gazza, "MAPbI3-xClx Mixed Halide Perovskite for Hybrid Solar Cells: The Role of Chloride as Dopant on the Transport and Structural Properties," *Chemistry of Materials*, vol. 25, no. 22, pp. 4613–4618, 2013.

[151] L. Liu, H. W. Choi, P. T. Lai, and J. Xu, "Passivation of oxide traps in gallium arsenide (semiconductor) metal-oxide-semiconductor capacitor with high-k dielectric by using fluorine incorporation," *Journal of Vacuum Science & Technology B, Nanotechnology and Microelectronics: Materials, Processing, Measurement, and Phenomena*, vol. 33, no. 050601, pp. 1–5, 2015.

[152] T. Sakurai, "Theory of continuously distributed trap states at Si-SiO2 interfaces," *Journal of Applied Physics*, vol. 52, no. 4, pp. 2889–2896, 1981.

[153] D. Rudmann, A. F. da Cunha, M. Kaelin, F. Kurdesau, H. Zogg, A. N. Tiwari, and G. Bilger, "Efficiency enhancement of Cu(In,Ga)Se2 solar cells due to post-deposition Na incorporation," *Applied Physics Letters*, vol. 84, no. 7, pp. 1129–1131, 2004.

[154] A. G. Aberle, "Overview on SiN surface passivation of crystalline silicon solar cells," *Solar Energy Materials and Solar Cells*, vol. 65, no. 1, pp. 239–248, 2001.

[155] D. W. DeQuilettes, S. M. Vorpahl, S. D. Stranks, H. Nagaoka, G. E. Eperon, M. E. Ziffer, H. J. Snaith, and D. S. Ginger, "Impact of microstructure on local carrier lifetime in perovskite solar cells," *Science*, vol. 348, no. 6235, pp. 683–686, 2015.

[156] W. A. Laban and L. Etgar, "Depleted hole conductor-free lead halide iodide heterojunction solar cells," *Energy & Environmental Science*, vol. 6, no. 11, pp. 3249–3253, 2013.

[157] A. Mei, X. Li, L. Liu, Z. Ku, T. Liu, Y. Rong, M. Xu, M. Hu, J. Chen, Y. Yang, M. Grätzel, and H. Han, "A hole-conductor–free, fully printable mesoscopic perovskite solar cell with high stability," *Science*, vol. 345, no. 6194, pp. 295–298, 2014.

[158] S. Aharon, S. Gamliel, B. El Cohen, and L. Etgar, "Depletion region effect of highly efficient hole conductor free CH3NH3PbI3 perovskite solar cells.," *Physical chemistry chemical physics : PCCP*, vol. 16, no. 22, pp. 10512–8, 2014.

[159] B.-E. Cohen, S. Aharon, A. Dymshits, and L. Etgar, "Impact of Anti-Solvent Treatment on Carrier Density in Efficient Hole Conductor Free Perovskite based Solar Cells," *The Journal of Physical Chemistry C*, vol. 120, no. 1, pp. 142–147, 2015.

[160] Q. Chen, H. Zhou, Z. Hong, S. Luo, H.-S. Duan, H.-H. Wang, Y. Liu, G. Li, and Y. Yang, "Planar heterojunction perovskite solar cells via vapor assisted solution process.," *Journal of the American Chemical Society*, no. 136, pp. 622–625, 2013.

[161] B. E. Cohen, S. Gamliel, and L. Etgar, "Parameters influencing the deposition of methylammonium lead halide iodide in hole conductor free perovskite-based solar cells," *APL Materials*, vol. 2, no. 081502, pp. 1–8, 2014.

[162] S. Gamliel, A. Dymshits, S. Aharon, E. Terkieltaub, and L. Etgar, "Micrometer Sized Perovskite Crystals in Planar Hole Conductor Free Solar Cells," *The Journal of Physical Chemistry C*, vol. 119, no. 34, pp. 19722–19728, 2015.

[163] C. Li, Y. Wu, J. Poplawsky, T. J. Pennycook, N. Paudel, W. Yin, S. J. Haigh, M. P. Oxley, A. R. Lupini, M. Al-Jassim, S. J. Pennycook, and Y. Yan, "Grain-boundary-enhanced carrier collection in CdTe solar cells," *Physical Review Letters*, vol. 112, no. 15, pp. 1–5, 2014.

[164] J. S. Yun, A. Ho-Baillie, S. Huang, S. H. Woo, Y. Heo, J. Seidel, F. Huang, Y. B. Cheng, and M. A. Green, "Benefit of grain boundaries in organic-inorganic halide planar perovskite solar cells," *Journal of Physical Chemistry Letters*, vol. 6, no. 5, pp. 875–880, 2015.

[165] Q. Chen, H. Zhou, T. B. Song, S. Luo, Z. Hong, H. S. Duan, L. Dou, Y. Liu, and Y. Yang, "Controllable self-induced passivation of hybrid lead iodide perovskites toward high performance solar cells," *Nano Letters*, vol. 14, no. 7, pp. 4158–4163, 2014.

[166] W. Rehman, R. L. Milot, G. E. Eperon, C. Wehrenfennig, J. L. Boland, H. J. Snaith, M. B. Johnston, and L. M. Herz, "Charge-Carrier Dynamics and Mobilities in Formamidinium Lead Mixed-Halide Perovskites," *Advanced Materials*, vol. 27, no. 48, pp. 7938–7944, 2015.

[167] A. Sadhanala, F. Deschler, T. H. Thomas, S. E. Dutton, K. C. Goedel, F. C. Hanusch, M. L. Lai, U. Steiner, T. Bein, P. Docampo, D. Cahen, and R. H. Friend, "Preparation of Single Phase Films of CH 3 NH 3 Pb(I 1-x Br x) 3 with Sharp Optical Band Edges," *The Journal of Physical Chemistry Letters*, no. 5, pp. 2501–2505, 2014.

[168] D. P. Mcmeekin, G. Sadoughi, W. Rehman, G. E. Eperon, M. Saliba, M. T. Hörantner, A. Haghighirad, N. Sakai, L. Korte, B. Rech, M. B. Johnston, L. M. Herz, H. J. Snaith, M. T. Horantner, A. Haghighirad, N. Sakai, L. Korte, B. Rech, M. B. Johnston, L. M. Herz, and H. J. Snaith, "A mixed-cation lead mixed-halide perovskite absorber for tandem solar cells," *Science*, vol. 351, no. 6269, pp. 151–155, 2016.

[169] W. Tress, N. Marinova, T. Moehl, S. M. Zakeeruddin, M. K. Nazeeruddin, and M. Grätzel, "Understanding the rate-dependent J–V hysteresis, slow time component, and aging in $CH_3NH_3PbI_3$ perovskite solar cells: the role of a compensated electric field," *Energy Environ. Sci.*, vol. 8, no. 3, pp. 995–1004, 2015.

[170] S. Van Reenen, M. Kemerink, and H. J. Snaith, "Modeling Anomalous Hysteresis in Perovskite Solar Cells," *Journal of Physical Chemistry Letters*, vol. 6, no. 19, pp. 3808–3814, 2015.

[171] J.-P. Correa-Baena, A. Abate, M. Saliba, W. Tress, T. Jesper Jacobsson, M. Grätzel, and A. Hagfeldt, "The rapid evolution of highly efficient perovskite solar cells," *Energy Environ. Sci.*, vol. 10, pp. 710–727, 2017.

[172] E. L. Unger, E. T. Hoke, C. D. Bailie, W. H. Nguyen, A. R. Bowring, T. Heumüller, M. G. Christoforo, and M. D. McGehee, "Hysteresis and transient behavior in current–voltage measurements of hybrid-perovskite absorber solar cells," *Energy & Environmental Science*, vol. 7, no. 11, pp. 3690–3698, 2014.

[173] S. J. Yoon, S. Draguta, J. S. Manser, O. Sharia, W. F. Schneider, M. Kuno, and P. V. Kamat, "Tracking Iodide and Bromide Ion Segregation," *ACS Energy Letters*, vol. 1, no. 1, pp. 290–296, 2016.

[174] P. Gratia, G. Grancini, J.-n. Audinot, X. Jeanbourquin, E. Mosconi, I. Zimmermann, D. Dowsett, Y. Lee, M. Gra, and F. D. Angelis, "Intrinsic Halide Segregation at Nanometer Scale Determines the High E ffi ciency of Mixed Cation/Mixed Halide Perovskite Solar Cells," *Journal of American Chemical Society*, vol. 138, pp. 15821–15824, 2016.

[175] J. L. Luria, N. Hoepker, R. Bruce, A. R. Jacobs, C. Groves, and J. A. Marohn, "Spectroscopic imaging of photopotentials and photoinduced potential fluctuations in a bulk heterojunction solar cell film," *ACS Nano*, vol. 6, no. 11, pp. 9392–9401, 2012.

[176] T. Y. Yang, G. Gregori, N. Pellet, M. Grtäzel, and J. Maier, "The Significance of Ion Conduction in a Hybrid Organic-Inorganic Lead-Iodide-Based Perovskite Photosensitizer," *Angewandte Chemie - International Edition*, vol. 54, pp. 7905–7910, 2015.

[177] S. Meloni, T. Moehl, W. Tress, M. Franckevičius, M. Saliba, Y. H. Lee, P. Gao, M. K. Nazeeruddin, S. M. Zakeeruddin, U. Rothlisberger, and M. Graetzel, "Ionic polarization-induced current–voltage hysteresis in CH3NH3PbX3 perovskite solar cells," *Nature Communications*, vol. 7, pp. 1–9, 2016.

[178] A. Walsh, D. O. Scanlon, S. Chen, X. G. Gong, and S. H. Wei, "Self-regulation mechanism for charged point defects in hybrid halide perovskites," *Angewandte Chemie - International Edition*, vol. 54, no. 6, pp. 1791–1794, 2015.

[179] J. Mizusaki, K. Arai, and K. Fueki, "Ionic conduction of the perovskite-type halides," *Solid State Ionics*, vol. 11, no. 3, pp. 203–211, 1983.

[180] Y. Yuan, J. Chae, Y. Shao, Q. Wang, Z. Xiao, A. Centrone, and J. Huang, "Photovoltaic Switching Mechanism in Lateral Structure Hybrid Perovskite Solar Cells," *Advanced Energy Materials*, vol. 5, pp. 1–7, 2015.

[181] D. W. DeQuilettes, W. Zhang, V. M. Burlakov, D. J. Graham, T. Leijtens, A. Osherov, V. Bulović, H. J. Snaith, D. S. Ginger, and S. D. Stranks, "Photo-induced halide redistribution in organic–inorganic perovskite films," *Nature Communications*, vol. 7, no. May, pp. 1–9, 2016.

[182] C. Li, S. Tscheuschner, F. Paulus, P. E. Hopkinson, J. Kießling, A. Köhler, Y. Vaynzof, and S. Huettner, "Iodine Migration and its Effect on Hysteresis in Perovskite Solar Cells," *Advanced Materials*, vol. 28, pp. 2446–2454, 2016.

[183] A. Benninghoven, "Chemical Analysis of Inorganic and Organic Surfaces and Thin Films by Static Time-of-Flight Secondary Ion Mass Spectrometry (TOF-SIMS)," *Angewandte Chemie - International Edition*, no. 33, pp. 1023–1043, 1994.

[184] D. Meggiolaro, S. G. Motti, E. Mosconi, A. J. Barker, J. Ball, C. Andrea Riccardo Perini, F. Deschler, A. Petrozza, and F. De Angelis, "Iodine chemistry determines the defect tolerance of lead-halide perovskites," *Energy and Environmental Science*, vol. 11, no. 3, pp. 702–713, 2018.

[185] S. Mastroianni, F. D. Heinz, J.-H. Im, W. Veurman, M. Padilla, M. C. Schubert, U. Würfel, M. Grätzel, N.-G. Park, and A. Hinsch, "Analysing the effect of crystal size and structure in highly efficient CH ₃ NH ₃ PbI ₃ perovskite solar cells by spatially resolved photo- and electroluminescence imaging," *Nanoscale*, vol. 7, no. 46, pp. 19653–19662, 2015.

[186] A. M. Soufiani, M. J. Y. Tayebjee, S. Meyer, A. Ho-Baillie, J. Sung Yun, R. W. McQueen, L. Spiccia, M. A. Green, and Z. Hameiri, "Electro- and photoluminescence imaging as fast screening technique of the layer uniformity and device degradation in planar perovskite solar cells," *Journal of Applied Physics*, vol. 120, no. 035702, pp. 1–7, 2016.

[187] A. M. Soufiani, Z. Hameiri, S. Meyer, S. Lim, M. J. Y. Tayebjee, J. S. Yun, A. Ho-Baillie, G. J. Conibeer, L. Spiccia, and M. A. Green, "Lessons Learnt from Spatially Resolved Electro- and Photoluminescence Imaging: Interfacial Delamination in CH3NH3PbI3 Planar Perovskite Solar Cells upon Illumination," *Advanced Energy Materials*, vol. 7, no. 1602111, pp. 1–12, 2017.

[188] U. Rau, "Reciprocity relation between photovoltaic quantum efficiency and electroluminescent emission of solar cells," *Physical Review B - Condensed Matter and Materials Physics*, vol. 76, no. 8, pp. 1–8, 2007.

[189] M. A. Green, "Solar Cells Utilizing Small Molecular Weight Organic Semiconductors," *Prog. Photovolt: Res. Appl.*, vol. 20, pp. 472–476, 2012.

[190] P. Khoram, S. Brittman, W. I. Dzik, J. N. H. Reek, and E. C. Garnett, "Growth and Characterization of PDMS-Stamped Halide Perovskite Single Microcrystals," *Journal of Physical Chemistry C*, vol. 120, no. 12, pp. 6475–6481, 2016.

[191] K. Domanski, J. P. Correa-Baena, N. Mine, M. K. Nazeeruddin, A. Abate, M. Saliba, W. Tress, A. Hagfeldt, and M. Gr??tzel, "Not All That Glitters Is Gold: Metal-Migration-Induced Degradation in Perovskite Solar Cells," *ACS Nano*, vol. 10, no. 6, pp. 6306–6314, 2016.

[192] E. J. Juarez-Perez, L. K. Ono, I. Uriarte, E. J. Cocinero, and Y. Qi, "Degradation Mechanism and Relative Stability of Methylammonium Halide Based Perovskites Analyzed on the Basis of Acid-Base Theory," *ACS Applied Materials and Interfaces*, vol. 11, no. 13, pp. 12586–12593, 2019.

[193] K. Ando, A. Yamamoto, and M. Yamaguchi, "Bias-dependent photoluminescence intensities in n-InP Schottky diodes," *Journal of Applied Physics*, vol. 51, no. 12, pp. 6432–6434, 1980.

[194] I. E. Beckers, U. Fiedeler, S. Siebentritt, and M. C. Lux-Steiner, "Voltage dependent electromodulated photoluminescence of chalcopyrite solar cells," *Journal of Physics and Chemistry of Solids*, vol. 64, no. 9-10, pp. 2031–2035, 2003.

[195] N. N. Winogradoff, "Field Control of the Quantum Efficiency of Radiative Recombination in Semiconductors," *Physical Review*, vol. 138, pp. A1562–A1568, may 1965.

[196] M. Stuckelberger, B. West, T. Nietzold, B. Lai, J. M. Maser, V. Rose, and M. I. Bertoni, "Review: Engineering Solar Cells Based on Correlative X-Ray Microscopy," *Journal of Materials Research*, vol. 32, no. 10, pp. 1825–1854, 2017.

[197] H. Cho, S.-H. Jeong, M.-H. Park, Y.-H. Kim, C. Wolf, C.-L. Lee, J. H. Heo, A. Sadhanala, N. Myoung, S. Yoo, S. H. Im, R. H. Friend, and T.-W. Lee, "Overcoming the electroluminescence efficiency limitations of perovskite light-emitting diodes," *Science*, vol. 350, no. 6265, pp. 1222–1225, 2015.

[198] J. Yan, B. Zhang, Y. Chen, A. Zhang, and X. Ke, "Improving the Photoluminescence Properties of Perovskite CH3NH3PbBr3-xClx Films by Modulating Organic Cation and Chlorine Concentrations," *ACS Applied Materials and Interfaces*, vol. 8, no. 20, pp. 12756–12763, 2016.

[199] K. Zheng, M. Abdellah, Q. Zhu, Q. Kong, G. Jennings, C. A. Kurtz, M. E. Messing, Y. Niu, D. J. Gosztola, M. J. Al-marri, X. Zhang, T. Pullerits, and S. E. Canton, "Direct Experimental Evidence for Photoinduced Strong-Coupling Polarons in Organolead Halide Perovskite Nanoparticles," *J. Phys. Chem. Lett*, vol. 7, pp. 4535–4539, 2016.

[200] J. Haruyama, K. Sodeyama, L. Han, and Y. Tateyama, "First-principles study of ion diffusion in perovskite solar cell sensitizers," *Journal of the American Chemical Society*, vol. 137, no. 32, pp. 10048–10051, 2015.

[201] Z. Deng, B. Radhakrishnan, and S. P. Ong, "Rational Composition Optimization of the Lithium-Rich Li ₃ OCl _{1– x} Br _x Anti-Perovskite Superionic Conductors," *Chemistry of Materials*, vol. 27, no. 10, pp. 3749–3755, 2015.

[202] J.-H. Yang, W.-J. Yin, J.-S. Park, and S.-H. Wei, "Fast self-diffusion of ions in CH ₃ NH ₃ PbI ₃ : the interstiticaly mechanism versus vacancy-assisted mechanism," *J. Mater. Chem. A*, vol. 4, no. 34, pp. 13105–13112, 2016.

[203] H. Mashiyama, Y. Kawamura, H. Kasano, T. Asahi, Y. Noda, and H. Kimura, "Disordered Configuration of Methylammonium of CH3NH3PbBr3 Determined by Single Crystal Neutron Diffractometry," *Ferroelectrics*, vol. 348, no. 1, pp. 182–186, 2007.

[204] G. Kresse and J. Furthmüller, "Efficient iterative schemes for ab initio total-energy calculations using a plane-wave basis set," *Physical Review B - Condensed Matter and Materials Physics*, vol. 54, no. 16, pp. 11169–11186, 1996.

[205] P. E. Blöchl, "Projector augmented-wave method," *Physical Review B*, vol. 50, no. 24, pp. 17953–17979, 1994.

[206] J. P. Perdew, K. Burke, and M. Ernzerhof, "Generalized gradient approximation made simple," *Physical Review Letters*, vol. 77, no. 18, pp. 3865–3868, 1996.

[207] S. P. Ong, W. D. Richards, A. Jain, G. Hautier, M. Kocher, S. Cholia, D. Gunter, V. L. Chevrier, K. A. Persson, and G. Ceder, "Python Materials Genomics (pymatgen): A robust, open-source python library for materials analysis," *Computational Materials Science*, vol. 68, pp. 314–319, 2013.

[208] T. Leijtens, E. T. Hoke, G. Grancini, D. J. Slotcavage, G. E. Eperon, J. M. Ball, M. De Bastiani, A. R. Bowring, N. Martino, K. Wojciechowski, M. D. McGehee, H. J. Snaith, and A. Petrozza, "Mapping electric field-induced switchable poling and structural degradation in hybrid lead halide perovskite thin films," *Advanced Energy Materials*, vol. 5, pp. 1–11, 2015.

[209] T. A. Berhe, W.-N. Su, C.-H. Chen, C.-J. Pan, J.-H. Cheng, H.-M. Chen, M.-C. Tsai, L.-Y. Chen, A. A. Dubale, and B.-J. Hwang, "Organometal halide perovskite solar cells: degradation and stability," *Energy Environ. Sci.*, vol. 9, p. Advance Article, 2016.

[210] C. C. Boyd, R. Cheacharoen, T. Leijtens, and M. D. McGehee, "Understanding Degradation Mechanisms and Improving Stability of Perovskite Photovoltaics," *Chemical Reviews*, vol. 119, no. 5, pp. 3418–3451, 2019.

[211] R. Cheacharoen, N. Rolston, D. Harwood, K. A. Bush, R. H. Dauskardt, and M. D. McGehee, "Design and understanding of encapsulated perovskite solar cells to withstand temperature cycling," *Energy and Environmental Science*, vol. 11, no. 1, pp. 144–150, 2018.

[212] M. I. Saidaminov, J. Kim, A. Jain, R. Quintero-Bermudez, H. Tan, G. Long, F. Tan, A. Johnston, Y. Zhao, O. Voznyy, and E. H. Sargent, "Suppression of atomic vacancies via incorporation of isovalent small ions to increase the stability of halide perovskite solar cells in ambient air," *Nature Energy*, vol. 3, no. 8, pp. 648–654, 2018.

[213] N. Aristidou, I. Sanchez-Molina, T. Chotchuangchutchaval, M. Brown, L. Martinez, T. Rath, and S. A. Haque, "The Role of Oxygen in the Degradation of Methylammonium Lead Trihalide Perovskite Photoactive Layers," *Angewandte Chemie - International Edition*, vol. 54, no. 28, pp. 8208–8212, 2015.

[214] M. A. Leguy, Y. Hu, M. Campoy-quiles, M. I. Alonso, O. J. Weber, P. Azarhoosh, M. V. Schilfgaarde, M. T. Weller, T. Bein, J. Nelson, P. Docampo, and P. R. F. Barnes, "Reversible Hydration of CH3NH3PbI3 in Films, Single Crystals, and Solar Cells," *Chemistry of Materials*, vol. 27, pp. 3397–3407, 2015.

[215] Silver-Hamill Turren-Cruz, A. Hagfeldt, and M. Saliba, "Methylammonium-free, high-performance, and stable perovskite solar cells on a planar architecture," *Science*, vol. 3, no. October, pp. 449–453, 2018.

[216] F. El-Mellouhi, A. Marzouk, E. T. Bentria, S. N. Rashkeev, S. Kais, and F. H. Alharbi, "Hydrogen Bonding and Stability of Hybrid Organic–Inorganic Perovskites," *ChemSusChem*, vol. 9, no. 18, pp. 2648–2655, 2016.

[217] C. Motta, F. El-Mellouhi, S. Kais, N. Tabet, F. Alharbi, and S. Sanvito, "Revealing the role of organic cations in hybrid halide perovskite CH3 NH3PbI3," *Nature Communications*, vol. 6, no. May 2014, pp. 1–7, 2015.

[218] D. A. Egger and L. Kronik, "Role of dispersive interactions in determining structural properties of organic-inorganic halide perovskites: Insights from first-principles calculations," *Journal of Physical Chemistry Letters*, vol. 5, no. 15, pp. 2728–2733, 2014.

[219] J. M. Azpiroz, E. Mosconi, J. Bisquert, and F. De Angelis, "Defect migration in methylammonium lead iodide and its role in perovskite solar cell operation," *Energy Environ. Sci.*, vol. 8, no. 7, pp. 2118–2127, 2015.

[220] F. Brivio, C. Caetano, and A. Walsh, "Thermodynamic Origin of Photoinstability in the CH3NH3Pb(I1-xBrx)3 Hybrid Halide Perovskite Alloy," *Journal of Physical Chemistry Letters*, vol. 7, no. 6, pp. 1083–1087, 2016.

[221] D. J. Slotcavage, H. I. Karunadasa, and M. D. McGehee, "Light-Induced Phase Segregation in Halide-Perovskite Absorbers," *ACS Energy Letters*, vol. 1, no. 6, pp. 1199–1205, 2016.

[222] D. Bi, X. Li, J. V. Milić, D. J. Kubicki, N. Pellet, J. Luo, T. LaGrange, P. Mettraux, L. Emsley, S. M. Zakeeruddin, and M. Grätzel, "Multifunctional molecular modulators for perovskite solar cells with over 20% efficiency and high operational stability," *Nature Communications*, vol. 9, no. 1, pp. 1–10, 2018.

[223] M. H. Futscher, J. M. Lee, L. McGovern, L. A. Muscarella, T. Wang, M. I. Haider, A. Fakharuddin, L. Schmidt-Mende, and B. Ehrler, "Quantification of ion migration in CH3NH3PbI3 perovskite solar cells by transient capacitance measurements," *Materials Horizons*, vol. 6, no. 7, pp. 1497–1503, 2019.

[224] G. Y. Kim, A. Senocrate, T. Y. Yang, G. Gregori, M. Grätzel, and J. Maier, "Large tunable photoeffect on ion conduction in halide perovskites and implications for photodecomposition," *Nature Materials*, vol. 17, no. 5, pp. 445–449, 2018.

[225] R. W. Balluffi, S. M. Allen, and W. C. Carter, *Kinetics of Materials*. John Wiley & Sons, 2005.

[226] D. Bi, W. Tress, M. I. Dar, P. Gao, J. Luo, C. Renevier, K. Schenk, A. Abate, G. Fabrizio, J.-p. C. Baena, J.-d. Decoppet, S. M. Zakeeruddin, M. K. Nazeeruddin, M. Gratzel, and A. Hagfeldt, "Efficient luminescent solar cells based on tailored mixed-cation perovskites Efficient luminescent solar cells based on tailored mixed-cation perovskites," *Sci. Adv.*, vol. 2, no. 1, pp. 1–7, 2016.

[227] M. Kim, G. H. Kim, T. K. Lee, I. W. Choi, H. W. Choi, Y. Jo, Y. J. Yoon, J. W. Kim, J. Lee, D. Huh, H. Lee, S. K. Kwak, J. Y. Kim, and D. S. Kim, "Methylammonium Chloride Induces Intermediate Phase Stabilization for Efficient Perovskite Solar Cells," *Joule*, vol. 3, no. 9, pp. 2179–2192, 2019.

[228] Q. Jiang, Y. Zhao, X. Zhang, X. Yang, Y. Chen, Z. Chu, Q. Ye, X. Li, Z. Yin, and J. You, "Surface passivation of perovskite film for efficient solar cells," *Nature Photonics*, vol. 13, no. 7, pp. 460–466, 2019.

[229] N. Pellet, P. Gao, G. Gregori, T. Y. Yang, M. K. Nazeeruddin, J. Maier, and M. Grätzel, "Mixed-organic-cation perovskite photovoltaics for enhanced solar-light harvesting," *Angewandte Chemie - International Edition*, vol. 53, no. 12, pp. 3151–3157, 2014.

[230] M. Zhang, J. S. Yun, Q. Ma, J. Zheng, C. F. J. Lau, X. Deng, J. Kim, D. Kim, J. Seidel, M. A. Green, S. Huang, and A. W. Ho-Baillie, "High-Efficiency Rubidium-Incorporated Perovskite Solar Cells by Gas Quenching," *ACS Energy Letters*, vol. 2, no. 2, pp. 438–444, 2017.

[231] S. H. Turren-Cruz, M. Saliba, M. T. Mayer, H. Juarez-Santiesteban, X. Mathew, L. Nienhaus, W. Tress, M. P. Erodici, M.-j. Sher, M. G. Bawendi, M. Gratzel, A. Abate, A. Hagfeldt, and J.-P. Correa-Baena, "Enhanced charge carrier mobility and lifetime suppress hysteresis and improve efficiency in planar perovskite solar cells," *Energy & Environmental Science*, vol. 11, pp. 78–86, 2018.

[232] T. Bu, X. Liu, Y. Zhou, J. Yi, X. Huang, L. Luo, J. Xiao, Z. Ku, Y. Peng, F. Huang, Y. B. Cheng, and J. Zhong, "A novel quadruple-cation absorber for universal hysteresis elimination for high efficiency and stable perovskite solar cells," *Energy and Environmental Science*, vol. 10, no. 12, pp. 2509–2515, 2017.

[233] W. Tress, "Perovskite Solar Cells on the Way to Their Radiative Efficiency Limit – Insights Into a Success Story of High Open-Circuit Voltage and Low Recombination," *Advanced Energy Materials*, vol. 7, no. 14, 2017.

[234] C. Roldán-Carmona, P. Gratia, I. Zimmermann, G. Grancini, P. Gao, M. Graetzel, and M. K. Nazeeruddin, "High efficiency methylammonium lead triiodide perovskite solar cells: The relevance of non-stoichiometric precursors," *Energy and Environmental Science*, vol. 8, no. 12, pp. 3550–3556, 2015.

[235] M. Abdi-Jalebi, Z. Andaji-Garmaroudi, S. Cacovich, C. Stavrakas, B. Philippe, J. M. Richter, M. Alsari, E. P. Booker, E. M. Hutter, A. J. Pearson, S. Lilliu, T. J. Savenije, H. Rensmo, G. Divitini, C. Ducati, R. H. Friend, and S. D. Stranks, "Maximizing and stabilizing luminescence from halide perovskites with potassium passivation," *Nature Publishing Group*, vol. 555, no. 7697, pp. 497–501, 2018.

[236] H. Demers, N. Poirier-Demers, A. R. Couture, D. Joly, M. Guilmain, N. De Jonge, and D. Drouin, "Three-dimensional electron microscopy simulation with the CASINO Monte Carlo software," *Scanning*, vol. 33, no. 3, pp. 135–146, 2011.

[237] S. Wang, M. Sina, P. Parikh, T. Uekert, B. Shahbazian, A. Devaraj, and Y. S. Meng, "Role of 4-tert-Butylpyridine as a Hole Transport Layer Morphological Controller in Perovskite Solar Cells," *Nano Letters*, vol. 16, no. 9, pp. 5594–5600, 2016.